

Development of a Scanning Nearfield Optical Microscope for Low-Temperature Investigations of Semiconductor Nanostructures

vorgelegt von
Dipl. Phys. Kai Friedrich Hodeck
aus Berlin

Von der Fakultät II Mathematik und Naturwissenschaften
der Technischen Universität Berlin
zur Erlangung des akademischen Grades

Doktor der Naturwissenschaften
- Dr. rer. nat. -
genehmigte Dissertation

Promotionsausschuß:
Vorsitzender: Prof. Dr. M. Lehmann
Gutachter: Prof. Dr. M. Dähne
Gutachter: PD Dr. A. Hoffmann

Tag der wissenschaftlichen Aussprache: 19. Februar 2009

Berlin 2009
D 83

Eidesstattliche Versicherung

Hiermit versichere ich an Eides statt, dass ich meine Dissertation mit dem Titel:

”Development of a Scanning Nearfield Optical Microscope for Low-Temperature Investigations of Semiconductor Nanostructures”

selbständig verfasst habe. Alle benutzten Hilfsmittel und Quellen sind in der Arbeit aufgeführt.

Berlin, April 15, 2009

Abstractum

Im Rahmen der vorliegenden Arbeit wurde mittels optischer Rasternahfeldmikroskopie (SNOM) die elektronische Struktur von MOCVD-gewachsenen InGaAs/GaAs- und InAs/GaAs-Quantenpunkten untersucht, die sich durch eine besonders niedrige Grundzustands-Übergangsenergie auszeichnen. Im Zentrum der vorgestellten Untersuchungen steht die Frage, welchen Einfluss die Wechselwirkung von im Quantenpunkt befindlichen Ladungen auf die Energiezustände von Biexzitonen und Mehrfachexzitonen hat. Dazu wurden Photolumineszenz-Spektren einzelner Quantenpunkte unter variierender Anregungsintensität bei verschiedenen Temperaturen zwischen 5 K und 300 K untersucht.

Die Untersuchung einzelner Quantenpunkte wurde möglich durch die Konstruktion eines neuen Rasternahfeldmikroskops speziell für den Betrieb bei tiefen Temperaturen. Durch entscheidende Verbesserungen der Positioniertechnologie und der Scherkraft-Abstandsregelung von Probe und Nahfeld-Sonde wurde erreicht, dass mit dem neuen Tieftemperatur-SNOM erstmalig stabiles Rastern der Quantenpunkt-Proben bei 5 K mit einer lateralen optischen Auflösung von 200 nm demonstriert werden konnte. Auf diese Weise wurde bei der Photolumineszenz-Spektroskopie einzelner Quantenpunkte die thermische Linienverbreiterung des detektierten Lichts bis auf Werte unterhalb 1 meV reduziert, was die Identifikation von Biexzitonen- und Mehrfachexzitonenübergängen erlaubte.

Anhand der durchgeführten Messungen wurde für die InGaAs/GaAs-Quantenpunkte insbesondere ein Biexzitonzustand mit einer variierenden Bindungsenergie von 2 – 7 meV festgestellt. Zudem wurde das Auftreten eines emissionsstarken positiv geladenen Trionzustands mit einer Bindungsenergie von -11 meV beobachtet. Dieser kann auf die Probendotierung zurückgeführt werden. Entsprechend kann auch für den positiv geladenen Biexzitonzustand eine Bindungsenergie von 11 meV angegeben werden. Für die untersuchten InAs/GaAs-Quantenpunkte wurde ein Biexzitonzustand mit einer Bindungsenergie von 3 – 4 meV gefunden. An einigen der untersuchten InAs/GaAs-Quantenpunkte wurde ebenfalls die Ausbildung positiv geladener Zustände festgestellt, insbesondere des Trionzustands mit einer Bindungsenergie von -3 meV, und des positiv geladenen Biexzitons mit einer Bindungsenergie von 1 meV.

Diese Werte konnten im Rahmen der vorliegenden Arbeit erstmalig für InGaAs- und InAs-Quantenpunkte mit einer Grundzustands-Übergangsenergie von 1.0 – 1.1 eV experimentell bestimmt werden. Die in dieser Arbeit gewonnenen Erkenntnisse lassen auf eine nichtlineare Fortentwicklung des bisher für Quantenpunkte mit erheblich höheren Grundzustandsenergien als linear angenommenen Verhaltens der elektronischen Zustände schliessen. Insbesondere wird eine sukzessive Reduktion der Bindungsenergien exzitonischer Komplexe, speziell des Biexzitons erwartet. Die damit korrelierte Verringerung der spektralen Feinstrukturaufspaltung ermöglicht prinzipiell eine technologische Anwendung als Einzelphotonenquelle.

Abstract

In the present work the electronic structure of MOCVD-grown InGaAs/GaAs and InAs/GaAs quantum dots which are characterized by a particularly low ground state transition energy, was investigated using Scanning Nearfield Optical Microscopy (SNOM). The pivotal question of the presented investigations is, which influence the interaction of the confined carriers has on the energy states of the biexcitons and the multiexcitons in a quantum dot. Therefore, photoluminescence spectra of single quantum dots were investigated under varying excitation intensity at different temperatures between 5 K and 300 K.

The construction of a novel scanning nearfield microscope especially for low temperatures allowed the investigation of single quantum dots. Due to significant improvements of the positioning technology and the shear-force distance control between the sample and the nearfield probe a stable scanning of the quantum dot samples at 5 K could be demonstrated, showing a lateral optical resolution of 200 nm. This way, in the photoluminescence spectroscopy of single quantum dots the thermal linewidth broadening of the detected light was reduced down to a value of less than 1 meV, which allowed the identification of the transitions of biexcitons and multiexcitons.

On the basis of the performed measurements, for the InGaAs/GaAs quantum dots a biexciton state was identified, with variable binding energies of 2 – 7 meV. Furthermore, a positively charged trion state with a binding energy of 11 meV was observed, showing high emission intensity, which can be assigned to the sample doping. Accordingly, for the positively charged biexciton state a binding energy of 11 meV can be announced. For the investigated InAs/GaAs quantum dots a biexciton state with binding energies of 3 – 4 meV was found. Some of the investigated InAs/GaAs quantum dots showed the formation of positively charged states, in particular of a trion state with a binding energy of 3 meV, and of the positively charged biexciton with a binding energy of 1 meV.

These values could for the first time be experimentally determined within this work for InGaAs and InAs quantum dots with a ground state transition energy of 1.0 – 1.1 eV. The findings obtained in this work suggest a non-linear extrapolation of the behavior of the electronic states, which has been formerly supposed to be linear for quantum dots with significantly higher ground state energies. In particular, a successive reduction of the binding energies of exciton complexes, specifically of the biexciton, can be expected. The related reduction of the spectral fine structure splitting in principle allows a technological application as a single photon source.

Parts of this work have been published in

- *Multiline photoluminescence of single InGaAs quantum dots*, K. Hodeck, I. Manke, M. Geller, R. Heitz, F. Heinrichsdorff, A. Krost, D. Bimberg, H. Eisele, and M. Dähne, *phys. stat. sol (c)* **0**, 1209 (2003).

Il faut s'imaginer Sisyphe heureux
Albert Camus,
Le Mythe de Sisyphe, 1942

Contents

1	Introduction	1
1.1	Semiconductor quantum dots and scanning nearfield optical microscopy	1
1.2	Structure of this work	3
2	Scanning Nearfield Optical Microscopy	5
2.1	Overcoming classical resolution limitations	5
2.2	Theory of the optical nearfield	6
2.2.1	Probing the evanescent field	8
2.2.2	SNOM configurations	11
2.2.3	Noble-metal tip nearfield antennas	12
2.3	Distance control	15
2.3.1	The shear-force feedback	15
2.3.2	The tuning fork oscillator model	16
2.3.3	Alternative techniques for distance control	20
3	The low-temperature SNOM	23
3.1	Assessment of the system	23
3.2	Low-temperature implementation concept	25
3.2.1	The inertial drive	25
3.2.2	Approaches to a technical solution	26
3.2.3	Innovation of the distance control	32
3.3	Nearfield probes	34
3.4	The photoluminescence spectroscopy setup	37
3.5	Apertureless nearfield microscopy	40
3.6	Characterization of the low-temperature SNOM	49
3.6.1	Calibration of the scanner	49
3.6.2	Obtained topographical resolution	49
3.6.3	Determination of mechanical stability	51
3.6.4	Locating of single quantum dots	52
3.6.5	Obtained lateral optical resolution	54
3.6.6	Low-temperature scanning of quantum dot samples	55

4	Investigations of III-V quantum dots	59
4.1	Semiconductor nanostructures	59
4.1.1	Characteristics of quantum-confined semiconductor structures	59
4.1.2	Self-organized formation of In(Ga)As/GaAs semiconductor quantum dots	60
4.1.3	Atomic structure	61
4.1.4	Electronic properties	62
4.1.5	Luminescence characteristics	65
4.2	Characterization of the samples	71
4.2.1	InGaAs/GaAs quantum dots	71
4.2.2	InAs/GaAs quantum dots	73
4.3	Spectroscopy of individual quantum dots	78
4.3.1	InGaAs/GaAs quantum dots	78
4.3.2	InAs/GaAs quantum dots	87
5	Conclusion	99
	Bibliography	102

Chapter 1

Introduction

1.1 Semiconductor quantum dots and scanning nearfield optical microscopy

In recent years, nanostructures have attracted considerable scientific interest as a coherent field of research on materials which are characterized by a structuring on the scale of a few nanometers. This new classification of matter includes substances as diverse as low-dimensional semiconductor heterostructures [1, 2] and noble metal clusters [3], quantum cavity structures [4, 5] and photonic crystals [6, 7], carbon nanotubes [8, 9], organic molecular aggregates [10] as well as biological systems [11, 12]. These materials have in common that, due to their nanometer-scaled morphology, quantum effects come to the fore which are not observed in macroscopic matter. Owing to these quantum effects the physical properties of nanostructured materials are determined essentially by their particular morphology and local material composition, hence differing qualitatively from those of the chemically identical bulk material.

In particular the so-called low-dimensional semiconductor heterostructures, such as *quantum wells*, *quantum wires* and *quantum dots*, have been subject of intensive investigation over the last decade because of their exceptional opto-electronic properties, making them promising for a large number of innovative technological applications [13–16]. They are called low-dimensional structures because of their peculiar spatial composition, which leads to a restriction of the carrier mobility in one or more dimensions of space, resulting in an energy quantisation [17]. They are further characterized in terms of degrees of freedom of carrier motion as two-dimensional *quantum wells*, one-dimensional *quantum wires*, or zero-dimensional *quantum dots*, respectively.

Technologically, semiconductor nanostructures are fabricated either by inducing self-organized formation during semiconductor heteroepitaxy or by controlled selective-epitaxy processing [18–20]. This work is focused on the investigation of semiconductor quantum dots, particularly on InAs and InGaAs quantum dots

which are embedded in a GaAs matrix. These quantum dot systems have already proven to be suitable for applications such as highly efficient light-emitting devices (LEDs) and infrared lasers [21, 22], as well as promising for innovative memory devices [23] and tunable single-photon sources for quantum information technology [24]. Furthermore, they serve as model systems to explore the basic physics of dimension-reduced structures. One particularly important issue in this regard, which is not understood in detail yet, is the formation of confined few-particle states within a semiconductor quantum dot.

The aim of this work was the detailed investigation of the opto-electronic properties of single self-organized In(Ga)As/GaAs quantum dots which are characterized by a ground-state transition energy of 1.0 – 1.1 eV. This comes quite close to the technologically important value of 0.954 eV which fits the transmission characteristics of standard optical fibers. A particular focus was put on the investigation of the binding energies of few-carrier states in the low-population regime, especially of the biexciton state, which represents a crucial factor for a possible application of quantum dots as controllable single-photon sources [25]. A key method to investigate this is the optical spectroscopy of individual quantum dots, complemented with further information on the structural characteristics of the respective quantum dots. Systematic investigations have been performed already on the electronic properties of InAs/GaAs and InGaAs/GaAs quantum dots with ground-state energies between 1.20 eV and 1.35 eV, providing a solid insight into these structures [26]. By contrast, an exhaustive investigation of the properties of correspondent quantum dots with lower ground state energies is lacking up to now. This work is intended to provide the onset to a detailed investigation of this system, using excitation-dependent spectroscopy of single quantum dots. For this purpose, in the scope of this work a novel scanning nearfield optical microscope (SNOM) had to be developed for the optical spectroscopy of semiconductor quantum dots at low temperatures. In order to investigate single quantum dots, which are separated typically by distances of some 10 – 100 nm within a sample, an extremely high spatial resolution is required, as it generally cannot be achieved by using classical optical microscopy. SNOM offers a powerful solution for this problem: by pointwise scanning of the sample surface at an extremely close distance using an aperture with a sub-wavelength diameter, this technique allows a spatial resolution below the limit of Abbe [27], and thus an investigation of the individual luminescence signals of single quantum dots [28, 29]. Other techniques which can serve for this purpose are cathodoluminescence (CL), micro-photoluminescence (μ -PL), confocal microscopy (CM) or the scanning tunneling luminescence (STL), which are all suitable to detect light emitted from a sample with a lateral resolution of a few 100 nm or below, depending on the particular experimental conditions. Among these various techniques the SNOM stands out providing a combination of an extremely high spatial resolution, sufficient signal intensity and spot control, complemented by the capacity

to obtain high-resolution topographical information from the sample surface in parallel. At low temperatures of 4 – 80 K the thermal linewidth broadening of the photoluminescence is reduced strongly, which allows a spectroscopic resolution of the line shift signature of few-carrier interactions within semiconductor quantum dots.

1.2 Structure of this work

This work is structured in 5 chapters: first, a short introduction is given, including a general motivation and an abstract on the physical questions driving the presented investigations. The second chapter addresses the theory of the scanning nearfield optical microscopy, including the fundamentals of the optical nearfield in general, as well as the essentials of a microscopic imaging that is based on the particular properties of the evanescent field. This regards especially the probing of the optical nearfield of a sample, and the transformation of the evanescent field into propagating waves which can be detected by an appropriate device. Central to this problem from a technological point of view is the fabrication of suitable nanometer-sized probes, as well as a precise and reliable distance control, as it is realized commonly with the shear-force feedback technology. Therefore, a special emphasis is put on the discussion of these issues. The third chapter provides a detailed description of the experimental setup that was developed in the course of this work. This survey is guided along an analysis of the experimental task and the required instrumentation, the technical setting, and the solutions that were found for the specific problems.

Therein is given a presentation of the core microscopy setup which is designed to match the specific requirements and constraints. A strong emphasis is put on the problems that come along with the operation of a scanning nearfield optical microscope under low-temperature conditions. These are primarily, the implementation of a reliable distance control, the positioning of the probe and the sample within the cryostate, and the decoupling of the setup from the impact of external influences, such as heat and mechanical vibrations. In particular is a profound investigation of the critical parameters for the operation of the SNOM probes presented. The latter determine the functioning of a shear-force control based on quartz tuning forks at low temperatures. Further, the fabrication of the probes, i.e. etched and metal-coated optical fiber tips is reported. Part of the third chapter is devoted to the discussion of the so-called apertureless SNOM technique, which was additionally explored within the scope of this work. This special configuration of SNOM makes use of a metal tip as a probe for the optical nearfield, thus allowing in principle for a substantial enhancement of spatial resolution in comparison to the conventional fiber tips. An important part of the third chapter is the calibration of the new setup by means of demonstration

measurements, which provides reference for the operation of the low-temperature SNOM.

The fourth chapter is dedicated to the presentation of the results obtained by the spectroscopic investigations of individual quantum dots with the new setup. The chapter starts giving a theoretical introduction to the basic properties of semiconductor quantum dots, with a special emphasis on their electronic and optical characteristics which are related to the experimental investigations in this work. In the following a detailed characterization of the investigated samples is presented. The main focus of the chapter is put on the presentation of the photoluminescence data from single quantum dots that were obtained at low temperatures. On the basis of these data, a comprehensive review of the related literature, and theoretical considerations and analysis of the emission signals is performed, focusing on the identification of the transitions from the biexciton and the charged exciton state, and a determination of their binding energies. The data are analyzed further in terms of information on the influence of, in particular doping-induced, external fields on the carrier states within the quantum dots. In the last chapter the obtained results are presented in summary in the context of the current state of knowledge.

Chapter 2

Scanning Nearfield Optical Microscopy

2.1 Overcoming classical resolution limitations

A detailed investigation of individual semiconductor quantum dots requires an experimental technique that allows the analysis of microscopically structured matter with a spatial resolution in the range of nanometers. Because classical microscopy is based on the diffraction of light by material structures and a subsequent interference of component waves, the maximum resolution that can be achieved is given by the limit of Abbe:

$$d_{min} \approx \frac{\lambda}{\sqrt{2}N_A} \quad , \quad (2.1)$$

with λ being the wavelength of the light and N_A the numerical aperture of the optics used for imaging [30]. This expression follows from a mathematical treatment of the problem in terms of the diffraction of waves, which yields that, after the interaction with a material structure of dimensions of less than roughly half of the wavelength, there are no diffracted components propagating which could be collected for imaging. Scanning nearfield optical microscopy (SNOM) is an experimental approach to overcoming this limitation by taking advantage of the peculiar properties of the so-called optical nearfield: Even a sub-wavelength dielectric structure will necessarily modulate an incident electromagnetic field due to the boundary conditions at its surface [31]. Accurate treatment shows that the resulting modulation is located strictly within a distance of sub-wavelength dimensions from the structure, which led to the term *nearfield* [32]. Based on an idea coined by Synge in 1928 [33], in SNOM the sample surface is scanned at a very close distance with an appropriate probe in order to pick up the light emanating from the sample in the nearfield region, and the optical information is obtained pointwise and further processed electronically [27, 34]. The principle is adapted from the scanning tunneling microscope (STM) that was developed by

Binnig and Rohrer in 1981 [35, 36]. However, unlike the latter, in a SNOM the probe is an optical element, which can be a nanometer-size dielectric acting as a tiny aperture of sub-wavelength diameter for the electromagnetic field, or another, equally small light source. Most commonly the SNOM probe is an optical fiber tip of some 10 – 100 nm apex diameter [37, 38]. The optical resolution that can be achieved this way is limited primarily by the dimensions of the aperture. In practice it is ranging from about 200 nm down to about 30 nm in extreme cases [39, 40], which gives an improvement of up to 10 times over that which classical microscopy can provide for light in the visible spectrum [39].

2.2 Theory of the optical nearfield

Central to classical optical imaging is the diffraction of a model lightwave in interaction with a material object, which leads to a decomposition of the electromagnetic wave into a series of waves of gradient wavelengths, which are strayed into different directions in space. Each of these components carries part of the full information on the material structure, which is reconstructed in optical imaging by collection and superposition.

To understand this fundamental principle of classical optical imaging, a monochromatic plane wave can be imaged incident onto a diffractive structure that is considered as two-dimensional in the xy -plane. The two-dimensionally structured sample can be thought of abstractly as a composition of gratings, each with a fixed spatial period [31]. Every of the grating structures will modulate the incident wave by diffraction, depending on the respective spatial period d and the angle of incidence Θ_i , in accordance with the Fresnel-condition [41, 42]. The wave is diffracted into different angles Θ_s whenever the respective component of the wave vector \underline{k} with $|\underline{k}| = 2\pi/\lambda$ projected onto the surface is an integer multiple n of the grating wave vector \underline{g} , which is given by $|\underline{g}| = (2\pi/d)$. Given that, for simplicity $\Theta_i = 0^\circ$, as a result the light that is strayed by the diffractive structure receives an angle-dependent intensity profile corresponding to

$$n \lambda = d \sin(\Theta_s) \quad , \quad (2.2)$$

which can be recorded by a detector that is placed at a far distance¹, as shown schematically in Fig. 2.1 [43]. Equation (2.2) conveys that the information on the real-space structure of the object is dispersed into the diffraction image, carried by a series of angular diffraction components, which can be expressed mathematically by a Fourier-transformation from the real space into the k -space of components with wave-vector numbers k_s . The electric field E in a plane $z \parallel xy$ at a distance z_0 can be written as

$$E(x, y, z_0) = \int e(k_x, k_y) \exp(ik_x x + ik_y y + i\gamma z_0) dk_x dk_y \quad (2.3)$$

¹This configuration corresponds to the so-called *far-field* regime

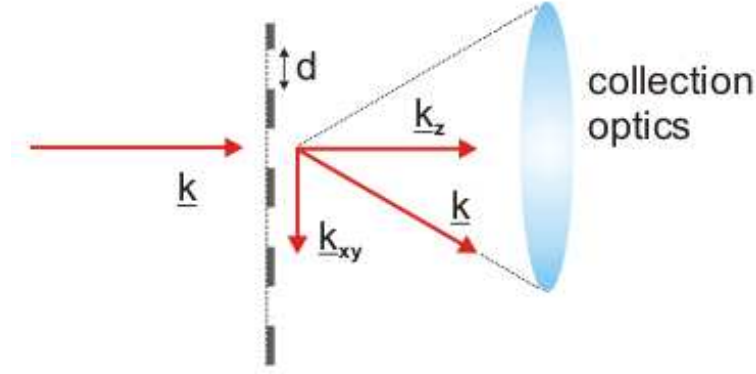


FIGURE 2.1: The diffraction of light at a two-dimensional sample structure leads to a decomposition of the wave vector.

with a maximum value for the wave vector

$$k \equiv |(k_x, k_y, \gamma)| = n \, 2\pi/\lambda \quad , \quad (2.4)$$

which yields

$$\gamma = \sqrt{\left[\frac{n2\pi}{\lambda}\right]^2 - (k_x^2 + k_y^2)} \quad . \quad (2.5)$$

For low spatial frequencies, i.e. for long-period lateral variation of the field in the plane $|(k_x, k_y)|$, the coefficient γ is a real number, and the electric field is a propagating wave along the axis perpendicular to the object plane [43]. The reconstruction of the information on the sample structure depends on the detection of the diffracted wave components and the inverse Fourier transformation. The latter operation is realized practically in classical optical microscopy by collection and superposition of the diffracted components in the image plane using appropriate optics.

subsection*The evanescent components The optical limit becomes apparent when the structure of the object is smaller than roughly the half of the wavelength: $d < \lambda/2$. In this case equation (2.5) has no real-number solution, which means that formally no diffracted-order wave can propagate and thus no information is detected in the far-field. Instead, the coefficient γ becomes imaginary, and equation (2.3) represents an *evanescent* field which is decreasing exponentially in the z -direction with a decay length $z_{1/e}$ determined by $\exp(-|k_x, k_y|z_0)$. This means that for very high spatial frequencies the information on the object structure disappears at a distance of the order of a wavelength λ from the sample surface. Hence, the minimum spatial structure that can be observed is given by the limit of Abbe which can be expressed in terms of wave vector components as

$$d_{min} \simeq \frac{2\pi}{\sqrt{(k_x^2 + k_y^2)}} \quad . \quad (2.6)$$

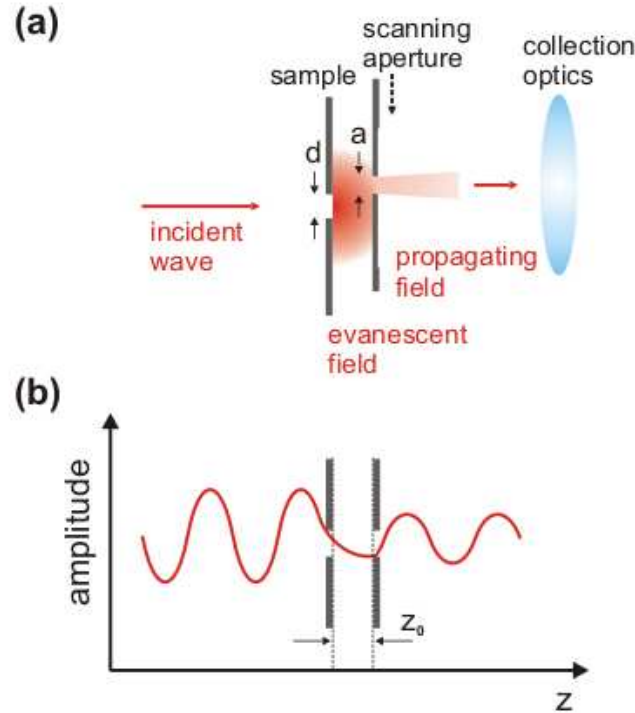


FIGURE 2.2: The SNOM principle; (a) a nanosized aperture is scanned along the sample surface at nearfield distance, (b) the dielectric probe material generates propagating waves from the evanescent field.

If, by contrast, the detection is performed at a close distance below the decay length $z_{1/e}$, all the components of the electric field (2.3) can be collected, and a reconstruction of the object structure is possible with a spatial resolution below the wavelength of the light. This condition defines the region of the so-called optical nearfield [31].

2.2.1 Probing the evanescent field

Considering a model sample grating with a lattice parameter of sub-wavelength dimension $d < \lambda$ being illuminated in transmission, all the Fourier components behind the sheet are diffracted into the evanescent field. If a dielectric probe, e.g. an aperture with a substantially smaller diameter $a < d$ is scanned along the sample at a distance $z < \lambda$, as is illustrated in Fig. 2.2 (a), the evanescent field is transformed into a propagating field (Fig. 2.2 (b)), and a pattern of (integrated) intensity can be detected in the far-field as a function of the position of the probe, which represents an image of the material structure of the object [31]. The resolution of this intensity profile is limited only by the dimensions of the aperture.

Practically, an aperture probe with a sub-wavelength diameter can be realized by an optical fiber tip with an apex of some 10 nm. The function of such fiber tips as efficient nearfield probes relies on a combination of two effects: on the one hand, the dielectric material of the tip generates a propagating electromagnetic wave by means of dipole interaction with the oscillating evanescent field. On the other hand, the core of the optical fiber is suited to guide the generated waves to the detector, this way diminishing further losses due to stray propagation. The obtained spatial resolution and the transmission efficiency of the probes depend essentially on the shape of their cone and the particular conditions at the apex [38]. In general, a transfer function of Gaussian character can be assumed for the light transmission of the aperture, whose full-width at half maximum (FWHM) intensity gives a lateral resolution of about $\lambda/5$, typically [44].

The change of the core structure of the optical fiber in between the waveguide and the apex of the tip leads to a successive constriction of the propagation conditions for the electromagnetic waves². In a quantum-mechanical photon picture, the classically forbidden zone at the front end of the tip presents a potential gap that has to be passed by the photons by means of tunneling³ to find conditions which allow the field to propagate again, as shown schematically in Fig. 2.3. The intensity of the photon current across this gap depends strongly on the tunneling distance, showing an exponential decrease with the gap width z_0 . Accordingly, the fabrication method, which has a significant effect on the cone angle and the structure of the fiber tip, determines largely the obtained transmission efficiency and spatial resolution [45].

The preparation of a nanosized fiber tip can be performed technologically either by local heating of the fiber with, e.g., a focused high-power CO₂ laser beam and parallel pulling it up to rupture [46], or by chemical etching with hydrofluoric acid [47]. In general, the chemical etching method generates larger cone angles than the pipette-pulling method [44]. Additionally, both methods exert a different effect on the material of the optical fiber: whereas by the etching process the waveguide is simply cut, during the pipette-pulling treatment the complete fiber is melted and thinned out, thus leading to different boundary conditions for the electromagnetic field within the material. Therefore etched tips generally have a considerably shorter photon tunneling length than pulled tips, hence resulting in a higher transmission efficiency [44]. On the other hand, the latter ones normally show a higher spatial resolution.

An effective method to increase the spatial resolution of optical fiber tips is by coating with a metal film, which additionally helps to suppress stray light from the surrounding area [40]. A metal coating is applied normally by beam evaporation in high vacuum in an inclined angle from behind. In a simple geometrical

²This narrowing region can be characterized as an adiabatic conical waveguide [38].

³This photon tunneling phenomenon is well-known from the attenuated total reflectance effect.

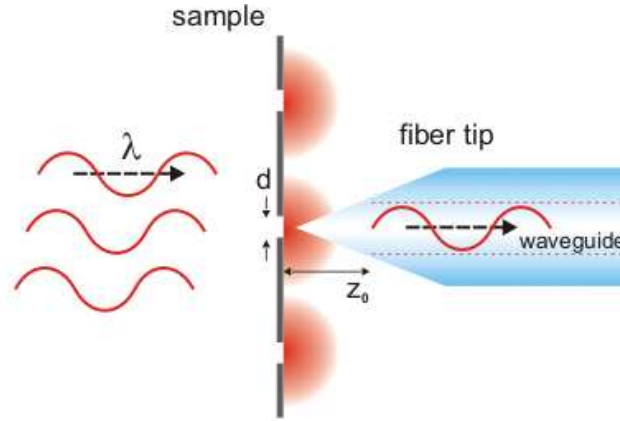


FIGURE 2.3: Probing of the evanescent field with an optical fiber tip. The distance z_0 between the investigated structure and the optical waveguide within the fiber gives the photon tunneling length.

model treating coated fiber tips as ideal point-detectors or emitters, for the signal intensity I_R from a point on the sample surface in a lateral distance R a relation $I_R \sim 1/R^4$ is obtained. This means a very fast decrease of the background signal, even for small distances R , and thus a high spatial resolution [45]. Ideally, a metal-coated fiber tip serves as a perfect nano-aperture, assuming that the obtained spatial resolution is determined solely by the diameter of the aperture hole at the apex. Real tips, however, display a lesser resolution of the order of several tens of nanometers, typically [48]. The reason for this is, firstly, that for any practical application a compromise has to be made between spatial resolution and signal intensity. Since the transmission I of an aperture is related to its diameter $d_{aperture}$ by $I \sim d_{aperture}^2$, in order to get an equal signal amplitude with a smaller aperture it would require a correspondingly squared measurement time, which soon runs into practical limitations. Secondly, the condition of continuity of the electromagnetic wave function at the material interface necessitates a leaking of the field into the coating material, and thus a widening of the nearfield spot, even if an aperture with a virtually infinitesimal diameter $d \simeq 0$ could be prepared without getting any loss of signal intensity. The extent of this effect can be determined from the skin depth δ of the coating material

$$\delta = \frac{1}{\sqrt{\pi f \mu_0 \mu_r \sigma}} \quad , \quad (2.7)$$

with the frequency f of the electromagnetic wave, $\mu_0 \mu_r$ the permeability of the coating material, and the specific conductivity σ [49].

2.2.2 SNOM configurations

The optical pathway in a SNOM experiment is usually put into practice by an arrangement of optical fibers ending in the central fiber tip probe which can be used either to conduct light towards the sample surface, or to collect the luminescence signal. Correspondingly, a SNOM can be realized in principle in collection or excitation mode either in reflection or transmission configuration, depending on the sample properties and the particular experimental task, as shown schematically in Fig. 2.4 (a), (b), (d), and (e). A special configuration is the so-called dark-field mode, which makes use of the attenuated internal reflection effect to generate an evanescent field, as illustrated in Fig. 2.4 (f) [50]. Whether the fiber tip is used for sample illumination or for signal collection is equivalent with respect to the nearfield effect [51]. However, in practice the properties of the sample and the particular experimental task must be taken into consideration. An inequivalency of collection and illumination mode can result, e.g., from drift

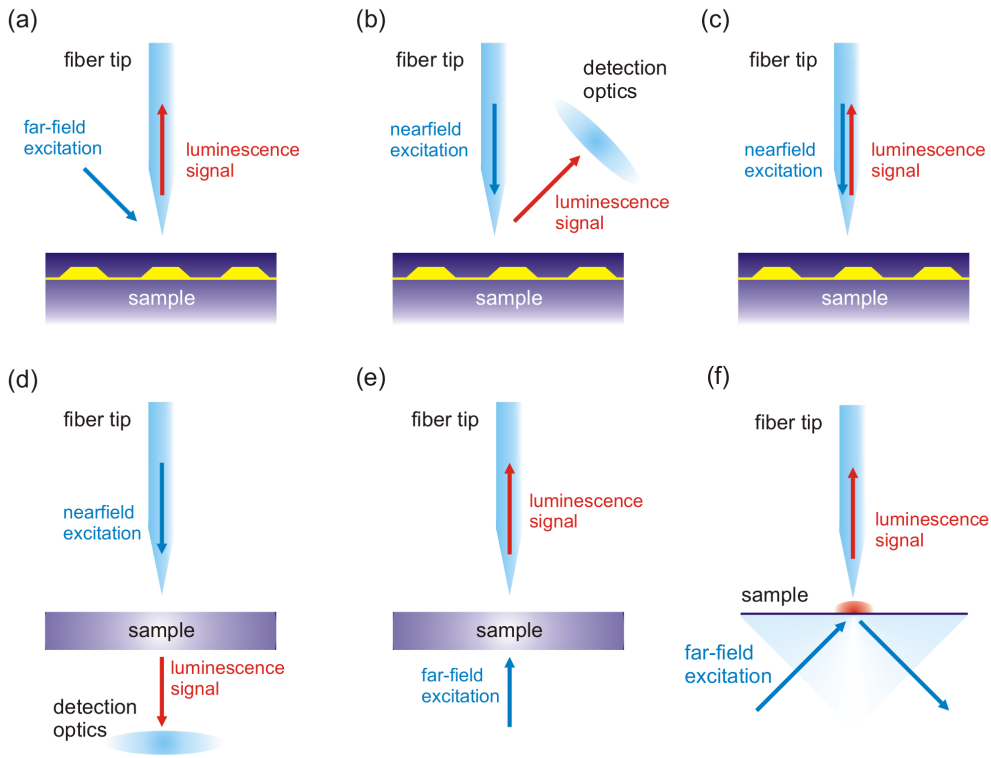


FIGURE 2.4: Common SNOM configurations; (a) reflection-collection, (b) reflection-excitation, (c) internal reflection, (d) transmission-excitation, (e) transmission-collection, (f) dark-field mode.

processes of carriers within the sample material: while in collection mode the fiber tip functions as a local selector for the luminescence signal that is emitted

from a certain sample area, in illumination mode the carriers are excited locally through the nano-aperture, but may diffuse within a conductive sample into a broader area before recombination, this way wiping out the nano-scopic capacity of the technique. On the other hand, this effect provides a possibility to investigate specific parameters such as the diffusion length of the carriers in the material [44, 45].

In particular when uncoated fiber tips are used in a SNOM experiment, a side-ward penetration of light through the tip cone will overlay the signal from the tip apex, which can severely affect the obtained information. An arrangement which is particularly suited to reducing this background signal is the combination of the above mentioned configurations in the so-called internal reflection mode, as it is shown in Fig. 2.4 (c), which was used in the frame of this work for the investigations on semiconductor quantum dots. Since in this configuration the fiber tip has to be passed twice by the light, a considerably enhanced spatial resolution can be obtained, in comparison to a one-way transmission configuration [40]. If a Gaussian profile is assumed for a transmission of the aperture, the spatial distribution of the obtained signal intensity is given by a convolution of the Gaussian with itself, which again is a Gaussian profile but with a FWHM that is reduced by a factor of $\sqrt{2}$ [52]. This way, often an individual investigation of densely packed objects as, e.g., quantum dots is possible even with uncoated fiber tips [29, 53]. Additionally, the internal reflection configuration has the advantage of compactness and easy handling.

2.2.3 Noble-metal tip nearfield antennas

Alternatively, instead of an optical fiber tip a dielectric scatterer, e.g., a sharp metal tip can be used to probe the nearfield of a sample in the so-called apertureless configuration [54, 55]. The evanescent field induces an oscillating dipole moment within the tip material, this way stimulating the emission of propagating waves which can be detected in the far-field, as it is shown schematically in Fig. 2.5. Since normally a metal tip can be prepared with a smaller apex diameter than an optical fiber tip, a considerable improvement in spatial resolution can be achieved [56]. However, this benefit has to be weighed up against practical disadvantages such as a more difficult handling, sensitivity on the wavelength, and polarisation of the light, and a particular dependence on the geometry of the probe [57]. In particular, the filtering of the signal against unwanted stray light is more difficult, in comparison with the conventional fiber tip technology.

A substantial enhancement of the detected signal can be achieved with a metal nearfield probe if the process takes place at resonance with the plasmon frequency of the tip material [58–60]. In a small metal structure such as a nanoparticle or a sufficiently sharp tip, an incoming electromagnetic wave of appropriate wavelength can couple to the electron gas of the material, thus generating so-called *plasmon-polaritons* or *plasmons* [61]. The excitation of plasmons corresponds to

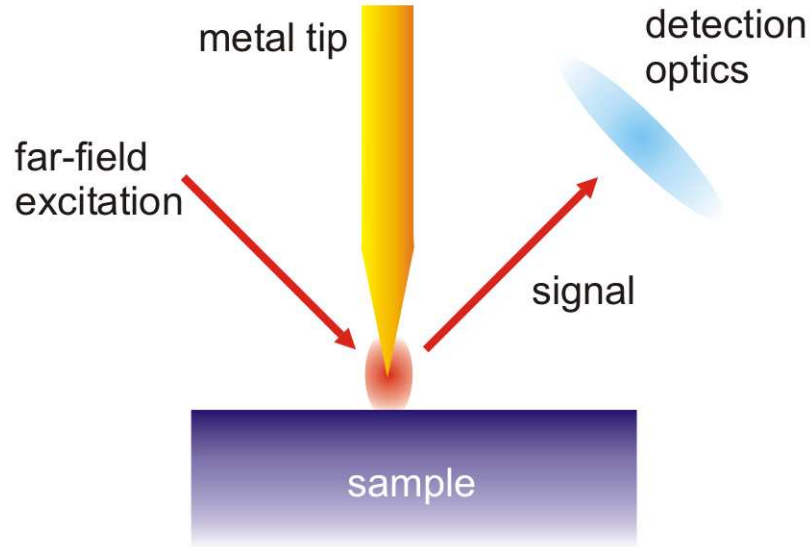


FIGURE 2.5: The principle of apertureless SNOM: a nanosized scattering object such as a metal tip is used to probe the evanescent field. The scattered light is detected using far-field optics.

a resonant amplification of the electrical nearfield of the particle [62]. This is possible because in a dimension-reduced geometry an additional wave vector transfer between the photon and the plasmonic state may occur, while at an ideally flat surface no interaction between them is allowed under conservation of energy and the wave vector [63, 64]. The resonance generally depends on a number of specific parameters, such as the material of the particle and the surrounding, the size and the shape of the particle, and in the special case of a material alloy, on its stoichiometry also [3, 65]. In a classical electrodynamic description the optical properties of a dielectric sphere are determined calculating the electrical polarizability by multipole expansion of the electric potentials of the particle and its surrounding space, solving the obtained Laplace equation in both media [66]. A basic calculation was performed in the context of this work for nano-sized Au particles, showing that for this commonly used tip material, a strong plasmon resonance can be expected at wavelengths of 700 nm – 900 nm [67].

An analog calculation can be carried out for other metal nanostructures, as for example the apex of a scanning probe [68, 69]. In that case the elongated geometry of the tip has to be taken into account, which can lead to a varied plasmon frequency in comparison to the spherical particle, a broadening of the resonance, or to a considerable polarization anisotropy, in particular.

Additionally, when the metal tip is brought close to a dielectric surface, the

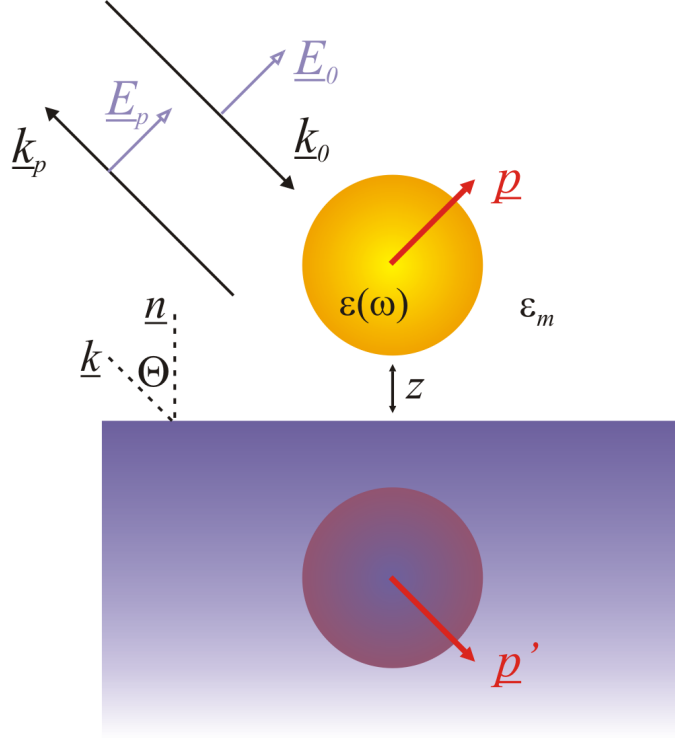


FIGURE 2.6: Model of a metal sphere at close distance to a metal surface. The dipole moment of the sphere induces an image dipole within the sample. The calculation yields an angle-dependent amplitude of the scattered electromagnetic field.

electromagnetic coupling between both must be regarded [68, 69]. In this configuration the tip is represented by a sphere at a very close distance above an ideal metal surface, as illustrated by Fig. 2.6, and the electromagnetic field $\vec{E}(\vec{r}, \omega)$ at a distance $r = |\vec{r}|$ is calculated by an expansion of Green functions of the geometry: an external field \vec{E}_0 induces a dipole moment $\vec{p} = \alpha_p \vec{E}_0$ within the sphere material, resulting in a field $\vec{E}_p(\vec{r})$ of:

$$\vec{E}_p(\vec{r}) = \frac{3(\vec{d} \cdot \vec{p})\vec{d} - \vec{p}}{|\vec{r} - \vec{r}_p|^3} \quad (2.8)$$

with the position \vec{r}_p of the dipole and the distance $\vec{d} = (\vec{r} - \vec{r}_p)/|\vec{r} - \vec{r}_p|$. If the distance between the sphere and the surface is small, the virtual image dipole induced within the sample interacts with the dipole moment of the sphere. Thus, the dipole of the sphere becomes $\vec{p} = \alpha_p(\vec{E}_0 + \vec{E}'(\vec{r}_p))$, with the field of the image dipole $\vec{E}'(\vec{r}_p)$. If the external field is a plane wave with the wave vector incident under an angle Θ against the normal \vec{n} of the sample surface, being polarized linearly in the plane of incidence, the calculation yields an angle-dependent gain

factor $F(\Theta) \sim 1/(1+\cos^2(\Theta))$ for the scattered wave, which is determined further by the dielectric functions of the sphere and the sample material, the distance between sphere and sample surface, and the diameter of the sphere [61].

2.3 Distance control

2.3.1 The shear-force feedback

Optical nearfield microscopy requires a technology that is suitable to control the gap between the sample surface and the probe during a spatial scan with nm-precision [46]. The common way to accomplish this is by using the so-called shear-force feedback technology [70–72]. Within a very close distance of some tens of nanometers, the mechanical interaction between the sample surface and a laterally oscillating probe leads to a damping of the oscillation [73–75]. This effect can be observed in the form of a distance-dependent attenuation of the amplitude, a shift of the resonance frequency, and a phase shift between the driving oscillation and the response. Because these parameters show a distinct, monotonic dependence on the amount of contact with the surface, each of them is suited as a feedback signal for distance control [76, 77]. The exact physical origin of the shear-force is a subject of ongoing debate [78–87]. Nevertheless, in recent years this method of distance control has been established widely. Very often the technology is realized using a tuning fork set-up, taking advantage of the mechanical resonance of a standard quartz tuning fork timer with a high quality factor Q [73]. Practically, the optical fiber tip is applied to one of the prongs of the tuning fork in a way that allows a lateral oscillation relative to the sample surface, as is schematically shown in Fig. 2.7. The oscillation can be

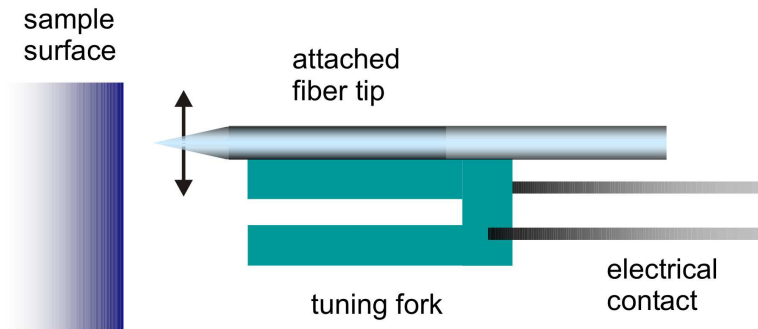


FIGURE 2.7: Distance control using a fiber tip attached to an oscillating tuning fork. The oscillation is attenuated by means of shear-force contact of the tip with the sample surface.

triggered, e.g., by an oscillating voltage applied to the tuning fork, which leads to oscillating charges at its electrodes thus inducing a correspondingly periodic deformation of the piezoelectric material, and vice versa [37]. In order to control the distance, the behavior of the system is monitored while the tip approaches perpendicular to the sample surface. The measured response is used as reference for the mechanical actuators which control the position of the tip or sample in terms of a negative feedback loop [72].

2.3.2 The tuning fork oscillator model

For small amplitudes $x(t)$ the oscillating probe can be described effectively as a driven harmonic oscillator [37]. In this model, the complete equation of motion of a tuning fork with an attached fiber tip in interaction with the sample surface reads as:

$$m\ddot{x}(d, t) + m\gamma(d)\dot{x}(d, t) + m\omega_0^2(d)x(d, t) = Fe^{-i\omega t} \quad , \quad (2.9)$$

with the resonance frequency $f_0 = \omega_0/2\pi$ of the free system, the damping constant γ , and a periodic driving force $Fe^{-i\omega t}$, with a constant amplitude F and angular velocity ω . The parameter d indicates the dependence on the probe-sample distance [37]. The amplitude x_0 of the corresponding oscillatory solution $x(t) = x_0(\omega) \cdot e^{-i\omega t}$ of Eq. (2.9) is a function of the excitation frequency ω , which follows a Lorentzian form:

$$x_0(\omega) = \frac{(F/m)}{\sqrt{(\omega_0^2 - \omega^2)^2 + \omega_0^2\omega^2/3Q^2}} \quad , \quad (2.10)$$

with the *quality factor* Q , which is a measure for the damping of the oscillation, being represented by the width of the resonance curve. The quality factor is defined by

$$Q = \frac{\omega_0}{\gamma\sqrt{3}} = \frac{f_0}{\Delta f} \quad , \quad (2.11)$$

where the FWHM of the curve is read as the characteristic frequency bandwidth Δf of the resonance. The corresponding phase $\phi_0(\omega)$ of the oscillation is expressed in terms of the Q -factor as

$$\phi_0(\omega) = \tan^{-1} \left[\frac{\omega_0\omega}{\sqrt{3}Q(\omega_0^2 - \omega^2)} \right] \quad , \quad (2.12)$$

thus following an *arctangent*-like characteristic. Accordingly, a reduction of the quality factor Q due to a damping of the oscillation leads to a lowering of the oscillation amplitude $x(t)$, and a broadening of the resonance function $x_0(\omega)$, together with a shift of the peak resonance frequency ω_{rod} , or a flattening of the phase function $\phi_0(\omega)$, respectively [49, 72].

Because there is effectively no center of mass motion occurring in the contralateral

oscillation of the prongs, the Q -factor of a free tuning fork is very high, showing values of the order of $10^3 - 10^4$ at ambient conditions, typically⁴ [73]. Regarding the reduction of the resonance quality due to surface contact: in the model introduced above, the damping constant γ and the spring constant $k = m\omega_0^2$ have two different contributions each: an intrinsic part, which is associated with the properties of the tuning fork itself, and an external contribution which is induced by probe-sample interaction [37].

Further, the shear interaction of the oscillating probe with the sample surface generates two types of forces: (1) a dissipative force $F_{int}^{friction}$, which is of friction type, and is expressed in the second term in Eq. (2.9), and (2) an elastic reaction $F_{int}^{elastic}$ which is associated with the third term in Eq. (2.9). An estimation of the respective contributions for a commonly used 32.768 kHz tuning fork timer with an intrinsic spring constant $k_{stat} = 40$ kN/m yields a dissipative friction of the order of some tens of pN, and a considerably larger elastic reaction of more than 100 pN [37].

Generally, for scanning probe experiments a sensitive distance control is required, which additionally has to be as fast as possible to permit time-efficient measurements but prevent tip or sample damage by accidental crash. Unfortunately, a short response time and a high sensitivity of the feedback counteract each other in principle, and a compromise has to be found between the two [37, 73]. In general, a high Q -factor is a prerequisite for high sensitivity of the shear-force feedback system [72]. On the other hand, the higher the quality factor of an oscillating system, the longer it takes to change to a new steady state and thus to respond to an external impact. With the solution of Eq. (2.9) written as $x(t) = x_0 \cos(\omega t + \phi_0)$ in terms of x_0 and ϕ_0 , the response of the oscillatory system to a sudden perturbation is described by

$$x(t) = x_t e^{-\omega'_0 \frac{t}{\tau}} \cos(\omega t + \phi_t) + x'_0 \cos(\omega t + \phi'_0) \quad , \quad (2.13)$$

for a variation of the resonance frequency from ω_0 to ω'_0 at the time $t = 0$ [88]. This function consists of a transient term $x_t e^{-\omega'_0 t / \tau} \cos(\omega t + \phi_t)$ describing the transition from the initial state to the new stable oscillation, and the term $x'_0 \cos(\omega t + \phi'_0)$ describing the new steady state. According to this interpretation, the response time τ of the system to a perturbation at $t = 0$ can be defined as

$$\tau = \frac{2\sqrt{3}Q}{\omega'_0} \approx \frac{2\sqrt{3}Q}{\omega_0} \quad . \quad (2.14)$$

Thus it can be concluded that it takes about $2Q$ oscillation cycles for a tuning fork to reach a new steady state in response to a sudden change of distance, which determines the lower limit of processing for the scanning distance control. For a usual 32.768 kHz tuning fork with a typical Q -factor of about ~ 3000 , this limit

⁴The value can be several orders of magnitude higher in vacuum [37].

is given by a response time in the order of 300 ms at ambient conditions [37]. However, an extremely sensitive feedback is not always necessary. At the cost of a slow degradation of the tip or surface quality, the experiments can be carried out remarkably faster using a more robust feedback, when the topography of the sample surface is not of primary interest for the investigation. This is possible for example in the investigation of buried semiconductor quantum dots with a low density, and a cap layer in the order of 50 – 100 nm which is limiting the spatial resolution anyway.

At low temperatures the quality factor Q of the tuning fork oscillators is increased considerably [89]. According to the theory of Debye, at temperatures T below the Debye temperature θ , the heat capacity C_V of a solid material is proportional to T^3 [17]. Because of this strong dependency the ability of the tuning fork crystal to dissipate kinetic energy into phonon excitations is almost completely suppressed, which is equivalent to a very low amount of intrinsic damping, thus resulting in an extremely strong resonance oscillation with a very low bandwidth. Therefore at very low temperatures the surface contact is almost purely elastic, which forces the system to either get literally frozen in a complete deadlock, or to transfer the kinetic energy of the oscillation into the material and break. At temperatures below 10 K the bandwidth of a usual 32.768 kHz tuning fork is typically reduced to less than 0.1 mHz. An oscillatory adaptation of the system to a shift of the excitation frequency is hardly possible, which leads to a situation of a random excitation of oscillations when the driving oscillation does not match the resonance frequency steadily with according precision. In practice, the impact of external vibrations, as well as the enhanced thermal sensitivity of the experimental setup at low temperatures add to this problem. Therefore an artificial reduction of the tuning fork quality factor can be necessary to ensure sufficiently stable scanning distance control [73, 90, 91].

In general, the experimental arrangement for the distance control has the structure of a negative feedback loop [72, 92]. The probe is triggered to oscillate resonantly lateral to the sample surface, being driven either electrically by an oscillating voltage which is applied directly, or by mechanical shaking using an oscillating piezo crystal which is mounted to it [37]. Because of the piezoelectrical coupling, the oscillating deformation of the prongs induces an oscillating voltage which can be measured between the contact pads of the tuning fork [37, 72]. This high-frequency signal is filtered for contact-induced perturbations using a lock-in amplifier, and the recorded modulations are processed further by a distance control electronics in terms of a negative feedback signal for the regulation of the distance between probe and sample with the respective piezo actuators [72, 92]. Regulating for a constant set-point value of the shear-force feedback signal, an intended scanning distance can be maintained. Figure 2.8 shows the feedback circuit schematically. If the amplitude of the oscillation is taken as control parameter, a single lock-in amplifier is used to filter the voltage that is picked up from the contact pads of the tuning fork. The lock-in amplifier is operated syn-

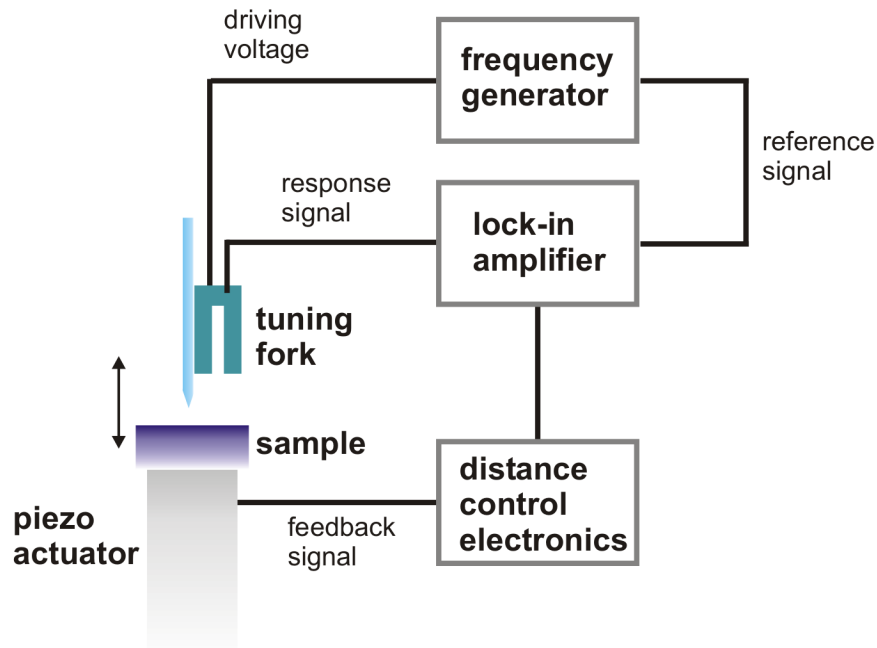


FIGURE 2.8: Diagram of the distance control circuit. The tuning fork is driven close to resonance, and the response signal is processed in terms of a negative feedback loop to control the distance using piezo actuators.

chronous with to the tuning fork oscillation, with the excitation frequency taken as reference [92]. This technique can be characterized as highly reliable, but has the disadvantage of a relatively long response time if the quality factor of the tuning fork is high [37, 73]. Nevertheless, due to the relative robustness of the signal, this is the favorable way of distance control for low-temperature measurements, provided that the quality factor can be tuned appropriately [73, 91].

In contrast, a measurement of the more rapid and monotonically changing frequency or phase shift can be a favorable alternative to achieve a faster distance control, which is frequently used, e.g., to image the morphological properties of particularly sensitive materials, or when working with ductile Au tips [37, 76, 93]. Furthermore, a distance control in the so-called phase-locked loop responds more sensitively to viscous friction-like forces on the sample surface, which allows the imaging of chemical properties which are unaccessible with the amplitude feedback [94]. A monitoring of the phase requires an electrical comparison of the phase of the reference voltage with that of the tuning fork oscillation, which can be realized using a two-phase lock-in amplifier [92].

In a very general sense, the electrically driven tuning fork oscillator may be

regarded as a variable capacitor, being part of a RLC -circuit, which is shown schematically in Fig. 2.9. Thus, in principle a variation of the quality factor of the combined system should be possible, either with a varied resistance within the electrical circuit, or by means of an appropriate mechanical damping of the fork oscillation. Concerning the bandwidth of the oscillation, however, the elec-

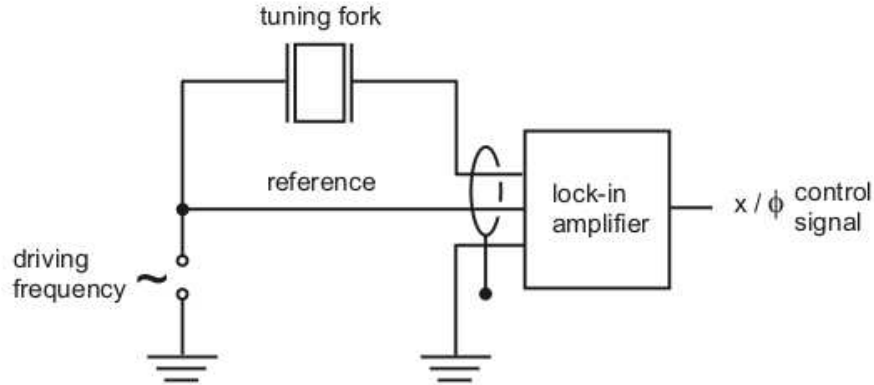


FIGURE 2.9: Circuit diagram of the distance control. The tuning fork is symbolized as a variable capacitor.

trical and the mechanical component have to be considered as separate systems [92, 95, 96]. The electrical circuit merely provides an external excitation source for the tuning fork, and the amount of dissipation within the electrical circuit has no influence on the quality factor of the mechanical resonance. The transmission bandwidth is limited by the bandwidth of the tuning fork. [92, 95, 96]. Thus, a considerable reduction of the quality factor of the scanning probe can only be achieved by means of a damping of the mechanical oscillation directly [73, 90–92, 96].

In general, the resonance frequency ω_0 of the oscillating probe is determined essentially by the elastic module of the tuning fork, while the bandwidth Δf of the oscillation response depends on the rate of dissipation that occurs when the material is deformed [72, 73]. The latter is described abstractly by the rate-dependent loss module $G \sim \omega_f$, with the rate ω_f of an oscillating force $F(t) = \hat{F} \cdot \sin(\omega t)$ acting on the material [97]. Since the amount of viscous dissipation occurring within the glue that is used to mount the fiber tip is considerably higher than within the tuning fork material, a mechanical tuning of the quality factor is possible by means of an appropriate adjustment of the viscoelastic properties of the glue.

2.3.3 Alternative techniques for distance control

An alternative way to control the distance between the nearfield probe and the sample is by using the tunneling current of carriers for feedback, as it is done

in STM [98]. Since this method requires conductive probe and sample materials, it can be applied to optical nearfield microscopy in principle only when metal-coated fiber tips or pure metal tips are used. Moreover, the oxidation or contamination of the sample surface with water or dust impede the use of a tunneling based distance control at ambient air, and requires UHV conditions [99]. The requirement of a conducting sample material can cause further problems for scanning optical investigations, due to a weaker luminescence intensity [99, 100]. In the case of semiconducting materials, often a strong doping is necessary in order to provide sufficient conductivity to permit tunneling, which in turn tends to inhibit the propagation of light, and this way attenuates the signal intensity. As a further problem for optical nearfield microscopy under tunneling distance control, the carriers injected into the sample represent an additional source of noise for the optically excited luminescence signal. This is not likely to happen for systems such as, e.g., buried semiconductor quantum dots which are capped typically by about 50 – 100 nm semiconductor material, since the injected carriers will get trapped easily by surface states, or recombine with doping atoms before approaching the quantum dot layer [100]. However, the electric field of the additional carriers may influence the electronic states within the luminescent structure in terms of a Stark shift, and in this way interfere with the optical information [53].

Another possibility is the use of an optical feedback, which has proven to provide a suitable method to control the scanning distance in different configurations [101, 102]. In internal reflection geometry, an optical feedback is possible when using uncoated fiber tips, which display nearly no back-reflection of light from the inside of the cone region [38]. In this configuration, the intensity of light that is reflected back from the sample surface into the fiber shows an approximately exponential dependence on the distance, with a half-power length of about 250 nm, typically [101]. Depending on the quality of the tip, the exponential relation can be modulated in some cases by oscillations which result from an optical interference of immitted and reflected light.

Another way to realize an optical feedback is based on the shadowing of laterally strayed light by a SNOM probe which is approached to the sample surface [102]. This method depends on the use of a coated fiber tip to achieve a sharp-cut shadowing. The intensity of the reflected signal which can be observed by an extra detection optics in the far-field shows a successive decrease with decreasing tip-sample distance. Also in this configuration a periodic oscillation of the intensity is observed, which interferes with the observed intensity, depending on the distance. Because of the relatively low intensities, to implement the technique the signal has to be collected precisely from the region of the tip apex, which requires an accurately adjusted high-aperture optic.

In essence, any optical technique brings up a number of specific difficulties, which have to be weighed up carefully against the prospective benefits, if they are to substitute for a mechanically based feedback. One major obstacle is that they

often require additional optical components which consume rare space, which can be critical for tiny setups that are operated, e.g., in small cryostates. This holds particularly for the shadowing method which relies on a precise focusing to the tip, and thus an optical access to the setup *in-situ*. Furthermore, a possible perturbation of the measurement by the feedback signal has to be taken into account. While on the one hand an unwanted extra excitation of the investigated sample can occur, on the other hand, a variation of the excitation intensity may lead to a perturbation of the feedback signal, which has to be balanced out by frequent, laborious re-calibration. Even though these problems can be successfully by-passed using lock-in technology, or pulsed excitation as like in time-resolved measurements [101], such a solution depends on costly extra instrumentation. In general, an optical distance control technique suffers from surface irregularities and pollution just as does a mechanical method, as well as from modifications or degradation of the tip due to continuous or accidental mechanical contact during a scan. For these reasons, an optical method does not essentially provide a better solution if a sufficiently reliable mechanical feedback can be established.

Chapter 3

Development of the low-temperature SNOM

3.1 Assessment of the system

In the frame of this work a scanning nearfield optical microscope (SNOM) for the investigation of semiconductor nanostructures was constructed, which is suited particularly for measurements at low temperatures. The design that was chosen for this purpose is based on the cooling of the SNOM in full, in a helium flow cryostate. This approach sets a number of boundary conditions for the structure of the setup, whilst still providing considerable advantages over alternative techniques, especially regarding the general handling of the setup, and the conditions needed to establish constructional stability. However, the construction implies a number of specific technological problems which have to be solved as a prerequisite for reliable operation. For that reason, there exist up to now only a few functioning realizations of a low-temperature SNOM which rely on this principle [31, 90, 103].

For the cooling of the experimental setup a helium flow cryostate type Cryovac KONTI-Spektro with a cylindrical measurement chamber of 350 mm in height, and a diameter of 22 mm was available [45]. Figure 3.1 shows a sketch of the cryostate and the cooling circuit. The measurement chamber can be flushed with helium which acts as a contact gas transporting thermal energy to the heat exchanger. An isolation vacuum of about 10^{-4} Pa between the measurement chamber and the exterior wall of the cryostate helps to reduce heat conductance and convection. An additional isolation against thermal radiation is provided by a cooled heat shield around the chamber. Visual access to the measurement chamber is possible through four windows placed at an interior level of 35 mm. A heater is placed at the lower part of the chamber, which allows heating of the chamber contra the cooling helium flow, thus permitting experimentation at controlled temperatures between 4 K and 300 K. The actual temperature within

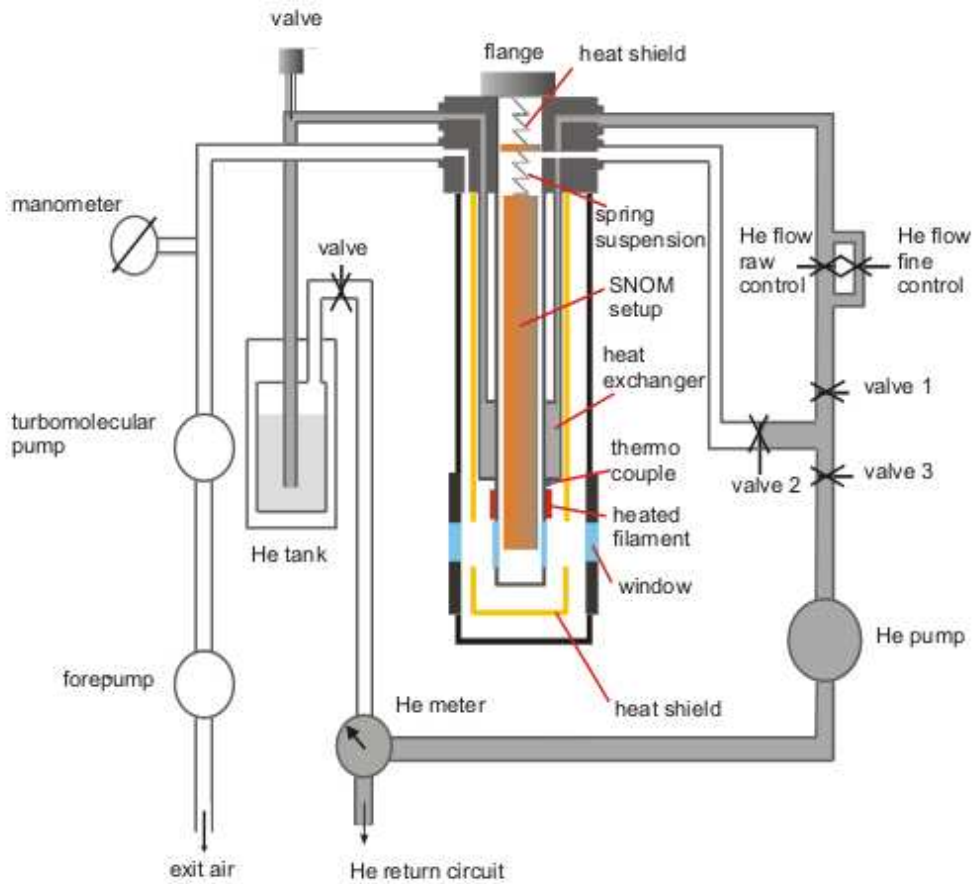


FIGURE 3.1: Diagram of the cryostat and the associated cooling circuit. The SNOM setup is suspended within the measurement chamber which can be flushed with helium by use of valve 2.

the chamber can be determined with a Si-diode at the chamber wall close to the heat exchanger and the windows.

The narrow dimensions of the cryostat compel an extremely compact, vertically oriented design. The measurement chamber does not provide enough space for a horizontal arrangement of tip and sample with the well-trying piezo tube scanner which has to be relatively large to render a reasonable scanning area of some micrometers (μm) at low temperatures, together with sufficient vibration stability. The limited bending radius of the optical fiber adds to this condition. Because of the limited space, the internal reflection mode is preferable, which makes dual use of the fiber tip for excitation and signal collection. This configuration has the additional advantage of compactness and easy handling. Since, for reasons of stability, further the tube scanner should be chosen to scan the sample rather than the tuning fork with the attached probe, the basic structure of the

low-temperature SNOM within the given cryostate is characterized by a vertical arrangement, with the sample at the bottom being carried by the scanner, and the fiber tip fixed opposing it from top.

However, this setup compels also a vertical coarse approach of probe and sample, which sets one of the technological problems to be solved. Furthermore, in the given case a direct optical control of the experiment becomes critical because the low position of the windows of the cryostate permit only minimum space for a direct visual access to the experiment.

At temperatures of a few K an efficient thermal isolation is necessary in order to reduce local temperature fluctuations which can strongly affect the sensitive distance control thus leading to considerable perturbation of scanning probe measurements [90]. However, it is almost impossible to suppress such thermal fluctuations within a helium flow cryostate completely [90]. A number of different effects have to be taken into account to accomplish sufficient thermal stability. Besides the basic thermal isolation that is provided by the cryostate, a primary issue is to minimize heat conduction by the electric wiring of the setup, which can represent a potent thermal contact to the environment. Therefore, the wiring is made of extremely thin wires which are connected to the outside by extra insulated pin connections in the top flange of the cryostate¹. Secondly, the thermal radiation passing through the windows and from the top flange of the cryostate may lead to local heating, as well as the potential entry of energy by the laser light used for the photoluminescence excitation. A copper heat shield as part of the setup suspension is used to reduce heat radiation from the top flange of the cryostate. An entry of heat radiation is minimized further by the heat-absorbing material of the windows which can be covered additionally with aluminum foil during a measurement. Then, the cylindrical shape of the cryostate facilitates the appearance of streams of convection of the contact gas. These can be triggered by heat conduction via the setup suspension and the wiring, and particularly by the use of the heater for temperature adjustment. It is enhanced further as the setup occupies a considerable amount of space within the measurement chamber, thus creating narrow convection channels. Accordingly, the construction of a slim and open setup helps to reduce this effect.

3.2 Low-temperature implementation concept

3.2.1 The inertial drive

The execution of scanning probe experiments requires a technology which allows the movement of components of the microscopy setup with nm-precision, and the maintenance of their position with equal stability. Piezoelectric actuators pro-

¹By contrast, the influence of electrical currents feeding the piezo positioners and the tuning fork is minimal, since the piezo elements are actuated at high voltage but low current.

vide the only practically possible way to cope with these requirements within a cryostate or in an ultra-high vacuum. Most commonly, the so-called inertial drive technology is used to approach the tip and the sample of a scanning probe microscope, which relies on a delicate balance of inertial force and friction [104, 105]. Therefore, a so-called walker slide is mounted by means of a low-friction support to a set of piezo elements which are actuated to deform by an applied periodic voltage of asymmetric shape, such as e.g., a saw tooth. At appropriate frequency the deformation of the piezo actuators shifts the walker over a typical distance of some 100 nm, along with the long ramp of the voltage, while the following sudden switch to the steep-edged gradient triggers a jerky snap of the piezo elements back in the opposite direction, against which the inertial walker resists. This way, the walker is moved in stepwise stick-and-slide motion over macroscopic distances. This technology has proven reliable functioning in different configurations, but is applied with good success usually for horizontal motion.

Due to the dimensions of the cryostate, in the given case the conventional walker design is not suitable for the low-temperature SNOM, and a more space-saving drive had to be developed for a vertically run coarse approach of tip and sample. Since in the vertical, the relation of the involved forces of inertia and friction is much more delicate, and the construction has to be balanced out a lot more precisely than in the horizontal. For that reason, currently just a few realizations of a piezo-based vertical coarse motion have been developed which are working reliably [106]. Low-temperature conditions add specific further problems: on the one hand, the balance of the gravitational impact and friction is changed considerably due to the modification of the mechanical characteristics and the surface properties of the components, while on the other hand the efficiency of the piezo effect decreases significantly with decreasing temperatures. The changed conditions can lead to a critical interdependency of specific operation parameters for the coarse approach, e.g., the amplitude or the frequency of the applied voltage, and the actual temperature.

3.2.2 Approaches to a technical solution

As a first attempt to realize a vertical coarse approach within the limited space of the cryostate, a technology was developed which is making use of the inertial force of a highly accelerated mass driving the walker in a hammer-propulsion manner, which is described in detail in [45]. In the given setting the walker consists of a hardened-steel bar which is drawn up extra straight to ensure maximum axial force transmission, being held in the vertical by magnetic mounting. The inertial mass is mounted axially at the lower end of the bar onto a piezo tube actuator, as shown in Fig. 3.2. The driving force is generated by a periodic parabola voltage, which triggers a corresponding contraction of the piezo tube, and in this way a jerk acceleration of the inertial mass at the moment of switch between two consecutive parabolae. This technology has proven principle functioning,

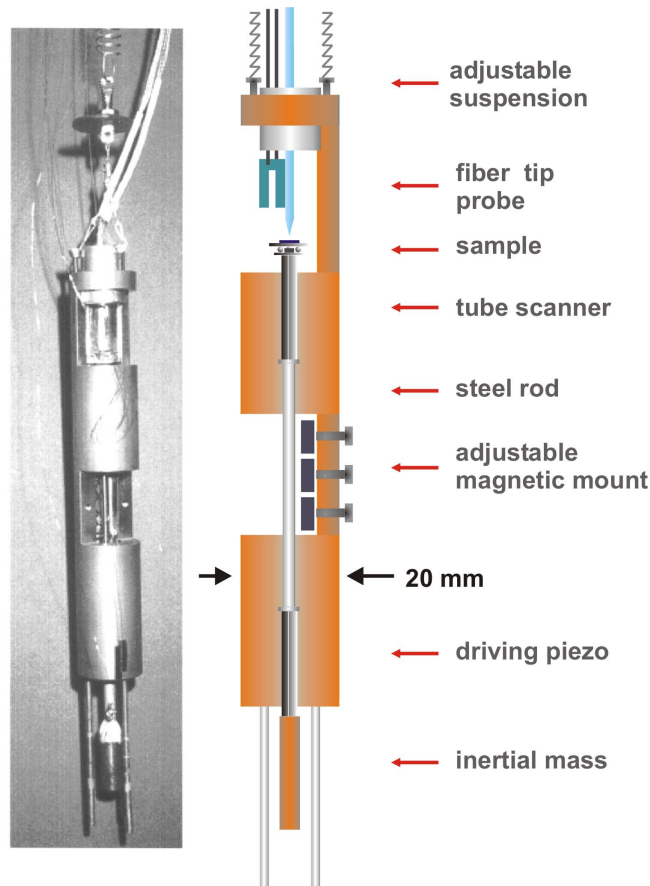


FIGURE 3.2: The hammer-propulsion setup. The walker unit is realized by a magnetically mounted steel rod. The coarse approach is performed using the impact of the inertial mass, which is accelerated by a parabola voltage applied to the driving piezo.

and allowed a number of first experiments at 4 K. However, in particular at low temperatures the inertial propulsion shows a critical sensitivity on a number of interdependent operation parameters and environmental conditions [105]. The temperature and the amplitude of the applied voltage have a particularly strong influence on the efficiency of the hammer drive. Furthermore, the mechanism is extremely sensitive to the frequency and the shape of the applied voltage, as well as to a precisely axial loading, while otherwise the drive would fail working due to a loss of momentum in resonant vibrations [105], or an enhanced canting of the bar. The reduced efficiency of the piezo actuators at low temperatures adds to these problems. A minimization of canting and friction, on the other hand, affected the stability of the walker at a fixed position, and led to an intolerable rate of vertical drift due to gravity. Additionally, the mechanical charge that was induced by the repeated driving jerk led to frequent material failure and breakdown. An attempt to tackle this problem was made by setting up an inchworm

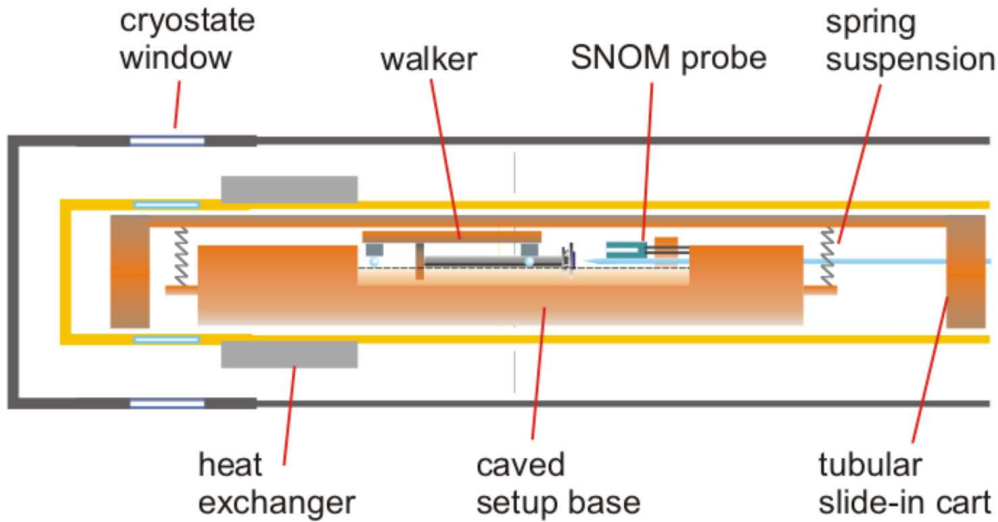


FIGURE 3.3: The horizontal low-temperature setup; diagram of the setup within the horizontal cryostat.

drive in a modified configuration [106]. However, a sufficiently reliable approach at low temperatures was not possible with this setup despite the onward developments.

As an alternative, the concept of the horizontal approach was reviewed in an innovative configuration that was developed on the basis of a former realization for 80 K operation in a dewar [107]. In order to work at lower temperatures, a setup was constructed for operation within the helium flow cryostat which had to be run in a horizontal position for that purpose [108]. Fig. 3.3 shows a schematic of the 'metro' setup. A particular problem in this configuration is, that the measurement chamber provides only minimal space to realize a suspension that provides a sufficient mechanical decoupling from external vibrations. However, at low temperatures the actuation of the lightweight walker turned out to be critical which neither could be solved sufficiently by a varied adjustment of the base within the limited space of the cryostat, nor be bypassed successfully by applying additional loading, or a magnetically tightened mounting.

An effective solution was found using a novel piezo positioner type attocube ANPz 50 for the vertical coarse approach, which is designed particularly for the operation at cryogenic temperatures, or in a UHV [109]. The working principle of this positioner is also based on the controlled use of the inertia of a sliding mass in slip-stick motion. As shown schematically in Fig. 3.4, a propulsion rod is dual-mounted, to a massive table by a springy clamp in such a way that it allows to slide along a fitted guide, and to the driving piezo actuator by fixation bonding. The shape of the guide and the materials used are chosen in such a way

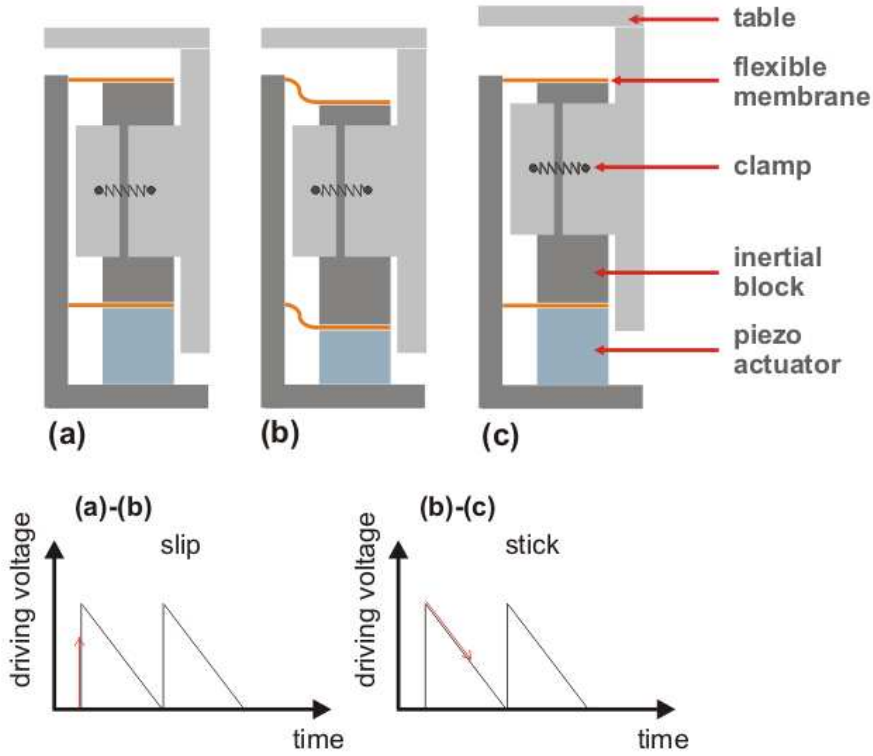


FIGURE 3.4: Diagram showing the working cycle of the inertial driver [109]: (a)-(b) slip motion of driving rod, (b)-(c) movement of clamped table under static friction.

that all surfaces in frictional contact are planar, which results in homogenous and constant friction forces, thus permitting controlled operation even at cryogenic temperatures [109]. To move the table, the actuator is driven by application of a saw-tooth voltage. Within each single step, the rod is accelerated rapidly by the driving piezo, so that the inertia of the table overcomes static friction from the clamp mount, and allows the rod to slide. Then the rod is moved back to its initial position slowly enough so that the inertial table can stick to it, thus being moved a net step (Fig. 3.4). A new setup was constructed adapted to the positioner, which is shown in Fig. 3.5 [110]. The positioner is fixed to the base at the lower end of the chassis, carrying a piezo tube scanner with a length of 30.0 mm, an outer diameter of 3.2 mm, and a wall thickness of 1.0 mm. This has proven to be functional for scanning at a temperature of 4 K, gaining access to a scan range of $20 \mu\text{m} \times 20 \mu\text{m}$. The sample is mounted to a sapphire tripod atop the scanner by means of magnetic holding, while the probe sits above it, being fixed in a displaceable flange, which permits a quick and secure exchange of either of them. Since the permitted range of motion of the piezo positioner is limited to 3 mm [109], an approach-stopper is installed to prevent damaging by excess

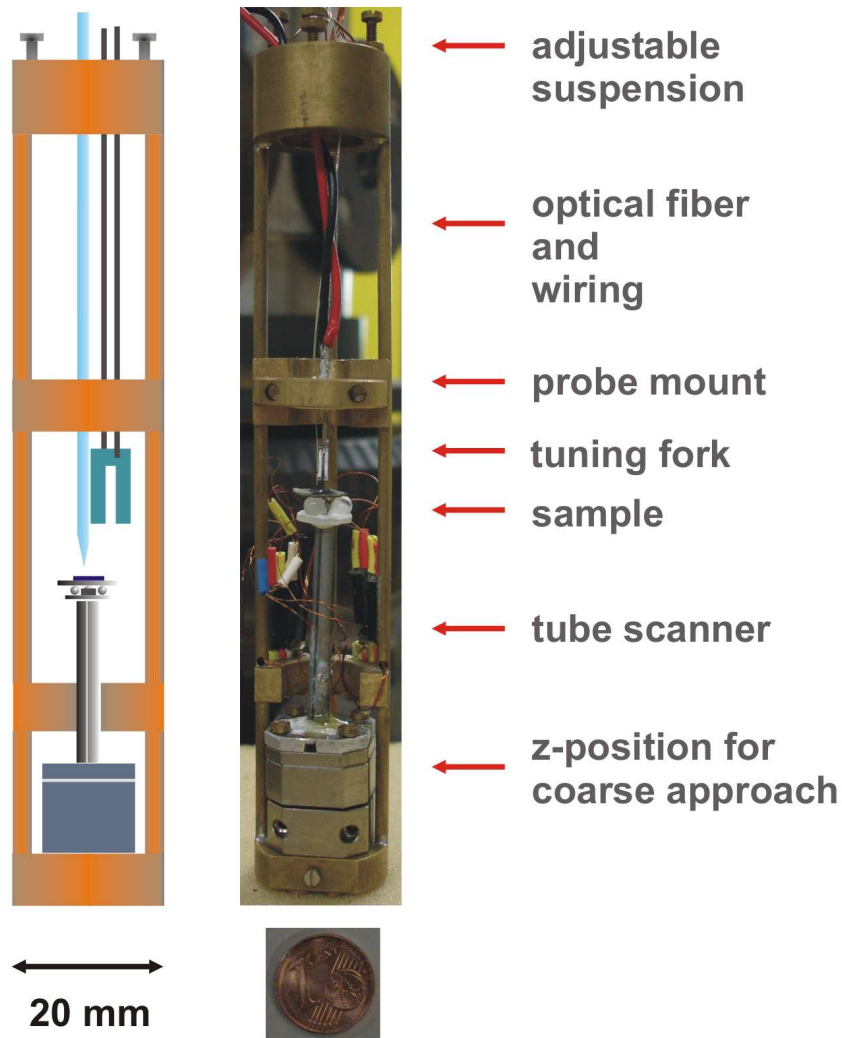


FIGURE 3.5: The new SNOM setup for investigations at low temperatures. The piezo positioner is fixed at the base, carrying the vertical tube scanner. The sample is approached to the probe from below.

motion. In order to avoid an accidental crash at low temperatures due to the contraction of the setup, the coarse approach has to be started from a relatively long distance. The relevant dimension is given by the material contraction taking place between the mount of the positioner and the mount of the tip, minus the contraction of the tube scanner, the positioner, and the tuning fork. Provided that the contraction of the ceramics of the scan tube, the positioner and the tuning fork can be neglected in comparison to that one of the chassis material, a net contraction of about $300 \mu\text{m}$ can be calculated. Taking into account a practically required safety margin, the distance between tip and sample has to be adjusted

to a minimum of about 0.5 mm at room temperature before the setup is cooled down.

The given cryostate permits a visual access to the measurement chamber through the windows located at an internal level of 35 mm, which is exceeded by the dimensions of the positioner plus the length of the piezo scanner. Hence, a direct view onto the sample-tip contact region is not possible, and neither a rough control of the actual distance nor a detection of a failure in the approach mechanism is possible once the setup is in the cryostate. The approach becomes a blind-flight task, and the only reference for a contact of tip and sample is given by the shear-force feedback.

As a possible makeshift solution, two small Si-mirror plates can be arranged in a periscope-like configuration, as shown schematically in Fig. 3.6. One plate is set in a 45° angle directly behind one of the cryostate windows, and the other one is fixed slightly above the probe in a converse 45° angle, being tailored to fit the setup without touching the wall of the cryostate. This way, a direct view onto the tip is possible, provided that the setup is adjusted precisely in the appropriate position. However, since the arrangement frequently failed to work, the measurements presented in this work were performed mostly without visual control.

An effective mechanical decoupling from external vibrations is achieved by an appropriately tuned soft-spring suspension of the setup within the cryostate chamber, which is mounted on an optical table. The chassis of the setup is constructed

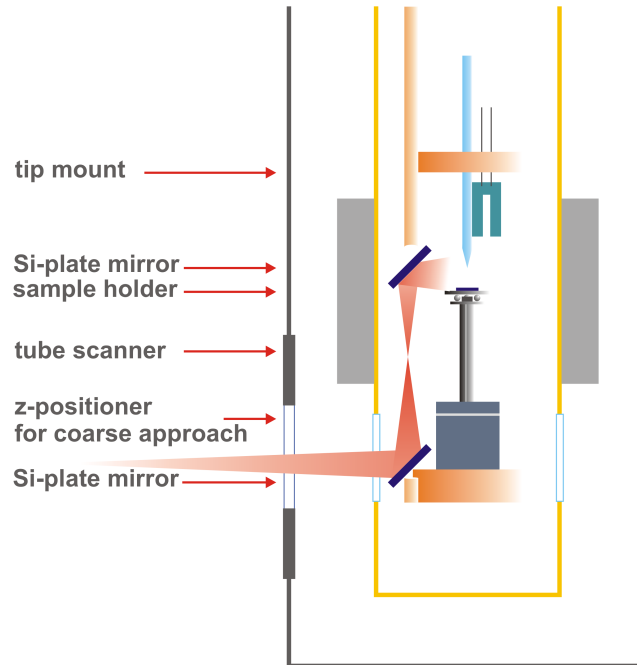


FIGURE 3.6: Visual access to the experiment is possible by of two Si-plate mirrors being arranged in a periscope-like configuration.

especially stiff, consisting of a number of stages, given by the base, the tip mount, the approach delimiter, and the top flange, which are fixed one upon the other by 3 vertically arranged tubular rods which serve for conduction of the electrical wiring also. To avoid mechanical contact with the inner wall of the cryostate chamber, the setup is balanced vertically with an adjustable 3 - point suspension. An extremely ductile wiring and a soft support of the cryostate are further provisions for vibration isolation.

3.2.3 Innovation of the distance control

According to the results of preliminary work, the shear-force feedback technology was chosen for distance control of the low-temperature SNOM. A further benefit of the method is a compact setting, which is easy to prepare and handle, as well as low joule heating, which allows an operation at temperatures of 4 K [31] In the present realisation the fiber tip is mounted alongside one of the prongs of a standard 32.768 kHz tuning fork timer using UHU endfest two-component adhesive, and the loaded fork is driven directly using a frequency generator type Hewlett Packard 33120A, with an intermediary potentiometer permitting a fine tuning of the driving voltage of between 0 – 50 mV peak amplitude. This way, a resonance oscillation could be generated with a typical bandwidth in the order of 60 – 80 kHz at room temperature, and operation of the feedback loop at a set-point of about 70% of the peak resonance amplitude allowed a reliable distance control for scanning.

The stability of the used frequency generator is limited by thermal noise to a critical value of 0.1 mHz [73, 92]. Since at low temperatures the bandwidth Δf of the tuning fork timer decreases rapidly below this value, as was confirmed experimentally, a transfer of the shear-force based distance control to a low-temperature environment requires an artificial reduction of the quality factor.

It is confirmed further by experimental exploration that an additional drain of energy by means of a tuning of the electronic resistance does not affect the quality factor of the tuning fork oscillation [92, 95, 96]. Thus, a mechanical damping of the tuning fork is required, which can be achieved by means of glue application [90]. However, this method was not investigated in quantitative detail up to now, thus generally failing to render predictable results. Therefore, a systematic investigation of the effect of the glue on the tuning fork oscillation was performed, in order to obtain suitable information for a practical application within the frame of this work.

The investigation focused in particular on the standard type 32.768 kHz tuning fork quartz which has been chosen for distance control², exploring especially the effect of the additional load exerted on it by the optical fiber, the amount of

²The second type of tuning fork that would come into question for this purpose is the 77 kHz quartz, which displayed only a marginally varied quality factor in preliminary test runs.

damping induced by the glue and the configuration in which it is applied to the tuning fork, as well as its viscoelastic properties. Furthermore the length of the overlapping end of the tip, as well as the strain exerted on the probe by both the mount and the wiring have to be regarded as having a potential influence on the quality factor. For the mounting, UHU endfest two-component adhesive was figured out to be the only adhesive that works appropriately at temperatures down to 4 K.

In a standard configuration the tuning fork is loaded with 300 μg of glue in a regular composition of 1 : 1 hardener to binder component, as is typically applied to mount a fiber tip alongside the lateral edge of one prong. The length of the overlapping tip could be controlled with a tolerance of 0.05 mm by microscope-aided preparation, which is appropriate regarding the found marginal influence on the oscillation quality. The effect of the mounting of the probe is also negligible in the present setup, according to attendant observations. For reference, the bandwidth Δf of the oscillation was determined in this setting at room temperature for the following: the unloaded fork ($\Delta f_q = 0.010$ kHz), the fork being loaded with glue ($\Delta f_g = 0.013$ kHz), and the typical SNOM probe consisting of a fork and an applied fiber tip ($\Delta f_p = 0.033$ kHz).

First of all, the studies showed that, the application of the tip using glue is the key parameter which leads to a significant variation of the bandwidth Δf . This is in accordance with the suggestion that the quality of the oscillation of the SNOM probe depends on the mechanical dissipation of energy [90–92, 95, 96] However, in practice, the simple application of larger amounts of glue leads to a rapid increase of damping, and suddenly a complete suppression of the oscillation, which impedes a use of the effect for a controlled tuning of the bandwidth. Therefore, a pre-check of the probe at ambient conditions is not possible, because an amount of glue which would yield a sufficient damping effect at low temperatures, suppresses the oscillation at room temperature. Likewise, the studies revealed that the application in a varied configuration, e.g., the additional loading of the fork at the frontal side, or in between the two prongs, either shows no significant effect on the bandwidth, or cuts off the oscillation abruptly. Since the effect of these parameters is extremely difficult to control, and their usage for the tuning of the quality factor is impractical, the focus of the investigations was put on the composition of the glue, which determines its viscoelastic properties [111].

Considering low-temperature experiments, in particular the temperature dependence of the viscosity has to be regarded. Unfortunately there is no quantitative information available on the behavior of the viscoelastic modules of epoxy-based adhesives at very low temperatures. It appears intuitive that, in general the viscosity of the material decreases with decreasing temperatures, and correspondingly the related rate of dissipation. However, experimental observation reveals that a substantial rate of dissipative quality is maintained even at low temperatures, which can be used to tune the quality factor of SNOM probes [90, 107, 110]. Therefore, the respectively induced rate of dissipation was investigated at temper-

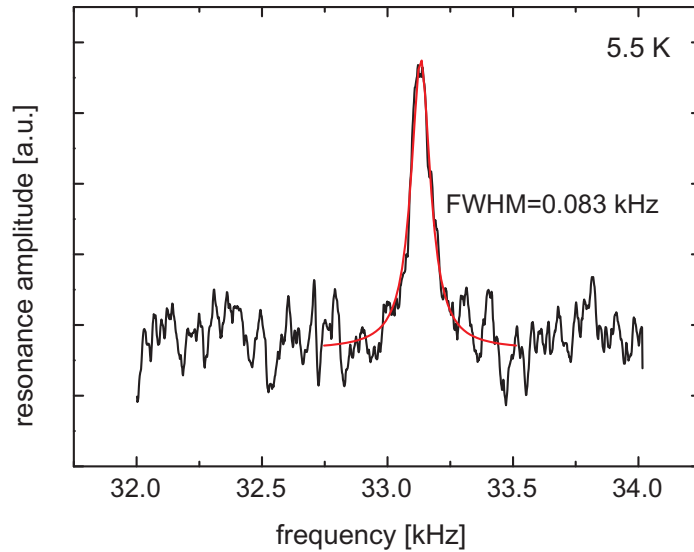


FIGURE 3.7: Resonance of tuning fork probe with glue composition of 2 : 3 hardener to binder, taken at 5.5 K. The bandwidth of the oscillation is 0.083 kHz

atures between 4 K and 300 K, in order to determine an appropriate composition of the glue. In general it was found that a relative increase of the binding component, which can be thought of as a softening of the glue, leads to an increased damping effect. Quantitatively, a ratio of hardener to binder in between 1 : 2 and 1 : 3 was found to result in a reduction of the quality factor which is sufficient for experiments at temperatures down to 4 K. A ratio of about 2 : 3 can be fixed as the optimum composition which results in a typical bandwidth of 70 – 90 Hz at 4 K, while also allowing for a measurable oscillation response at room temperature, thus making possible a pre-check of the functioning of the probe at ambient conditions. Figure 3.7 shows an example resonance curve of a tuning fork probe with 2 : 3 glue composition, taken at 5 K. A bandwidth of 83.24 Hz is determined, which is of the same order as those obtained typically from SNOM probes at room temperature. According to these findings, the low-temperature experiments presented in this work were mostly carried out using a 2 : 3 composition.

3.3 Nearfield probes

Because the samples which were investigated in the frame of this work show relatively low quantum dot densities, a maximum spatial resolution was less im-

portant to observe single objects. Moreover, the capping material on top of the quantum dots already limited the resolution due to spatial dispersion within the cap layer [38]. The maximum spatial resolution that could be obtained in the given setting was determined to be of the order of the capping thickness, i.e. some 100 nm. On the other hand, a good transmission efficiency of the fiber tip was of major importance for investigations in the low-population regime of quantum dots. Because of this for the investigations presented in this work primarily etched fiber tips were used.

In general, the chemical etching method yields large cone angles of up to 40° , which results in high transmission coefficients of 10^{-3} or even more [31, 44]. An additional benefit of the technique is that it permits the production of larger quantities of probes in a single step with reproducible quality.

For the preparation of fiber tips by chemical etching in a standard configuration the acrylate jacket is removed from the end of a multi-mode index gradient optical fiber, and the stripped fiber is dipped into aqueous 48% hydrofluoric acid (HF) solution, which is covered by a thin lipophilic overlayer such as, e.g., hexadecane or isooctane³[112]. Due to the adhesive forces between the different materials a fluid meniscus forms at the interface between the glass fiber and the etching solution, as is shown schematically in Fig. 3.8. Whilst the diameter of the fiber

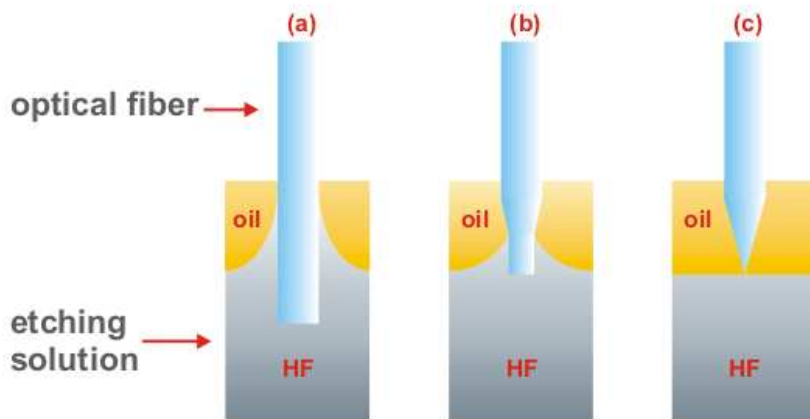


FIGURE 3.8: Etching of optical fiber tips. The successive narrowing of the fluid meniscus at the material interface leads to the formation of a taper from the optical fiber.

narrows with the progression of the etching process, the height of the meniscus decreases, which leads to the formation of a cone, and a sharp tip with an apex diameter of a few tens of nanometers. This process takes about one hour typically, and stops when the tip is finished and the surface of the etching solution is closed underneath the apex. After that the fiber is removed quickly and rinsed with distilled water and pure ethanol, in order to remove any remaining HF

³We also obtained very good results using *Penaten* baby oil.

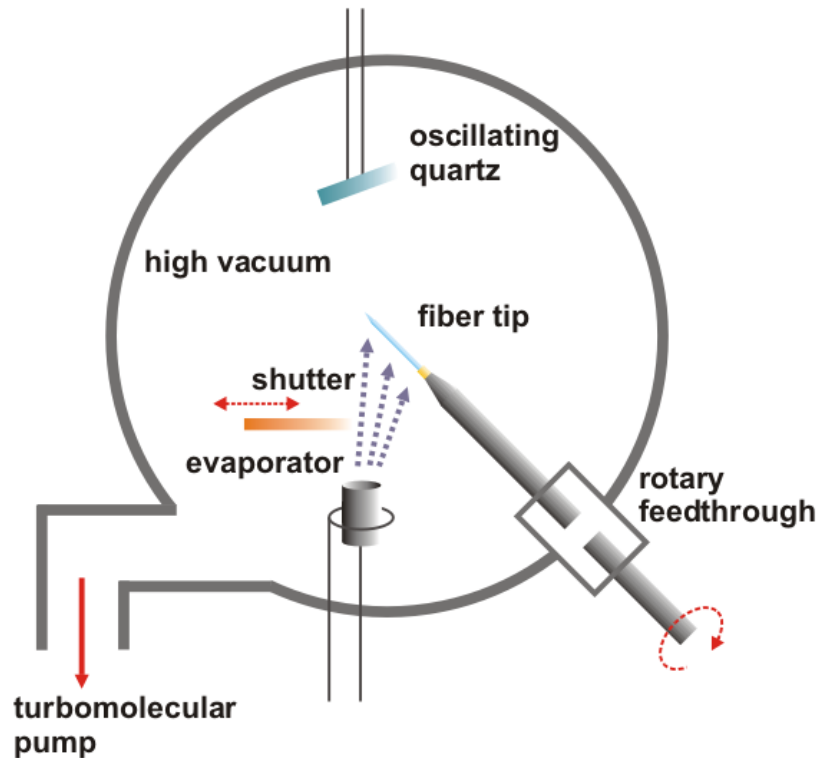


FIGURE 3.9: Coating of the optical fiber tips by means of electron beam evaporation in a high vacuum. A regular covering of the tapered end of the fiber is obtained by a slow rotation of the fiber.

which otherwise causes damage to the cone by continuing erosion. The quality of the surface and the symmetry of the obtained probes depend sensitively on the etching parameters, such as a careful cleaning of the fiber, the purity of the HF solution and the lipophilic overlayer, as well as on environmental influences such as vibration, temperature stability, convection flow within the etchant, and so on.

Part of the measurements presented in this work were performed using fiber tips that were coated with a thin Ag layer, in order to get an optimum spatial resolution. The material was chosen for reasons of its small skin depth of about 12 nm, and its relatively convenient handling [45]. The coating of a tip is performed by electron beam evaporation in a high vacuum. Therefore, the fiber tip is placed in the vacuum chamber at an angle of 45° above the evaporator, as shown in Fig. 3.9, in order to obtain a smooth metallic film with a minimal covering of the tip apex. During the evaporation of the coating material the tip is rotated slowly along its axis, which leads to a regular covering of the tapered end and the formation of a circular aperture. An online observation of the material deposition is possible using an oscillating quartz that is placed slightly above the rotating

probe. During the evaporation the successive loading of the quartz with Ag leads to a measurable shift of its resonance frequency. This allows a determination of the deposition rate and the actual thickness of the coating layer. The quality of the obtained aperture depends on a number of parameters: the angle of inclination of the fiber tip, the quality of the surface of the cone, the rotation frequency, the speed of deposition, and the final thickness of the coating layer [44].

In some cases the tip apex is covered slightly when particularly thick coatings are applied, and must be freed by a inducing controlled frictional contact against the sample surface using an appropriately adjusted distance control [45]. Sometimes also a repeated scanning of a sample area results in the successive opening of the tip, because of the tendency of coated tips to degrade relatively fast during usage [44]. The tips that were used in the frame of this work have been coated with relatively thick layers of 50 – 200 nm Ag, in order to ensure a leakproof covering.

3.4 The photoluminescence spectroscopy setup

For photoluminescence spectroscopy of semiconductor nanostructures a setup was prepared according to the diagram shown in Fig. 3.10 [45].

For the excitation of the samples an Ar^+ -Ion laser is used, which is emitting at 488 nm in continuous wave mode, with a tunable emission power of 4 – 40 mW. A fine-tuning of the excitation intensity, especially at very low emission power, is possible using a set of grey shade filters. An additional edge filter is used to block thermal radiation from the laser, which otherwise would interfere with the analysis of the photoluminescence signals obtained from the quantum dots. The light is coupled into a standard multimode optical fiber with a core of 50 μm and a gradient-index cladding of 125 μm diameter, which guides it towards the SNOM probe, reversely passing a $2 \times 1 - 80/20$ fiber coupler, as is illustrated in Fig. 3.10. The luminescence signal from the sample is collected by the probe in internal reflection configuration, and is then split 80% to 20% in intensity by forward-passing the fiber coupler. While the lesser part is lost way back to the excitation source, the major part is guided to the spectrometer setup which consists of monochromator and detector. For the spectral analysis of the signal a monochromator type Jobin Ivon HR 320 is used, which is characterized by a focal length of 32 cm and a blazed grating with 600 streaks per mm, attuned to a blaze wavelength of 1500 nm. While in operation, the monochromator is flushed with nitrogen in order to prevent adsorbates of water on the optical components, whose specific absorption in the near-infrared would cause interference with the observed luminescence spectra.

A calibration of the monochromator was performed by taking emission spectra of an InGaAsP-photodiode, showing that the spectral resolution can be tuned up to a maximum of about 0.2 meV at a slit width of 0.1 mm. Depending on the sensitivity of the detector, a compromise between signal intensity and spectral

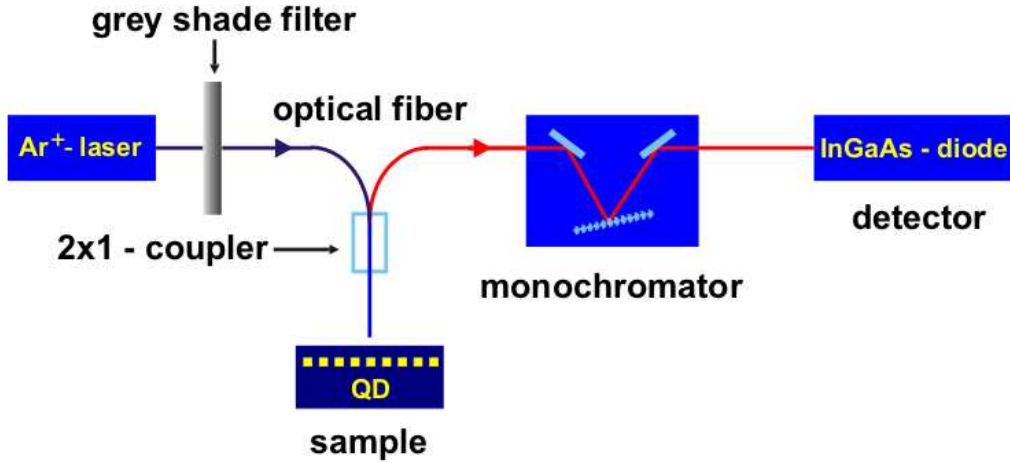


FIGURE 3.10: Diagram of the PL spectroscopy setup. The luminescence signal from the sample is detected in internal reflection geometry, and is analyzed using a monochromator and an InGaAs-detector. The excitation intensity is tuned using grey-shade filters.

resolution is often necessary. Experience shows that, especially in investigations of single semiconductor quantum dots the monochromator has to be operated with relatively wide open slits of 0.5 – 1 mm to obtain sufficient signal intensity, which results in a spectral resolution of about 1 – 2 meV. In this case the spectral resolution depends not only on the slit opening but also on the diameter of the spot that is focused onto it. Concerning the analysis of the spectra, it further has to be regarded that, when the spectral width of the luminescence lines is of the same order as the resolution of the monochromator, the obtained lineshape is given by a convolution of the physical lineshape with the effective throughput profile of the monochromator. For the investigation of semiconductor quantum dots at low temperatures the observed peak is a Voigt-profile, i.e. a convolution of a Lorentz-function with a Gaussian and the effective resolution can be determined as the FWHM of this function [100]. For the detection of the photoluminescence signal, a Peltier-cooled InGaAs-photodiode is used, which is coupled directly to the optical fiber. The detector has a maximal sensitivity of $5 \cdot 10^{-17}$ W with a noise-equivalent power of $0.1 \text{ fW}/\sqrt{\text{Hz}}$, which in principle allows the detection of an intensity of 1000 photons per second. The effective detection range is between 800 nm and 1700 nm wavelength. The detector can be operated at a selectable integration time constant of 0.23 Hz, 2.3 Hz or 23 Hz, which influences the measuring speed, but also the signal to noise ratio (SNR), meaning that a faster detection is possible at a larger bandwidth, but the level of background noise is also increased. Since a maximally sensitive measurement requires integration times of about $1/0.23 \text{ Hz} \approx 4 \text{ s}$ per point, in practice concessions have to be made normally, very often in terms of sensitivity. At low

temperatures especially, where the reduced stability of the tip position requires fast measuring, the detector is operated mostly at a time constant of at least 2.3 Hz. In order to get sufficient spectral resolution, a spectrum should be taken with about 5 – 10 points per nanometer wavelength. Thus, the average time required to take a single spectrum with a meaningful spectral resolution and a sufficient SNR is approximately 1 min.

For a thorough analysis of the spectral data, the impact of cosmic particles on the detector has to be regarded, which leads to additional peaks in stochastic time intervals. Figure 3.11 shows an example dark-spectrum from the detector with a number of features which originate from such incidences. The irregular appearance of these particle features can be taken as a first indicator to differentiate them from the relevant luminescence signal. Accordingly, the questionable lines can be tested easily for reproducibility by repeated measurements. However, low temperatures often require a fast experimentation, so that the replication of a measurement under precisely the same conditions is not always possible. Therefore, the characteristic lineshape can be taken as a second criterion to discriminate artifacts from cosmic particles in the spectra. The example spectrum shown in Figure 3.11 gives a reference for their typical appearance, thus allowing the determination of a characteristic fingerprint, as is illustrated in the Figure. A

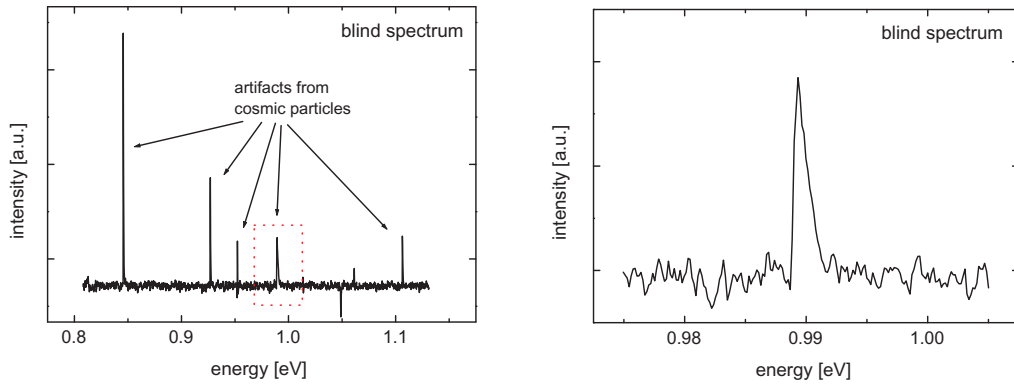
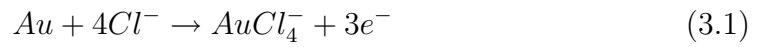


FIGURE 3.11: Reference spectrum of the detector; peak artifacts originate from the impact of cosmic particles; the characteristic line profile becomes visible in the extension.

major characteristic is the asymmetrical lineshape, which reflects an immediate charging of the detector by the impact, and the following teardown which takes longer time while continuing data acquisition. By contrast, an actual luminescence signal is characterized by a basically symmetrical lineshape.

3.5 Apertureless nearfield microscopy

For the exploration of the apertureless nearfield detection it is necessary to fabricate Au tips with an apex diameter in the order of a few nanometers. These are produced by electrochemical etching in 37% hydrochloric acid (HCl), according to the method described in [113]. Therefore the end of a thin Au wire is dipped into the etching solution, and a voltage is applied by means of a second Au wire which is put on negative potential. This second wire is formed into a circle thus creating a symmetrical counter electrode, as is shown schematically in Fig. 3.12 (a). Because of the applied voltage metal ions are dissolved from the anode wire in the center by chemical reaction with chloride ions according to



or



and diffuse to the cathode. Since the material ablation is enhanced at the interface between the solution, the metal and the surrounding air, the wire is thinned out in this region until the tail is ripped off eventually by the weight of the dangling end piece. By this process a sharp taper is formed from the anode wire, which can be used as a nearfield probe tip. Typically, the etching voltage is of the order of 1 – 3 V, depending on the concentration of the etching solution, the size of the anode wire, and the diameter of the cathode circle. The associated flow of

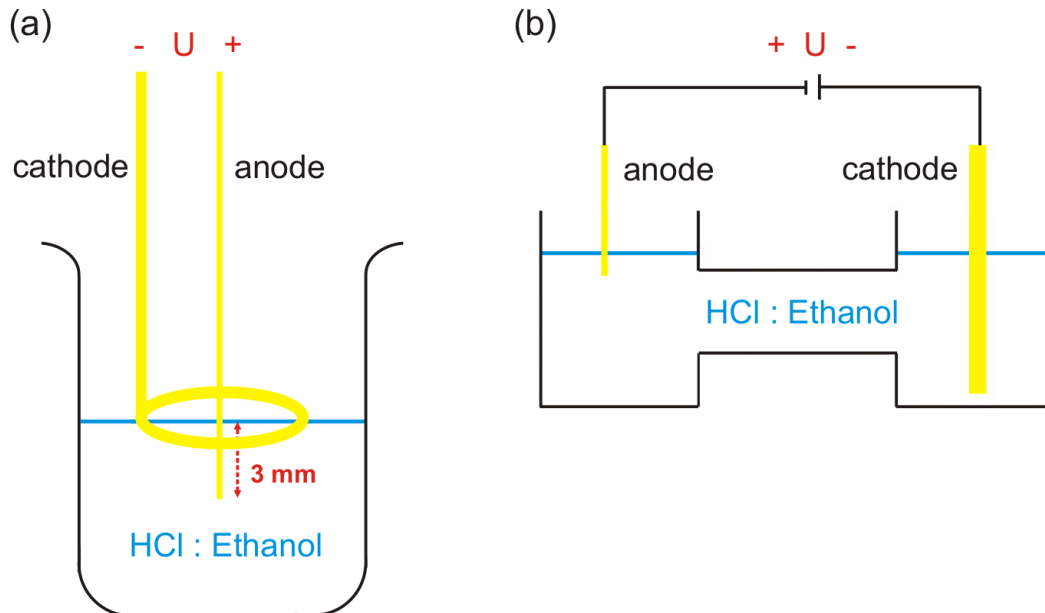


FIGURE 3.12: Electrochemical etching of Au tips: (a) in the standard configuration; (b) the u-pipe configuration allows a better suppression of turbulence within the etching solution.

charges results in a current which can be measured between the electrodes, being proportional to the etching speed [113]. After the rupture of the tail the resistance within the circuit rises abruptly, leading to an immediate decrease of the measured current. To obtain an optimal tip quality an instantaneous turn-off of the voltage is important to prevent a degradation of the tip by remnant chloride. This is accomplished using an especially constructed electronics which allows an online monitoring of the etching current, and an automated voltage cut-off within a few milliseconds [92].

The chemical reactions associated with the formation of the tip consume large amounts of Cl, thus leading to a periodic decline in the concentration of Cl^- -ions around the anode wire, which are substituted cyclically by diffusion. This can be observed as an oscillation in the current. The reaction can be stabilized by application of a relatively high voltage of more than an empirically determined value of 1.4 V, in the present case. However, this brings about an increase of turbulence by the formation of Cl_2 and O_2 bubbles in the solution, hence leading to a roughening of the obtained cone surface. It was found that such turbulence can be suppressed by the addition of ethanol to the etchant [113].

Since the formation of bubbles is enhanced at the cathode, a further suppression of turbulence can be achieved using a specifically designed u-pipe reaction tube, as it is shown schematically in Fig. 3.12 (b), which ensures a better spatial separation of the electrodes and a more quiet flow of chemicals [114]. This configuration allows a reproducible production of tips with a small apex of the order of 50 nm. Figure 3.13 (a) shows an example rasterelectron microscopy (REM) image of a Au tip that was etched with the standard ring electrode configuration and a voltage of 1.4 V. As visible, the surface of the tip shows a distinct roughness along the length of the whole cone to the apex of the tip, which can be assigned to the occurrence of turbulence during the etching process. For comparison, Fig. 3.13 (b) shows a tip that was etched in the u-pipe setup at 2.4 V, showing a significantly reduced surface roughness.

An extended exploration revealed that a further improvement in terms of surface smoothness and cone geometry is possible by adding minute amounts of lipid substances to the etching solution. For instance, Fig. 3.13 (c) shows a tip that

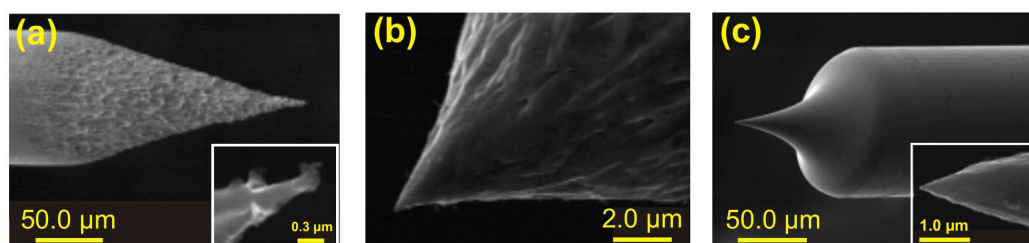


FIGURE 3.13: REM images of Au tips; (a) Au tip showing roughened surface due to turbulences in the etching solution; (b) Au tip etched in u-pipe shows less surface roughness; (c) Au tip etched in lipid-stained solution shows smooth cone surface.

was etched in the u-pipe at a voltage of 1.8 V in a solution of 1 : 1 ethanol (100%) to HCl (37%), and stained with about 0.01 vol% grease. The tip shows a smooth surface along the full length of the cone, and an apex of about 70 nm in diameter. A specific feature of this tip is the hyperbolic cone profile, which resembles that of high-quality tungsten tips as there are fabricated by a similar process for scanning tunneling microscopy [115]. By contrast, the cones of conventionally produced Au tips normally show a more linear profile. A benefit of a hyperbolic profile is the reduced tip angle, which results in a stronger confinement of electrons at the apex, and thus to a broadening and a redshift of the plasmon resonance⁴ [61]. In order to explore the apertureless probing of the optical nearfield using a metal tip, an extra setup was constructed specifically for experiments in the attenuated total reflectance configuration, as is shown in top view by Fig. 3.14. This setting allows a selective probing of the optical nearfield from a translucent sample [50]. In the present realization, a right-angled glass prism represents the sample which is mounted to a piezo tube scanner, being approached horizontally by a conventional sleigh-like walker to the opposing tuning fork probe. A lens optics is adjusted to focus the light of a HeNe laser ($\lambda = 632.8$ nm) onto the base of the prism from behind, thus allowing an excitation of the sample by means of the evanescent field that is present there under illumination in total reflectance⁵ [50]. The signal from the nearfield probe is collected in the far-field using an optical fiber with a large core of 1 mm diameter, and guided to a Si-avalanche photodiode (APD) single-photon detector. The angles of excitation and detection can be adjusted continuously over 90° relative to the prism by two circular track slots in the base of the setup.

For the implementation of a shear-force feedback for apertureless SNOM, the way in that Au tips differ physically from optical fiber tips must be regarded [37]. A systematic investigation of the relevant control parameters showed that in general, Au tips should be rather thin and of as little weight as possible. This is plausible regarding their physical parameters, as the specific mass and the viscoelastic properties, which have a significant influence on the quality factor of a tip-tuning fork probe system [116]. The application of a piece of an Au wire to a tuning fork adds an excentric load to the system which may result in a considerable perturbation of its oscillation. Additionally, the ductile wire material leads to an enhanced dissipation of energy which is inappropriate at least at room temperatures. The preference is, therefore, for tips made of Au wires with a small diameter of the order of 0.1 mm, which are cut back to a length of 1 – 1.5 mm and mounted to the head of the tuning fork, as is shown in Fig. 3.15 (a). A typical resonance curve of such a probe is shown in Fig. 3.15 (b), having a bandwidth of $\Delta\omega_{Au} = 6.47$ Hz [114]. In general, a shear-force distance control with

⁴An elongated shape also leads to an enhanced polarization of the electromagnetic response function of such tips.

⁵The depth of the evanescent field under total reflectance is approximately 200 nm in air for a surface of glass type BK-7.

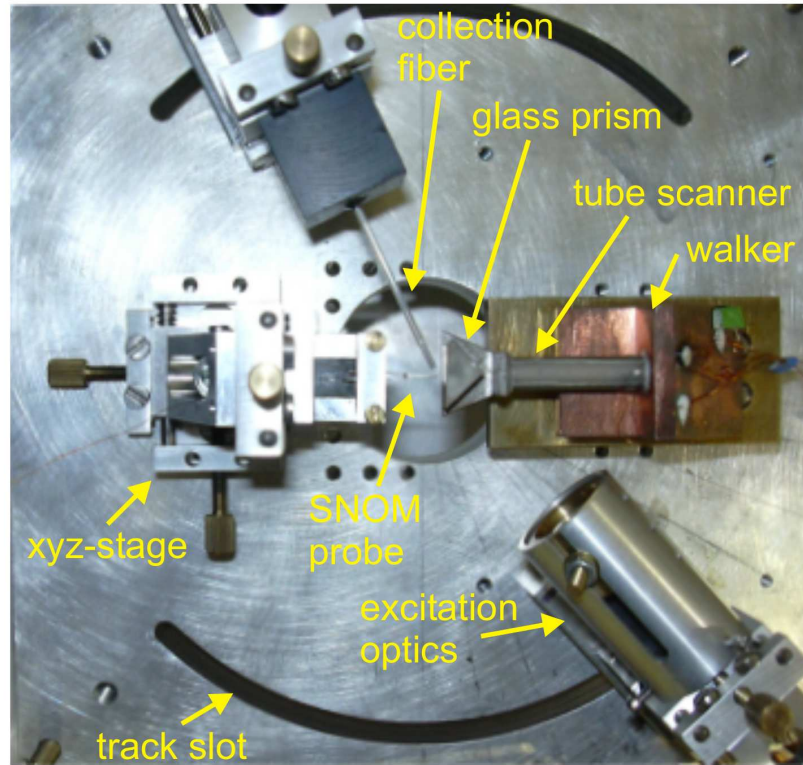


FIGURE 3.14: Top view of the the dark-field setup. The sample is mounted to the base of the glass prism. The probe can be adjusted to the collection optics in 3 directions in space. The angles of excitation and signal detection can be independently adjusted.

Au tips is more sensitive than using an optical fiber tip, while on the other hand the more ductile material results in less stability, thus demanding a lower excitation, higher time constants for lock-in integration and a better decoupling from external vibrations. Since the luminescent signal is detected in the far-field, an extra filtering is necessary in general to discriminate the light from the nearfield probe against the background signal of the surrounding sample area. This can be performed with a periodic variation of the distance between the probe and the sample using lock-in technology, taking benefit from the strong dependence of the evanescent field on the distance. For this purpose, a modulator device was constructed in the context of this work, which allows an independent modulation of the distance of the order of several 100 nm while scanning a surface. Pictorially speaking, the tip is dipped into the nearfield with a certain frequency which is taken in parallel as a reference for the lock-in filtering of the obtained optical signal. The effect is shown in Fig. 3.16 (a), (b), once with an optical fiber tip and direct nearfield detection (a), and once with a Au tip and far-field detection (b). The images show the oscillating control voltage applied to the piezo tube scanner in parallel with the intensity of the detected signal [114]. The modulation was

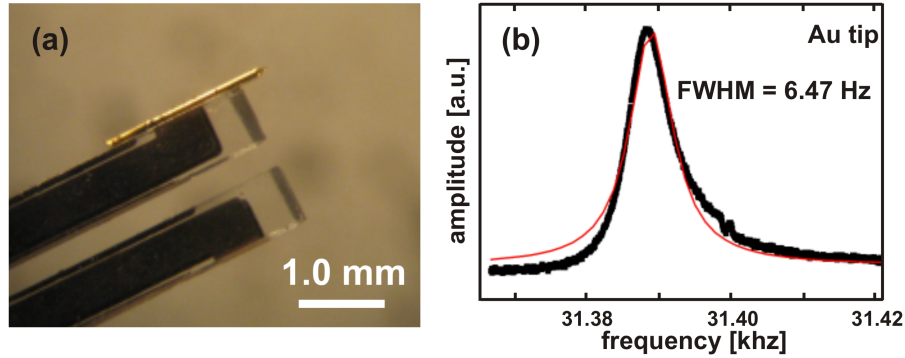


FIGURE 3.15: (a) an Au tip applied to a tuning fork; (b) resonance curve of the Au tip, showing a characteristic bandwidth of 6.47 Hz at room temperatures.

done at a frequency of 39 Hz, which is slow in comparison to the time constant of the APD of 10 ms. A clear correspondence of the intensity of the optical signal to the modulation pattern is observed. However, in the case of the Au probe the signal suffers from considerable noise, because a very low intensity of the order of ≈ 1000 photons per second was received. At this low intensity, already very small stochastic variations lead to a significant perturbation of the signal. In order to work out the potential of the technique for a prospective investigation of nanostructured samples, a test structure was prepared onto the glass prism, consisting of a thin Au film which contains statistically distributed apertures of two different, sub-wavelength sizes. For this purpose, synthetic spheres of 100 nm and 200 nm diameter are applied in aqueous suspension onto the base of the prism which is then coated, after drying in air, with a film of 70 nm Au by evaporation in UHV. With a subsequent treatment in an ultrasound bath the covered spheres are thrown off, leaving nanosized holes within the metal film. The density of these apertures can be tuned via the concentration of the spheres

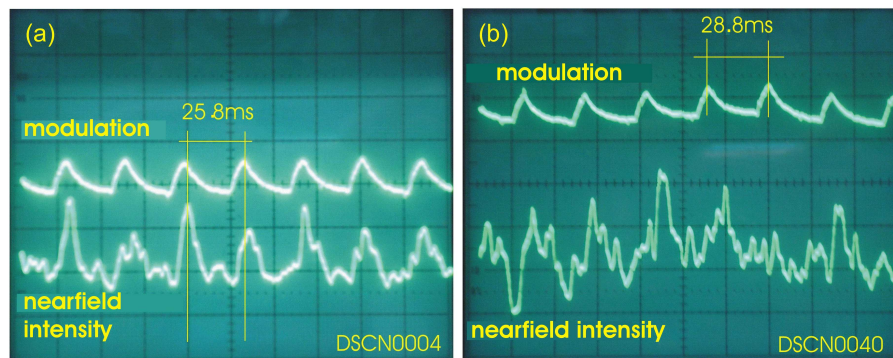


FIGURE 3.16: Modulation filtering of the luminescence signal; (a) probing of the nearfield with optical fiber tip, (b) scattering of the nearfield with Au tip.

in the suspension. Figure 3.17 shows an REM image of the prism surface, in which holes of different sizes can be identified, as well as a number of equally sized bumps indicating spheres that remained adhering to the prism surface and where covered by Au. In some cases also larger structures as, e.g., paired holes appear, where spheres have been stuck together during the preparation process. According to the REM measurements, the average density of topographic features is 10^8 cm^{-2} , which corresponds to a probability of $0.5 \mu\text{m}^{-2}$ of features being expectable to be observed in scanning probe images.

Figure 3.18 shows an example pair of scanning images of the test sample, taken at first with an uncoated optical fiber tip and without distance modulation. Correlations between the topography image and the detected luminescence signal are obvious, particularly in the form of manifold small jumps which are recognized as bright spots with a characteristically asymmetric shape in the topography (Fig. 3.18 (a)), while in the luminescence image Fig. 3.18 (b) the corresponding spots are found showing up as dark. This indicates a decrease in the detected intensity, which is due to an increased distance between the tip and the sample. The jumps originate from sudden tip contacts, which can be due to surface features, or be induced by external vibrations. The asymmetric shape is the result of the large recovery time of the distance control, which leads to a slow re-approach after a fast retraction in response to the contact. In addition to these jumps, some further structures can also be observed as corresponding in the images, whose assignment to the morphological structures of the test sample is more delicate. In detail three prominent areas are indicated in Fig. 3.18 (a), (b), which show a distinct variation in the measured intensity in particular in the luminescence image (Fig. 3.18 (b)), having a maximum lateral diameter of $1.92 \mu\text{m}$ (1), $0.89 \mu\text{m}$ (2), and $0.65 \mu\text{m}$ (3), respectively. These spots may actually represent aperture holes, regarding the enhanced luminescence intensity, with the spot (1) showing a

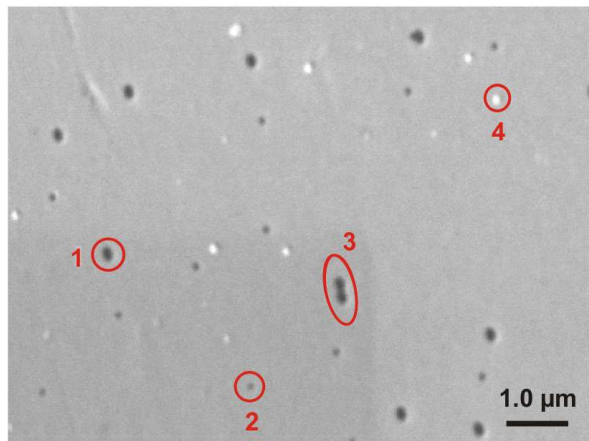


FIGURE 3.17: REM image of test structure. Circles indicate characteristic features: (1), (2) single holes, (3) paired holes, (4) bumps [100].

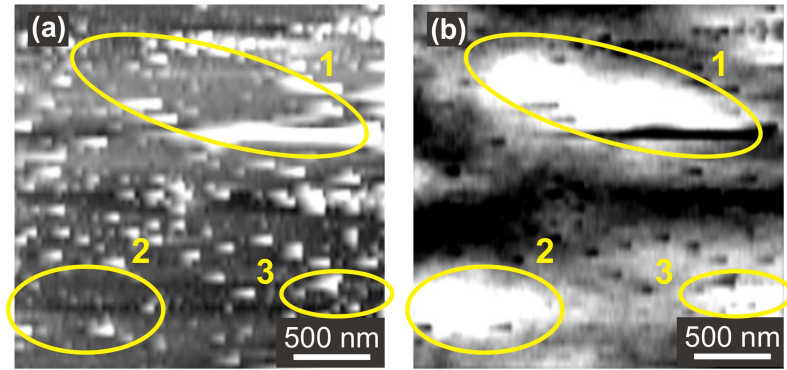


FIGURE 3.18: Scanning image of test structure, taken with an optical fiber tip; (a) topography, (b) luminescence image; the features (1), (2) and (3) are interpreted as originating from aperture holes within the sample surface.

doubled aperture, according to its elongated profile. However, the dimensions of these spots at first view call such an assignment into question, as well as the lack of corresponding depressions in the topography image. As a reference for the discussion, the characteristic appearance of the topographical features of the sample in scanning images can be taken, which is shown in Fig. 3.19: while the spheres which are still covered by the Au film are imaged in the form of bumps (Fig. 3.19 (b)), a hole, by contrast, does not appear as a topographical depression, but rather shows up typically in the form of a rough-textured area, as is shown in Fig. 3.19 (a). The reason for this is that the shear-force feedback responds to the edge of the hole even if the diameter of the used tip is too large to allow a distinct imaging of the aperture. Regarding the size of the spots in the luminescence image, it has to be further taken into account that the measurements which are shown in Fig. 3.18 were performed using an uncoated fiber tip, thus falling victim to a sideward penetration of light into the cone of the tip, which results in a decrease in optical resolution. According to these considerations, the observed spots may be well assigned to apertures. For comparison, Fig. 3.20 shows a couple of scanning images that were taken with an Au tip and distance modulation. Since the luminescence enhancement of the used tip was weak, the measurement was performed at very low light intensity in order to observe the filtering effect of the modulation.

A similarly fissured area with a maximum diameter of 290 nm is visible (Fig. 3.20 (b)), corresponding to a bright spot of 360 nm diameter in the luminescence image (Fig. 3.20 (a)). Remarkably, the luminescence spot which is detected with the Au tip is much smaller than, e.g., the spot (2) detected with the fiber tip (Fig. 3.18), even though in neither case the hole is imaged as a well-defined depression in the topography. Assuming that in both cases a single aperture was investigated, the improvement in the optical resolution can be assigned to the

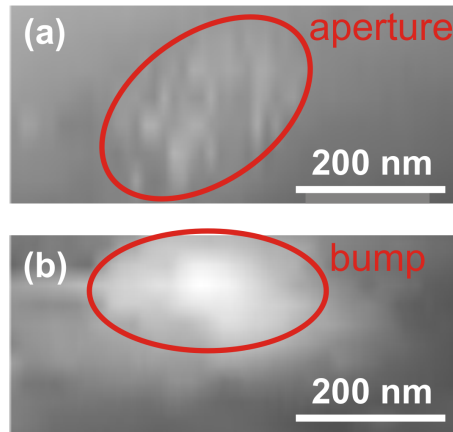


FIGURE 3.19: Characteristic appearance of surface structures in topographical scanning images: (a) apertures and depressions show up in the form of rough-textured areas, revealing an unsteady scanning contact, (b) bumps are imaged with a smooth profile.

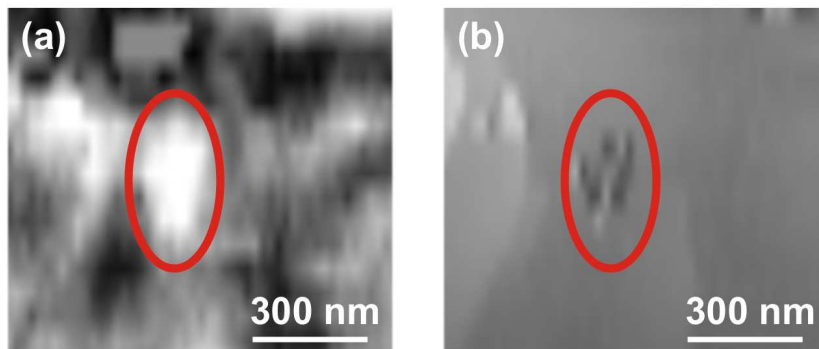


FIGURE 3.20: Scanning images taken with an Au tip and distance modulation, showing a bright spot in the luminescence image (a) and the corresponding topographical image of the hole as a rough-textured blot (b).

distance modulation used for the measurement with the Au tip.

However, because the effective electromagnetic interaction between the tip and the sample is actually much more complex than it is outlined in chapter (2.2.3.) a number of additional effects occur in measurements in particular on structured metallic surfaces [117]. Thus, the improved spatial filtering is paid for by an increased observation of artifacts, which can superimpose on the expected signal pattern. When a metallic surface is structured on a scale of nanometers particularly the appearance of radiative plasmons can be induced. As visible in Fig.3.20 (a), there are bright spots showing up in the luminescence image which cannot be assigned to a recognizable aperture hole. Instead, these spots correspond to nano-sized surface defects or step-edges which are particularly prone to the excitation of radiative plasmons. The effect is demonstrated in Fig. 3.21, showing a fissure

which might be due to a damage in the surface structure, or the edge of a material terrace. Also the preparation process of the sample leads to nanosized tears or fringes from the ductile material at the edges of the holes when the spheres are thrown off in the ultrasound bath. These fissures are not only prone to the excitation of plasmons, but also tend to interact mechanically with the nearfield probe, thus leading to a perturbation of both the topographical and the optical signal. These features are seemingly imaged with a very high resolution of better than 50 nm (Fig. 3.21). It can be conceived that, while on the one hand the plasmonic effects interfere with a speckless imaging of topographical structures, on the other hand they offer an intriguing possibility to investigate the electro-optical properties of metallic nanostructures. However, an explicit analysis of the obtained images is difficult, and extended investigations are first necessary in order to get a more detailed understanding of the effects which are involved in apertureless nearfield imaging, before the application of the technology to the investigation of semiconductor nanostructures can be considered.

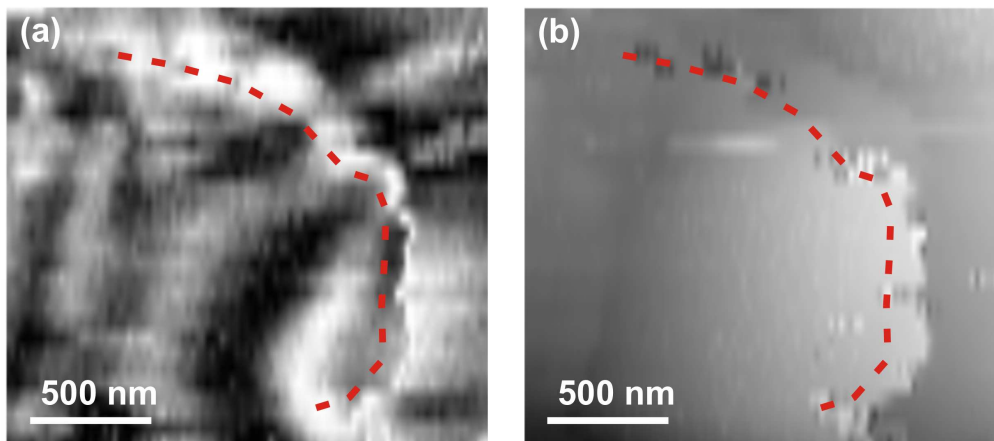


FIGURE 3.21: Scanning images taken with an Au tip and distance modulation, showing a luminescence signal from a surface fissure (a), and corresponding topography (b).

3.6 Characterization of the low-temperature SNOM

3.6.1 Calibration of the scanner

To determine the size, shape and relative location of the features to be observed, the scanning images have to be calibrated in terms of both, size and topography, as well as optical resolution. The size of a scanning image depends essentially on the geometry of the scanner and the efficiency of the piezoelectric conversion. Particular attention has to be paid to the fact that the voltage-induced relative deformation of the scanner is temperature-dependent. If the specific temperature dependence of the material is known, the relative deformation of the scanner can be calculated from its geometry. To obtain a reference for the calculation, a number of calibration measurements were performed on an uncovered CD surface, which provides a defined topographical structure, given by the standardized distance between the traces of $1.7 \mu\text{m}$. To detect a potential inequality of the scanning directions, such as it can originate from material irregularities of the tube scanner, the images have to be taken twice with interchanged polarity of the applied voltages.

From such measurements, the relative lateral displacement per voltage of a point on the sample surface was determined for the new setup to be 200 nmV^{-1} at room temperature. With the dimensions of the tip, the sample mount and the used tube scanner, and the specific properties of the piezo material, the respective values can be determined for different temperatures, which allows the calibration of scanning images as necessary. In this way, for a temperature of 80 K a lateral displacement of 40 nmV^{-1} was determined, according to the example scan image shown in Fig. 3.22. For a temperature of 4 K a value of 20 nmV^{-1} results.

3.6.2 Obtained topographical resolution

The spatial resolution which is obtainable by a scanning probe microscope is limited by the minimum step-size that the probe can be moved, which in turn is determined by the smallest voltage difference that can be applied to it, as well as the noise voltage of the used HV-amplifier [92]. This means that the properties of the control electronics set a basic limitation to the resolution. However, in most cases the geometrical properties of the probe, and the specific kind of physical interaction which is monitored, are more relevant in defining the actual resolution limit. For a SNOM, the primary factor is the geometry of the nearfield probe, whose apex radius is typically of the order of a few tens of nanometers (nm). By comparison, the amplitude of the tuning fork oscillation is of the order of several picometers pm, up to a few nm, depending on the quality factor of the probe, and on the amplitude of the driving voltage, and can thus be neglected [37]. A calibration for the topographical resolution can also be obtained from

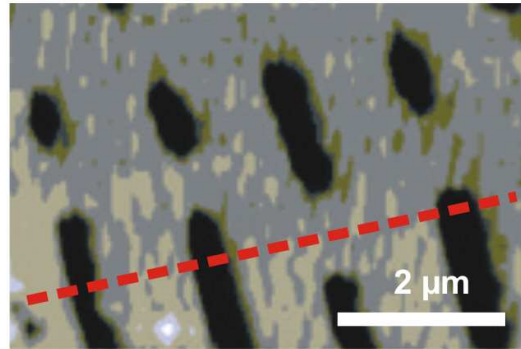


FIGURE 3.22: Scanning image of cd surface, taken at 80 K. The dimensions of the image are determined according to the standardized distance of the traces of $1.7 \mu\text{m}$. The variation of the height along perpendicular to the traces is taken as a measure for the topographical resolution.

the scanning of the uncovered CD surface. For this purpose, the variation of the imaged height is determined perpendicular to the traces, as it is indicated in Fig. 3.22. The mean full width half maximum (FWHM) of the edges of the pits can be taken as a measure for the topographical resolution which is obtained in the measurement. In this way, for the example scan image shown in Fig. 3.22 a topographical resolution of 20 nm was determined. However, since the actual value depends largely on the geometry of the tip, the topographical resolution varies correspondingly in the range of several tens of nanometers. Thus, the calibration merely provides a rough measure.

If the correlations between the spatial structure and other physical parameters of a sample are of particular interest, accurate topographical imaging becomes very important. This is the case, e.g., in the characterization of so-called microcrystalline CuInS_2 (CIS) - solar cells, which have been investigated in the context of this work with respect to their local efficiency in photovoltaic conversion. Figures 3.23 (a) - (c) show the irregular surface topography of these devices, which are

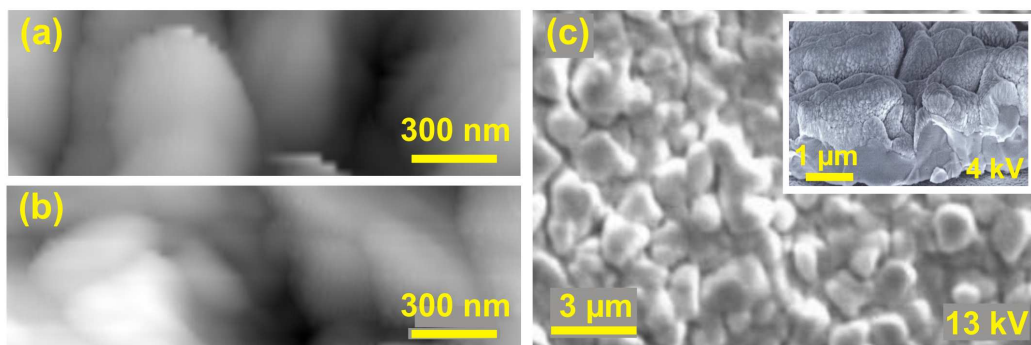


FIGURE 3.23: Topography imaging of a structured surface; (a), (b) show scanning images of a CuInS_2 thin-layer photovoltaic cell, (c) shows a REM image of the surface structure, the inset REM gives another impression of the spatial structure [118].

fabricated by thin-layer technology [118]. In the investigation of epitaxially overgrown semiconductor quantum dots, which is the primary focus of this work, topographical resolution is not very important, even though these dots are detected in topography scans in some cases. However, it can be necessary for a determination of the mechanical stability and the drift rate of the setup, i.p. at low temperatures.

3.6.3 Determination of mechanical stability

The mechanical stability of the setup against external disturbances and thermally induced drift is extremely important for the spectroscopy of single quantum dots, because an unnoticed drift in the position of the tip may lead to a variation in the local excitation density. It is particularly when the sensitivity of the feedback control is attenuated, as it is often necessary for measurements at low temperatures, that a certain rate of lateral drift, or a slight distance variation can occur unnoticed. On the other hand, a sufficiently low drift rate allows a readjustment of the tip position in between local measurements.

A calibration of the setup in terms of positional stability was obtained from repeated scanning images of characteristic areas of the surface of a GaAs semiconductor sample. The four images shown in Fig. 3.24 are taken at successive intervals of 40 min at room temperature. The size of the scanning area is $1.5 \mu\text{m} \times 1 \mu\text{m}$. The images show a prominent feature which is probably due to

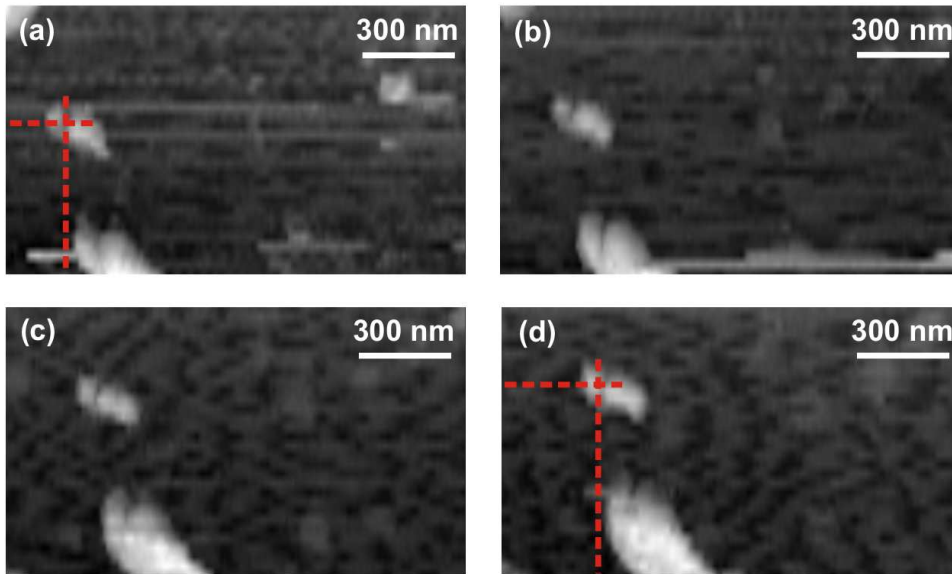


FIGURE 3.24: Drift determination at room temperature. The images (a) - (c) are taken at successive intervals of 40 min. A drift rate of 1 nm per minute is determined equally for the horizontal and the vertical direction.

a contamination. The variation of the position of this feature permits the determination of the drift rate. An equal drift of 1 nm per minute for the horizontal direction (labeled as x) and for the vertical direction (labeled as y) is observed, which conforms to a linear drift of approximately 1.5 nm per minute.

A calibration of the drift rate is likewise performed at low temperatures. Figure 3.25 shows a pair of topography images of $1 \mu\text{m} \times 0.9 \mu\text{m}$ size, which are taken successively at an interval of 30 min at 13 K. A drift of 13 nm in x -direction, and 32 nm in y -direction was detected, which conforms to a rate of $d_x = 0.4$ nm per minute and $d_y = 1.1$ nm per minute, or a linear drift of approximately 1.4 nm per minute on average. The images in Fig. 3.25 show very little distortion, which

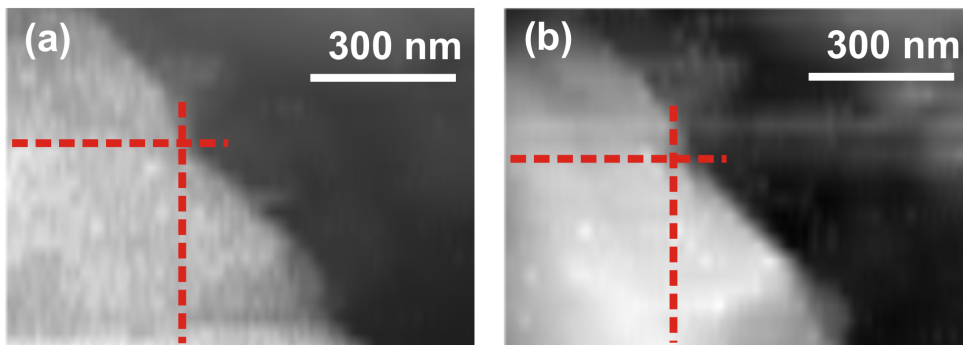


FIGURE 3.25: Drift determination at 13 K. The images (a) and (b) are taken at successive intervals of 30 min. A linear drift of 1.4 nm per minute is determined.

corresponds to the low drift rate. Such stable scanning at low temperatures requires an extremely accurate preparation and a permanent online readjustment of the temperature and the feedback parameters, in order to keep sufficiently steady conditions. However, it is found that nevertheless in practice such cannot be provided for significantly longer than about 60 min. This compels a pragmatic experimental strategy to obtain meaningful quantities of spectra from single quantum dots, as it is described in the following.

3.6.4 Locating of single quantum dots

To pinpoint an appropriate spot out of a scanning image for the investigation of single quantum dot luminescence depends largely on experience and intuition. Due to the self-organized formation of the quantum dots, their distribution on a microscopic scale is inhomogeneous, and the actual quantum dot density can vary considerably within a sample. Since local accumulations of quantum dots may exceed the optical resolution of the probe, the observed features in scanning luminescence images cannot be assigned straightforwardly to signals from single quantum dots. In some cases a group of adjoining quantum dots shows up in a luminescence image as a broadened or asymmetric signal, as in Fig. 3.26 [110].

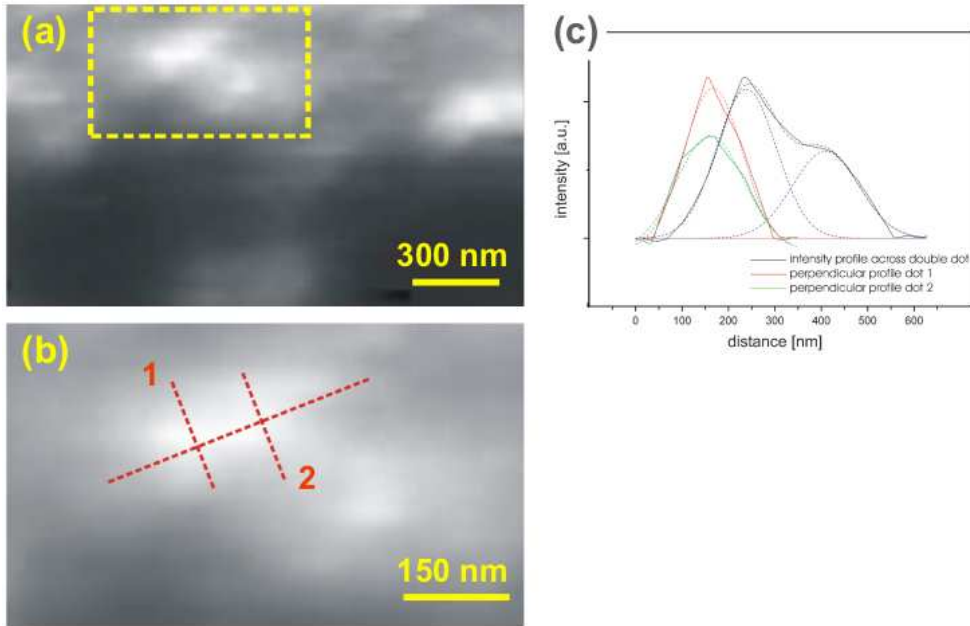


FIGURE 3.26: (a) Asymmetric luminescence feature in scanning image of a InAs/GaAs-quantum dot sample; (b) extension image; (b), (c) intensity profiles across the feature indicate neighboring quantum dots.

Such features can be investigated for intensity variations by taking crosswise intensity profiles, which may indicate neighboring quantum dots, as demonstrated by Fig. 3.26 (b) and (c). However, an interpretation has to be done regarding that such features may actually cover still more quantum dots than indicated by the number of cross-sectional intensity maxima. Furthermore, it has to be taken into account that the statistical variation of the size and the structure of the quantum dots leads to a distribution of their luminescence properties. In a scanning image that is obtained at a certain peak detection energy, different quantum dots show differing signal intensity. An apparently isolated quantum dot may have neighbors which are invisible because their emission is outside the chosen range of detection. Therefore, if possible, scanning images should either be taken repeatedly with different detection energies, or at integrated luminescence, i.e. with a very large spectral range. In order to analyse such searching scans, however, a relatively high resolution is required, both in terms of luminescence intensity, which means a low detection bandwidth, and a high spatial density of points, which results in an increased measurement time. Experience shows that, in general the number of measurements has to be reduced to obtain meaningful results, in favour of reproducibility and a sufficient signal-to-noise ratio. A pragmatic strategy which frequently yields good results is, to initially take an overview scan of a small sample area, and a test spectrum from a promising spot. This test spectrum can be performed quite quickly, if the spectral range is

limited roughly to the region of the expected quantum dot ground state emission. Since at low temperatures the thermal broadening of the quantum dot luminescence is suppressed, signals from neighboring dots can be discriminated by an unexpected line broadening, or additional lines appearing in the spectrum. The potential excitation of higher carrier complexes has to be regarded as well, as it also leads to additional lines [119]. Therefore, the test spectra should be taken with as low an excitation intensity as possible.

3.6.5 Obtained lateral optical resolution

The resolution obtained in photoluminescence scanning images of quantum dot samples depends on the one hand on the quality of the probe, and on the other hand on the thickness and the material of the capping layer on top of the quantum dots. The latter determines the effective distance between the tip and the luminescent object, this way limiting the optical resolution, due to spreading of the light within the material of the cap layer. Accordingly, the diameter of an intensity profile across a luminescence centre can be taken as a measure for the optical resolution, provided that the luminescent spot represents an isolated light source of minimum size, as a single quantum dot. In practice, the principle difficulty of determining whether a certain spot fulfils this requirement is overcome by taking an average value from several suitable spots. Figure 3.27 (a) shows an example scanning image of a sample containing InGaAs quantum dots, taken at a peak detection energy of 0.992 eV [107]. The image is obtained out of a series of measurements which were carried out with a Ag-coated fiber tip. The optical resolution is determined by drawing intensity profiles across suitable luminescence spots, as shown by way of example in Fig. 3.27 (b), and averaging the FWHM of appropriately fitted Gaussian functions. In this way, a spatial

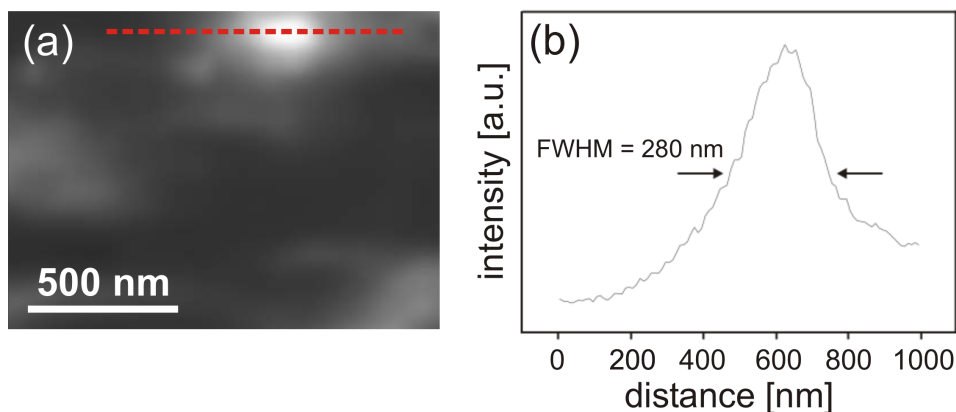


FIGURE 3.27: (a) Scanning image of InGaAs/GaAs quantum dot sample, taken with coated fiber tip; (b) an optical resolution of 280 nm is determined from intensity profile drawn along the dashed line in (a).

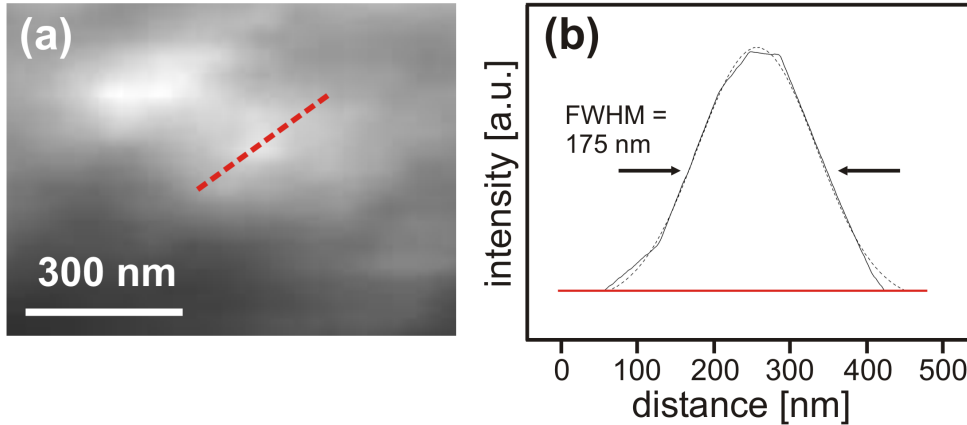


FIGURE 3.28: (a) Scanning image of InAs/GaAs quantum dot sample, taken with uncoated fiber tip; (b) an optical resolution of 175 nm is determined

resolution of about 280 nm is calculated for this tip. For comparison, Fig. 3.28 (a) shows an example out of a series of scanning images of a sample containing InAs quantum dots, which was taken with an uncoated fiber tip [110]. Compared to the wavelength of the detected luminescence of about 1250 nm in vacuum, this value corresponds to a resolution of roughly $\lambda/5 - \lambda/4$. This demonstrates the potential to achieve a considerable improvement in the optical resolution in the nearfield, in comparison to classical far-field microscopy.

Analogous to the measurement shown previously, the lateral optical resolution is determined by averaging intensity profiles drawn across suitable luminescence spots (Fig. 3.28 (b)), obtaining a value of 175 nm, which corresponds to an effective resolution of about $\lambda/7$. In this case the obtained resolution is much better than in the previous measurement, even though an uncoated fiber tip is used. The difference in the obtained resolution of both measurements are partially owing to a different quality of the used fiber tips, but result primarily from a different thickness of the cap layer above the quantum dots.

3.6.6 Low-temperature scanning of quantum dot samples

Despite the limited stability of the shear-force feedback, the new setup permits a scanning of quantum dot samples at low temperatures with a sufficient quality to localize single quantum dots for spectroscopic investigations. Figure 3.29 shows an example scanning image of a sample containing InGaAs quantum dots, which is taken at 80 K with a coated fiber tip [107]. The image has a size of $2 \mu\text{m} \times 1 \mu\text{m}$ and is taken at a peak detection energy of 0.992 eV. The red circle indicates a luminescence signal of a single quantum dot which shows a strong emission at the chosen detection energy. Other bright spots show signals from single quantum dots or groups of quantum dots with a peak emission at a different energy, which are observed in the scanning image because of a remaining

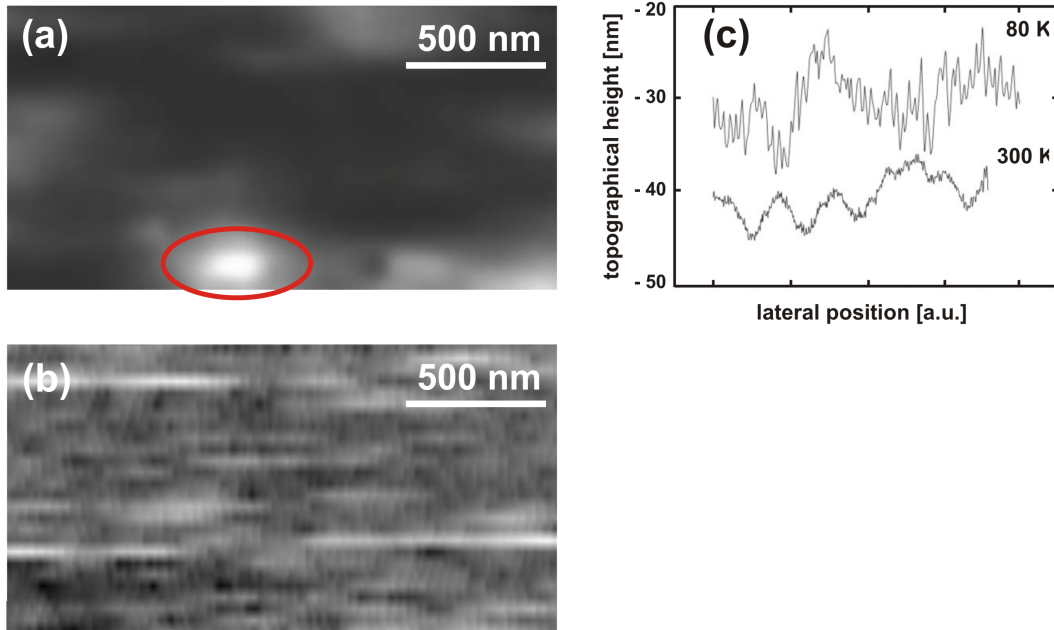


FIGURE 3.29: Scanning of InGaAs/GaAs quantum dot sample at 80 K; (a) image of the luminescence signal, (b) corresponding topography image; (c) comparison of topography profiles at 80 K and 300 K.

thermal broadening of the quantum dot luminescence of about 5 meV at 80 K. The corresponding topography image shown in Fig. 3.29 (b) reveals that the measurement suffers from a considerable noise of about 3 nm on average, which is due to the reduced stability of the shear-force distance control. Figure 3.29 (c) shows a direct comparison of a topography profile from the scanning image 3.29 (b) with a profile obtained from a measurement at 300 K. The profile shows a characteristic noise rate of about 3 nm at 80 nm, which is owing to the increased sensitivity of the distance control mechanism. By contrast, the profile taken at room temperature shows a noise rate that is clearly below 1 nm.

Figure 3.30 shows an example scanning image of an InAs/GaAs quantum dot sample taken at 20 K with an uncoated fiber tip and a peak detection energy of 0.929 eV. The scanning image has a size of $1.5 \mu\text{m} \times 0.8 \mu\text{m}$. Luminescence signals from two single quantum dots are observed, being indicated by the circles in Fig. 3.30 (a). This measurement was performed using a strongly damped tuning fork sensor in order to ensure stable scanning. Furthermore, the set point for the distance control was set extremely high. As visible in the topography image shown in Fig. 3.30 (b), this practice leads to an almost completely suppressed reaction to surface structures, and thus to a loss of topographical imaging. Nevertheless, the image shows an irregular, tapping-like variation of the tip position, which reflects the limited stability of the tuning fork oscillation at low temperatures.

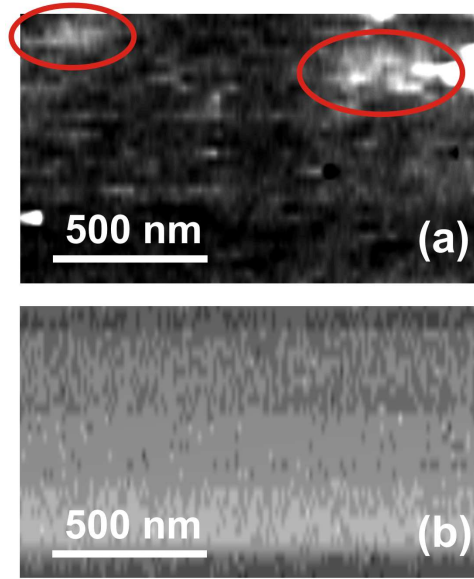


FIGURE 3.30: Scanning image of InAs/GaAs quantum dot sample at 20 K; (a) shows the luminescence image; the circles indicate luminescence of single quantum dots; (b) the corresponding topography scan suffers from considerable noise.

Another example scanning image is shown in Fig. 3.31, which was taken with an uncoated fiber tip at a temperature of 5 K and at a peak detection energy of 1.068 eV. The scanning image has a size of $3.0 \mu\text{m} \times 1.0 \mu\text{m}$. Because this measurement was also performed using a highly stabilized distance control, there is no information obtained from the surface structure, as visible in the topography image Fig. 3.31 (b). Because in this measurement a probe with a very low quality factor was used, the oscillation was much more stable than in the previously presented measurement (Fig. 3.30). However, due to the additionally applied electronic stabilisation of the feedback signal, the reaction of the probe to actual surface structures was lagging considerably. Therefore, the contact between the tip and the surface of the sample was characterized by sudden steps and large areas which are run down in lines at a constant height (Fig. 3.31 (b)). Nevertheless, the luminescence image contains information, which is revealed by an appropriately adjusted image contrast. This processing of the data is necessary because of the low signal intensity in this measurement. The luminescence signals of 3 quantum dots are observed in the image, which are indicated by the red circles (Fig. 3.31). According to this image, an optical resolution of 200 nm is obtained. Moreover, because at a temperature of 5 K the thermal broadening of the quantum dot luminescence is diminished, the measurement was performed with a broad range of detection, in order to increase the probability to observe signals from different quantum dots. As a makeshift solution, overview scans can be performed in principle in a non-contact mode with a slightly retracted tip, this

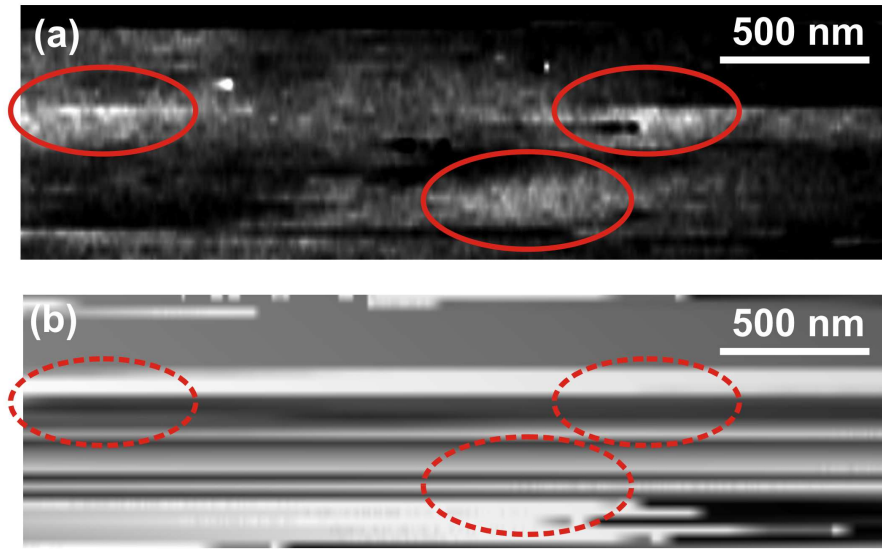


FIGURE 3.31: Scanning image of InAs/GaAs quantum dot sample at 5 K; the circles indicate luminescence of single quantum dots.

way avoiding the necessity for a stable distance control at low temperatures. This method can be applied in particular to samples with a relatively low quantum dot density, where a certain loss of resolution is tolerable. However, such hovering scans also run the risk of a sudden tip crash, since an inclination of the sample is inevitable in practice. Even a small inclination of about 2° will result in a rise of more than 10 nm over a scanning distance of $1 \mu\text{m}$, while on the other hand, when the tip is retracted more than some tens of nm, the luminescence signal decreases strongly and the spatial resolution is reduced considerably. The problem can be managed in principle with the help of an electronic plane compensation, which allows the scanning of an inclined sample at constant height in a very close distance [92]. However, the electronics of the plane compensator have to be adjusted beforehand to the actual inclination, which requires a reliable tip approach at 3 reference points of the intended scanning image. This procedure takes so much time, that often the calibration is not valid any more for the actual measurement because of thermally induced drift. Thus, the spectroscopy of quantum dots at low temperatures is normally performed immediately after taking an overview scan with shear-force control, according to the procedure described above.

Chapter 4

Investigations of III-V semiconductor quantum dots

4.1 Semiconductor nanostructures

4.1.1 Characteristics of quantum-confined semiconductor structures

Semiconductor nanostructures are characterized by a spatial confinement of carriers to dimensions of a few nanometers, which leads to specific electronic and optical properties [14, 15, 18, 120, 121]. They consist typically of a combination of materials with differing electronic band structures, in such a way as to create a constriction of one of them to dimensions below the quantum-mechanical wavelength $\lambda_{deBroglie}$, which is associated with the motion of the carriers within the material. This leads to a quantization of the electronic density of states (DOS) in one, two or three dimensions in space. In the case of a so-called zero-dimensional quantum dot structure, the confinement affects all three dimensions, and the DOS is characterized by a series of discrete, δ -function like states, as is visualized in Fig. 4.1 [120–122].

A closer look at the energy states within such semiconductor nanostructures reveals that they are determined mutually by the material they consist of, and by the details of their spatial structure. The particular size, shape, and the stoichiometric distribution of an individual nanostructure, such as a quantum dot, have substantial influence on the actual quantum-mechanical potential, and thus on its electronic and optical properties [14, 18, 121]. Because further the specific geometry of such a semiconductor nanostructure impedes an analytical calculation, an accurate theoretical description of the electronic structure requires a numerical treatment [122, 123]. However, in a first approximation a nanosized semiconductor structure can be characterized using a simplified potential geometry which allows the treatment of the energy states of the confined carriers analogous to

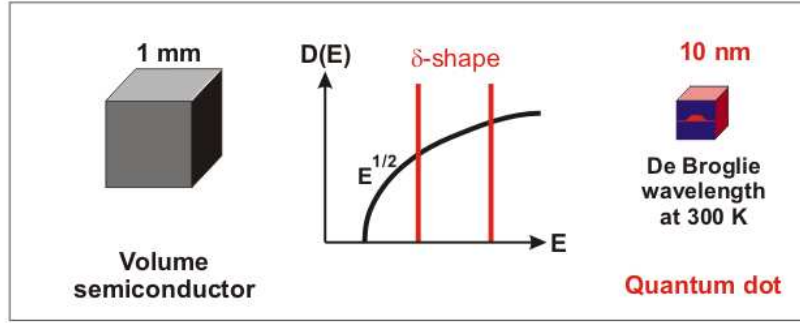


FIGURE 4.1: Comparison of the electronic density of states of a volume semiconductor, showing a $E^{1/2}$ dependence, to the discrete energies with a delta-like shape of the 3D-confined quantum dot structure.

the harmonic oscillator model¹ [26].

4.1.2 Self-organized formation of In(Ga)As/GaAs semiconductor quantum dots

In view of a technological application it is important to control the properties of semiconductor quantum dots in the fabrication process [20]. Semiconductor quantum dots are fabricated primarily using technologies such as, e.g., metal-organic chemical vapor deposition (MOCVD) or molecular-beam epitaxy (MBE) [121]. These technologies are making use of self-organized formation processes during the epitaxial growth of semiconductor materials with different lattice constants, thus creating a heterojunction structure [2, 124]. The formation processes can be distinguished into three different modes [125]: (i) the layer-by-layer Frank-van der Merwe growth [126], (ii) the Volmer-Weber mode generating single, separated material islands [127], and (iii) a combination of both, which was found by Stranski and Krastanov, leading first to the growth of a so-called wetting layer (WL) of a few monolayer thickness, before taking advantage of the formation of material clusters for degradation of lattice strain [128]. Which mode it is that emerges actually depends on the lattice constants of both materials, and the relation of the free enthalpies of their surfaces to the material interface [129]. The properties of the generated structures are determined on the one hand by the material parameters, particularly the relative lattice mismatch, and on the other hand by the specific growth parameters, such as the supply of constituent materials, the growth rate, the temperature, and timed growth interruptions [20, 130].

The following introduction is focused on type In(Ga)As/GaAs quantum dots,

¹This simplification mostly holds for the strong confinement regime, i.e., if the confinement energy given by the quantum dot potential is larger than the influence of the Coulomb-interaction of the carriers within the quantum dot.

which were investigated in the frame of this work. These quantum dots are formed by self-organized growth in the Stranski-Krastanov mode during heteroepitaxy of either InGaAs or InAs on GaAs, respectively [125]. For this purpose the chosen material is deposited on the (001)-surface of a GaAs substrate, resulting in the formation of a wetting layer of 1.7 – 1.8 monolayers which is strained because of a lattice mismatch of about 7% between both materials [131, 132]. With further deposition of material, the necessity to reduce the strain leads to the formation of three-dimensional islands, which are overgrown later with subsequently deposited GaAs material for technological application [133]. The size of the quantum dot islands depends largely on the supply of material, while local conditions, such as the strain field, the stoichiometry and the after-effects of growth kinetics, rather determine their shape and atomic structure [134, 135]. In general, an extended deposition of material contributes to progressing quantum dot growth, while the thickness of the wetting layer remains constant [125]. In the case of a regularly layer-wise quantum dot growth, a number of discriminative sub-ensembles of quantum dots with different sizes but similar structure can often be found within a sample, which is known as *monolayer-splitting* [136–139]. Furthermore, the capping layer grown on top of the quantum dots exerts a strong influence on their eventual size and shape by means of a subsequent modification to the strain field, and to segregation effects [140–143].

Many technological applications require samples which are as homogeneous as possible in terms of the distribution and the physical properties of the contained quantum dots. In order to promote the formation of homogeneous collectives of quantum dots, the growth parameters have to be kept uniform as possible during sample fabrication. Such is brought forward in MOCVD fabrication, e.g., by providing a laminar flow of chemicals, and by the utilization of a rotating substrate wafer. If, by contrast, a sample is grown without wafer rotation, a strongly inhomogeneous distribution of quantum dots is obtained, containing gradient densities of quantum dots with significantly different properties [144].

4.1.3 Atomic structure

In terms of structure, a semiconductor quantum dot can be characterized roughly by its shape, size, local stoichiometry and geometrical symmetries, which in a first approximation determine the electronic properties in mutually dependent relation with the electronic bandgap of the quantum dot material [145]. In the case of a typical In(Ga)As/GaAs quantum dot, a pyramidal shape emerges during the growth [146, 147], which is then transformed as a result of the capping process into the shape of a truncated pyramid [140, 141, 148, 149]. The pyramids are characterized by a basically four-sided base with a diameter varying between 10 nm, up to about 20 nm, and a height of about 2 – 6 nm, typically [125, 140, 150]. The model of a truncated pyramid with an approximately rectangular base permits a number of elementary calculations of the electronic properties of the quan-

tum dots. However, because of the strong dependence on small variations in the particular morphology, an accurate calculation requires precise information on the atomic structure of the pyramids, such as the types of facets and their edges, the stoichiometry and the resulting distribution of the lattice strain, and of the piezoelectric fields [122, 123, 145, 151]. For In(Ga)As/GaAs quantum dots, in particular the influence of the specific stoichiometry profile must be considered, which is characterized by an In-rich inverted cone [152–154]. Furthermore it was shown that, in terms of the electronic potential, the strain-related piezoelectric fields within these quantum dots result in a transformation of the geometrical symmetry [145]. This has a significant effect on the actual distribution of the carrier wavefunctions within the quantum dots, leading to variations in their electronic interaction and recombination properties.

4.1.4 Electronic properties

Although the particular electronic properties of a quantum dot depend on the details of its individual atomic structure [155], at first order it can be characterized by the confinement of carriers, which leads to an increase of the overlap of their wavefunctions, and hence of the oscillator strength of the radiative recombinations, in comparison with the bulk material [156]. Because of the spatial confinement in all three dimensions, a quantum dot shows discrete, δ -function like energy states, which appear in the dot area in addition to the bands of the host material. Furthermore present are the states of the wetting layer, which are of quantum-well character, as well as additional high-energy quantum dot states (so-called resonances), which couple to the energy bands of the host [157, 158]. Figure 4.2 shows a simple diagram of the electronic structure of a model InAs/GaAs quantum dot. This simplified model of a semiconductor quantum dot allows for some considerations about its electronic properties, even though an analytical solution of Schrödinger's equation is impossible in most cases [92]. In general, a stronger confinement leads to larger quantization effects, i.e. an increase in the energy of the electronic states [122].

The most simple configuration of carriers in a quantum dot is the population with a single carrier, which can be either an electron or a hole. In terms of a radiative relaxation, the confinement of an electron and a hole together is of major interest. This configuration is commonly called a confined exciton (X). In order to draw further conclusions on the details of the electronic structure, more complex calculations can be done with the help of numerical models, such as the pseudopotential-approach [123, 159] or the 8-band $\mathbf{k} \cdot \mathbf{p}$ theory [122, 156]. Such simulations reveal for instance, that pyramidal dots can show a complicated variety of energy states which are not necessarily equidistant [122, 156]. As was observed in the photoluminescence spectra of quantum dots of different aspect ratio, the states become the more equidistant the flatter the quantum dots are [160, 161]. Furthermore, the confinement potential may allow for a population

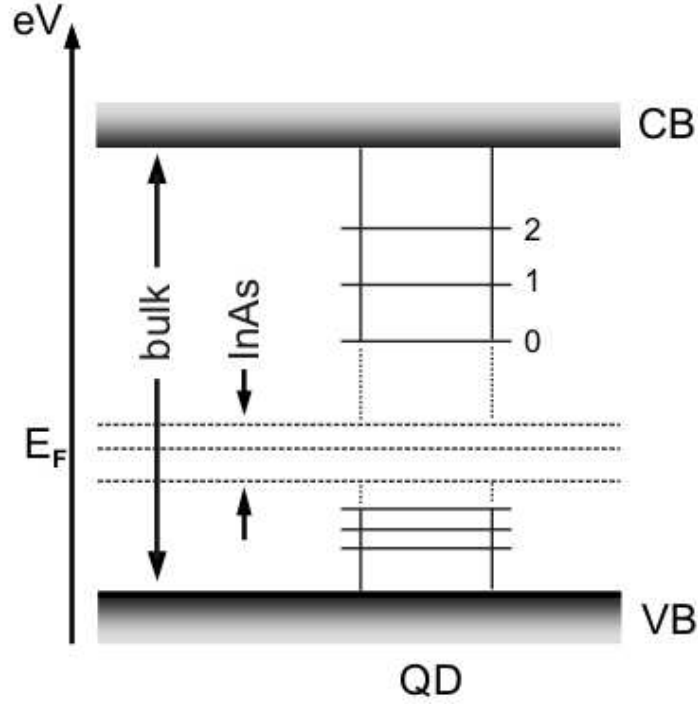


FIGURE 4.2: Electronic structure of an InAs/GaAs quantum dot. The spatial confinement results in the formation of discrete energy states in addition to the bands of the GaAs bulk.

of a quantum dot by multiple carriers, and the formation of exciton complexes which are not stable in the bulk crystal [162]. The energies of the corresponding multiple-carrier states are determined by a calculation of the single-particle states and the Coulomb interaction within the excitonic complexes [160]. In a quantum-mechanical notation, the Hamiltonian describing the multiple-carrier system can be written as the sum of the single-particle Hamiltonians $\sum_i^{a+b} H_i$ of the electrons and holes, with a second part covering the operators of the respective Coulomb interaction of all contained pairs of carriers [26]:

$$H = \sum_i^{a+b} H_i + \sum_{i \neq j}^{a,b} \frac{1}{8\pi\epsilon} \frac{e^2}{|\mathbf{r}_i - \mathbf{r}_j|} . \quad (4.1)$$

In this notation, all the location-dependent influences are comprised in the single-particle terms. The corresponding spectra of the energies and the states can be determined by solving the appropriate stationary Schrödinger equation. The next charge-neutral state within a quantum dot is the so-called biexciton (XX), which is given when two pairs of carriers are confined therein [163]. The recombination of the biexciton normally takes place by cascade, with initially a dissociation into a photon and an exciton, and secondly, the recombination of the latter [164].

Because of the mutual Coulomb interaction, the additional carriers affect the energy of the recombination of a single exciton out of the biexciton state [165]. The interaction can be net either attractive or repulsive, which means that the transition energy is either lowered [166, 167] or raised [162] in comparison to the energy of the solitary exciton, as is shown schematically in Fig. 4.3 [26, 165]. Correspondingly, the biexciton state is characterized as either binding or antibinding, and the energy difference is called the positive or negative binding energy of the carrier complex, respectively. The energy of an exciton complex (e.g. a biexciton) also depends on the structural properties of the particular quantum dot, as well as its respective binding energy.

It was shown recently that there are systematic correlations between the structural parameters of quantum dots and the states of specific excitonic complexes [26]. For In(Ga)As/GaAs quantum dots there was found to be a general tendency of the binding energies of carrier complexes to decrease with an increasing single-exciton energy, i.e. with smaller quantum dots [165]. In the case of the biexciton, a change from a binding situation towards an antibinding state can be observed with a decreasing size of InAs/GaAs quantum dots, while for InGaAs/GaAs quantum dots the biexciton state is always binding, even though no systematic correlation between the energy of the exciton and the binding energy of the biexciton state can be found [26]. The typical values of the biexciton

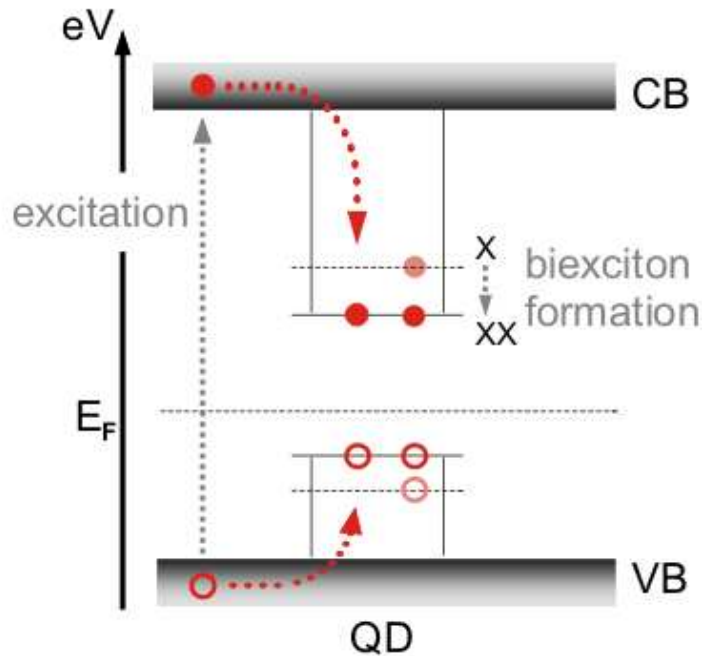


FIGURE 4.3: Formation of a biexciton (XX) in a quantum dot. The interaction of the additional carriers with the present electron-hole pair (X) in the quantum dot leads to a variation of the energy for the collective state.

binding energies which are reported for these material systems vary from about -7 meV to 5 meV [160, 165, 167–169].

The exciton and biexciton are the two possible configurations of carriers in the ground state of a net charge-neutral quantum dot. A population of potentially existing higher, so-called excited states can lead to the formation of higher exciton complexes. The corresponding energies and recombination sequences of such multi-excitons are extremely complex owing to the manifold configurations of carriers which are possible, so that no general scheme can be announced [26]. Merely for the case of a single carrier interacting with an exciton or a biexciton state a number of systematic investigations were performed [26, 166, 167, 170]. Such charged states can form in particular when a sample has an enhanced background doping, which is often necessary to facilitate technological applications [100]. In this case, the quantum dots frequently carry a permanent charge which is induced by incorporated or nearby located doping atoms [171]. Because of this, the according recombinations often display strong emission and can become quite prominent in photoluminescence spectra [100]. Charged excitons also display binding or antibinding behavior: for the negatively-charged exciton (X^-) a generally binding effect is observed for In(Ga)As/GaAs quantum dots, whilst for the positively-charged exciton (X^+) a continuously antibinding behavior is reported [26]. The corresponding binding energies vary from -14 meV to 9 meV.

4.1.5 Luminescence characteristics

The recombination of an electron-hole pair within a quantum dot can lead to radiative emission, in accordance with the selection rules giving respect to the angular momentum of the respective quantum mechanical states. The spectral width of the emitted luminescence lines is determined basically by the uncertainty relation, which yields a reciprocal relation between the decay time T_{rel} and the bandwidth Δf_{hom} of the corresponding electromagnetic oscillation in a semi-classical model [172]. In the quantum-mechanical view, the significant time interval for a radiative recombination between two discrete energy levels is the phase-relaxation time T_{rel} of the excited state, which is determined by different phase-destroying processes [173]. The corresponding emission shows the profil of a Lorentzian function with the homogeneous linewidth Δf_{hom} given by

$$\Delta f_{hom} = \frac{2\hbar}{T_{rel}} \quad . \quad (4.2)$$

The most relevant dephasing processes which affect the states of carriers within a quantum dot are, the energy relaxation, as well as the elastic or inelastic scattering with phonons and free carriers. The resulting linewidth Δf_{hom} is of the order of some μeV , typically.

In contrast to the ideally isolated atom, a semiconductor quantum dot is usually in permanent physical contact with the surrounding host material, which leads to a number of additional phase-destroying effects rendering a homogeneous broadening of the photoluminescence lines. With the bandwidth Δf_{hom} of a radiative transition in a quantum dot being described by Eq. 4.2, the dephasing time T_{rel} is given as the net phase-relaxation time of all dephasing processes:

$$\frac{1}{T_{rel}} = \frac{1}{2T_e} + \sum_i \frac{1}{T_i^*} \quad , \quad (4.3)$$

with the energy-relaxation time T_e , and T_i^* comprising the other dephasing processes which do not affect the energy of the state² [26].

For this work, the elastic scattering with phonons is of primary relevance, which leads to a temperature-dependent line broadening. It can also be described as a thermal activation of the carriers [28]. If the scattering with acoustic and LO-phonons is the dominating line-broadening mechanism, the temperature-dependent linewidth broadening Δf_{hom} can be described by:

$$\Delta f_{hom}(T) = \Delta f_0 + \gamma_{ac} \cdot T + \gamma_{LO} \cdot \frac{1}{\exp\left(\frac{\hbar\omega}{k_B T}\right) - 1} \quad , \quad (4.4)$$

with the temperature T , the linewidth Δf_0 at $T = 0$ K, the coupling parameters γ_{ac} and γ_{LO} for the interaction with acoustic and LO-phonons, respectively, and the medial energy of the LO-phonons $\hbar\omega$ [26]. Besides line broadening, the lattice temperature has a strong influence on the photoluminescence intensity of semiconductor quantum dots. In general, the luminescence intensity of a semiconductor decreases with increasing temperature, which is the net result of a number of different effects: The probability for a non-radiative recombination of free carriers via phonon states or lattice defects increases with increasing temperature, due to a stronger population of phonon states in the solid material [175]. The extended diffusion length of the free carriers enables them to reach such non-radiative centers more frequently. Additionally, the increased diffusion facilitates the spatial separation of electrons and holes within the material. And eventually, localized carriers are emitted thermally from radiative states, and free carriers are hindered from a relaxation into localization centers through frequent phonon scattering at higher temperatures [176].

In a quantitative description, the carriers get lost for a recombination from a certain state E_0 by thermal activation into higher levels $E_{1,2,\dots}$, from where they can relaxate radiatively or non-radiatively. The remaining luminescence intensity depends on the temperature T by:

$$I(T) = \frac{I_0}{1 + \sum_i B_i \cdot \exp\left(-\frac{\Delta E_{0i}}{k_B T}\right)} \quad , \quad (4.5)$$

²If there are no other effects involved and the energy-relaxation is the only process that affects the phase, there is $T_{rel} = T_e$. An experimental method to determine T_{rel} directly is the four-wave mixing technique [174].

with the intensity I_0 at $T = 0$ K, the rate B_i of degeneration between levels 0 and i , and the energy distance ΔE_{0i} between the levels 0 and i , respectively [177]. In the case of a quantum dot, the higher levels E_i may either consist of excited quantum dot states, or resonances, wetting layer states, or states from the bulk material. Furthermore, temperature has an influence on the transition energy of a semiconductor structure in general. Since the balanced distance between the atoms in a crystal lattice grows with increasing temperature, a general decrease of the material bandgap takes place at higher temperatures, and with it a decrease of the transition energy of the luminescence emission [178].

A strong effect is induced also by the temperature dependence of the effective masses of the carriers which in principle decrease with increasing temperature [179]. Additionally and in principle, the variation of the quantization energy due to the modified spatial dimensions of the quantum dot has to be considered. The latter effect is, however, rather weak and can be neglected in the normal case, along with the temperature-dependent variation of the dielectric constant, which has an influence on the Coulomb energy: the more so as neither of these contributions have been sufficiently grasped yet in terms of a quantitative description [26].

An additional variation in the luminescence emission of a quantum dot is possible owing to an interaction with external electric fields, which can be induced by defects within the crystal lattice of the host material, incorporated doping atoms, surface and interface states, or externally applied voltages. Their effect on the states within a quantum dot is described in general by the quantum-confined Stark effect (QCSE) [180]: an external field tilts the bandstructure of the material, which results in a variation in the relative energies of the electron and hole states in the quantum dot. As a result, the overlap of the particle wavefunctions and the Coulomb interaction between the confined carriers is modified, and thus the oscillator strength of a radiative transition among them [181]. The existence of a permanent vertical dipol moment is suggested [182, 183] as the result of a local separation of the wavefunctions of electrons and holes [184], or a local stoichiometry gradient within the quantum dot [152], whose interaction with the external field gives an additional contribution.

Since these interactions can vary strongly on relatively short timescales, the induced shifts of the transition energies result in a broadening of the luminescence lines which are observed in time-integrated spectroscopy. The pattern of this so-called spectral diffusion can be recognized in detail only in time-resolved spectroscopy, yet in some cases a corresponding variation in the luminescence signal is also observed over a relatively large time interval of several seconds [100].

The analysis of a quantum dot spectrum is based on a theoretical modeling of the electronic transitions, and a comparison with related experimental data such as there are shown in Fig. 4.4 [26]. Because currently the database for In(Ga)As/GaAs quantum dots with a ground state energy in the region of 1.0 eV

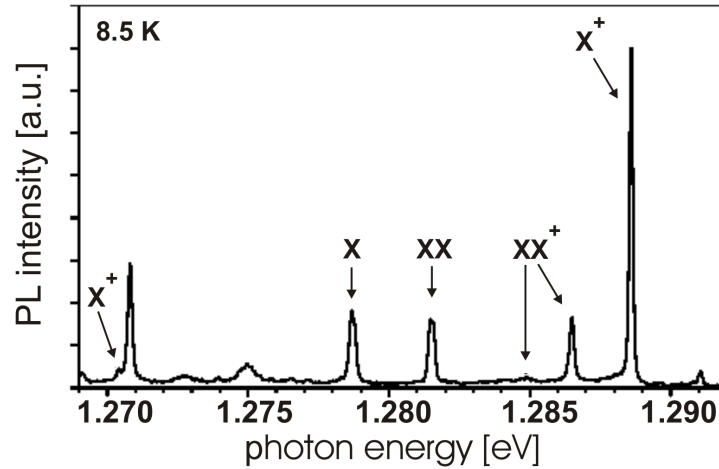


FIGURE 4.4: Complete assignment of the cathodoluminescence emission peaks of a single InAs/GaAs quantum dot [26].

is fairly weak, a transference of information from quantum dots with a considerably higher ground state emission energy is taken as a reference [26, 160]. An extrapolation of the systematics shown in Fig. 4.1.5 for InAs/GaAs quantum dots with a ground state emission between 1.20 eV and 1.35 eV suggests that, with a shift of the ground state emission towards 1.00 eV, a number of considerable changes may occur in their electronic and optical properties [26]. Particularly for the binding energy of the biexciton (XX) a transition from an antibinding state towards a binding state is expected, as well as for the positively-charged biexciton (XX^+). Likewise, for the positive trion (X^+) a decrease of the antibinding influence, or even a transition into a binding state occurs, as is illustrated in Fig. 4.1.5.

A thorough examination of the information allows the gathering of a number of general propositions on the optical properties of the investigated system:

At large, the luminescence spectrum of an InAs/GaAs or InGaAs/GaAs quantum dot can be expected to consist of a series of emission peaks which are separated by several tens of meV, typically. These peaks can be assigned to recombinations of different electron states. At high temperatures, they will show a thermally induced broadening of some meV, which covers the pattern of the transitions into different hole states, being separated by just a few milli-electron volt, because of the lesser effective mass of the holes [28, 29, 185].

At appropriately low temperatures a dissolution of the broadened signals into bunches of well-separated, narrow lines can be expected, which represent emissions from the various radiative recombinations that can take place in between the different electron and hole states, in accordance with the possible populations of the states and the selection rules. With regard to the population with carriers it can further be expected that, with increasing excitation intensity the emission

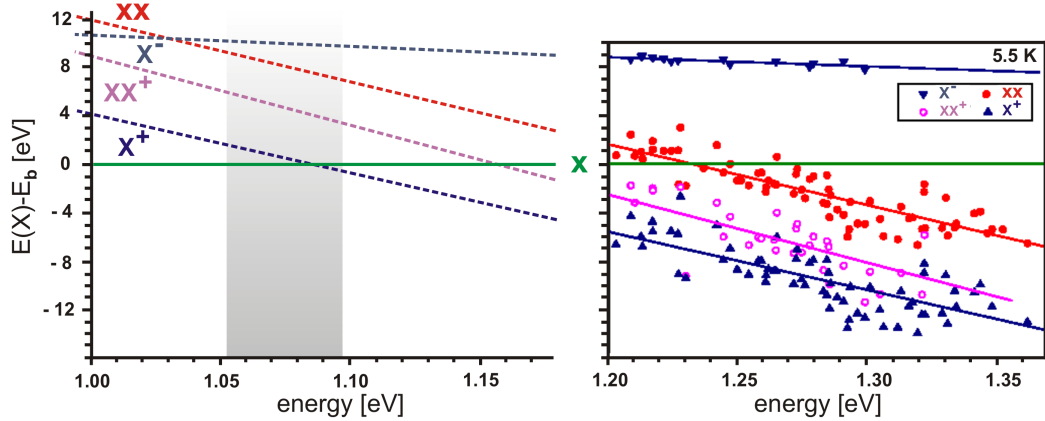


FIGURE 4.5: Binding energies of excitonic complexes in InAs/GaAs quantum dots (extrapolation after [26]); the grey-shaded area indicates the region of the ground state energies of the quantum dots in the investigated sample.

from the exciton state saturates, and later on shows a decay, whilst the emissions from the biexciton and the trion states become more prominent. With the rise of the biexciton line, the emission from a first excited electron state will also appear, provided that such exists within the quantum dot. In general the intensity of the single exciton line can be expected to follow a linear increase, whereas the intensity of the biexciton signal will rise quadratically, due to the respective probabilities of a population with carriers [163, 186]. Further, the interaction with carriers being co-existent in an excited (electron) state will have an influence on a possible recombination of ground state carriers, hence leading to the appearance of additional lines at high excitation intensities [168]. Moreover, there are excited hole states to be considered, which may provide additional relaxation channels, thus also leading to additional lines at energies between the electron ground state and the first excited state, with respect to the selection rules [100].

In terms of a detailed assignment of the lines the following can be assumed further on, on the basis of the examined information:

In general, the binding energy of the biexciton (XX) should be positive for InGaAs/GaAs quantum dots, as well as for InAs/GaAs with low ground state energies, i.e. the emission from a recombination out of this carrier complex will be of lower photon energy than the signal from the single exciton (X) in the electron ground state. The same is expected for the emission from the negatively-charged exciton (X^-). Quantitatively, the binding energy of the negative trion (X^-) should be higher than that of the neutral biexciton (XX). A positive binding energy is to be expected further for a positively-charged biexciton (XX^+).

By contrast, the positively-charged exciton (X^+) may either be binding or antibinding. According to a linear extrapolation of the systematics found for InAs/GaAs quantum dots with ground state energies of 1.20 – 1.35 eV [26], the

behavior of the positive trion (X^+) will be related decisively to the energy of the ground state of the respective quantum dot. The transition from an antibinding towards a binding state will take place between an energy of 1.05 eV and 1.10 eV of the single exciton recombination. This is precisely the region of the ground state energy of the quantum dots investigated in this work. Therefore, a definite prediction of the sign of the binding energy of the positively-charged exciton (X^+) cannot be given solely based on data obtained from quantum dots with higher ground state energies. According to the linear extrapolation, in each case the value of the binding energy will be rather low. However, the behavior of the states in quantum dots with lower ground state energies does not necessarily need to be strictly linear. Thus, for an assignment of the peaks in luminescence spectra other indications such as their relative intensity gain in equal importance.

4.2 Characterization of the samples

4.2.1 InGaAs/GaAs quantum dots

The first sample which was investigated in this work contains InGaAs quantum dots in a GaAs matrix grown by MOCVD [187]. For that, a layer of nominally 0.94 nm of $\text{In}_{0.4}\text{Ga}_{0.6}\text{As}$ was deposited on the 001 surface of an undoped GaAs substrate in a MOCVD reactor with rotating susceptor, leading to the formation of a wetting layer of about 1.7 monolayers, and a subsequent emerging of quantum dots in the Stranski-Krastanov mode. Thereafter, a cap layer of about 100 nm was deposited on top of the quantum dots, which consists of GaAs. This includes a diffusion barrier of 30 nm of $\text{Al}_{0.3}\text{Ga}_{0.7}\text{As}$, in order to reduce the loss of carriers by non-radiative recombination at the sample surface, thus increasing the efficiency of photoluminescence excitation. The sample structure is shown schematically in Fig. 4.6 (a), together with a cross-sectional scanning tunneling (XSTM) image of an InGaAs/GaAs quantum dot in Fig. 4.6 (b), which is taken from a sample that had been grown with comparable parameters [135]. The image indicates a quantum dot shape of a truncated pyramid with a baselength of about 17 nm, and a height of about 4 nm, which corresponds to other structural investigations using XSTM [140], transmission electron microscopy (TEM) [188], as well as theoretical simulations [125].

However, since for principally technical reasons no direct investigation of the structural parameters of the sample were possible, the information on the quantum dots investigated in this work is based merely on the specifications of the growth process, and the analogy of comparable samples. These investigations of comparable samples in particular found a specific stoichiometry distribution for

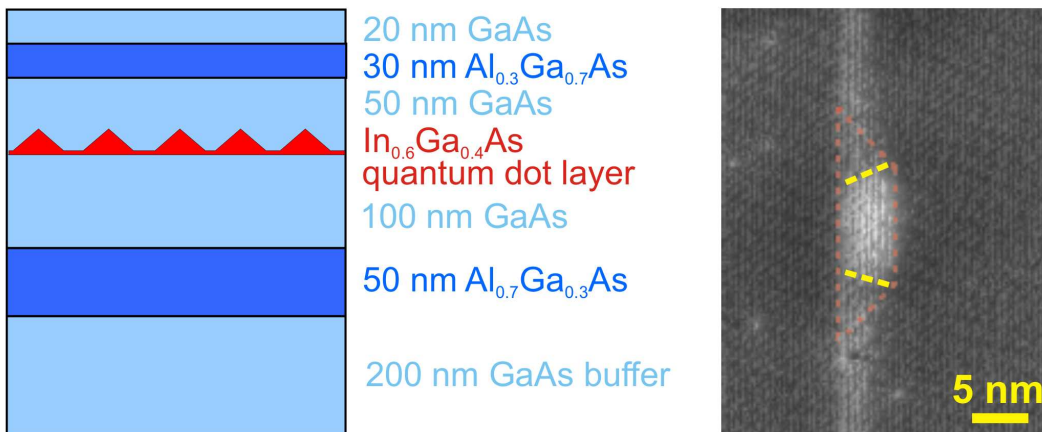


FIGURE 4.6: (a) Structure of the InGaAs/GaAs quantum dot sample; (b) XSTM image of comparable InGaAs/GaAs quantum dot [135]; the dashed lines indicate the shape of the quantum dot and the stoichiometry profile.

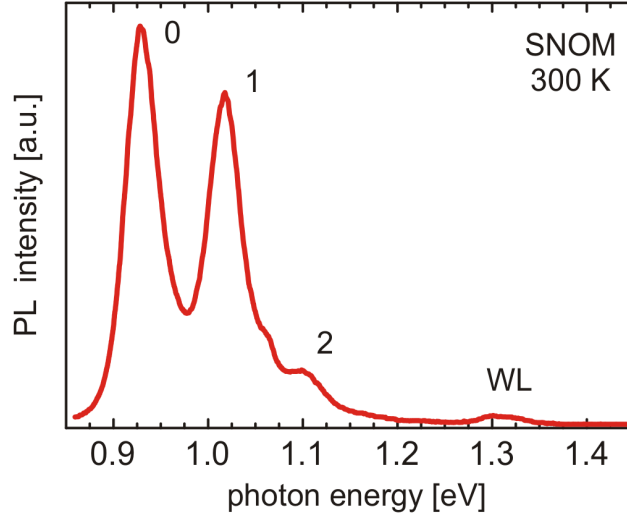


FIGURE 4.7: Ensemble PL of InGaAs/GaAs quantum dot sample at 300 K. The peaks originate from recombinations of the ground state (0), the first (1) and the second excited states (2) of the quantum dots, as well as from the wetting layer (WL).

InGaAs/GaAs quantum dots, which is characterized by an In-rich core showing the profile of an inverted, truncated cone (Fig. 4.6 (b)) [154]. According to former experiments, a quantum dot density of $10^8 - 10^9 \text{ cm}^{-2}$ was determined for the sample, which is equivalent to an average of 1 to 10 dots per μm^2 [189]. With respect to the thickness of the capping layer, hence a spatial resolution of at least a few 100 nm is required to investigate single quantum dots. This can be obtained with the SNOM using Ag-coated fiber tips.

Figure 4.7 shows a photoluminescence (PL) spectrum of an ensemble of quantum dots, taken at 300 K with a fiber tip at far-field distance [189]. The emission from the wetting layer, as well as from the quantum dot ground state, and the first and second excited electron state can be identified. At this temperature, the ground state has a peak energy of 0.92 eV, the first excitation of 1.02 eV, and the second excitation of 1.10 eV, whilst the wetting layer signal shows up at an energy of 1.31 eV.

For comparison, Fig. 4.8 (a) shows a micro-photoluminescence (μ -PL) spectrum of the sample at 10 K [144]. Fig. 4.8 (b) shows the region of the quantum dot emission at a larger scale. The emission from the wetting layer is shifted towards 1.36 eV, according to the lower temperature (Fig. 4.8 (a)). A luminescence signal is visible in the region of 1.00 eV, which represents the quantum dot ground state at 10 K (Fig. 4.8 (b)). The higher states are just weakly populated, due to the low excitation density. A small signal from the first excited state can be observed, showing up in the form of a tailing of the ground state peak up to about 1.10 eV.

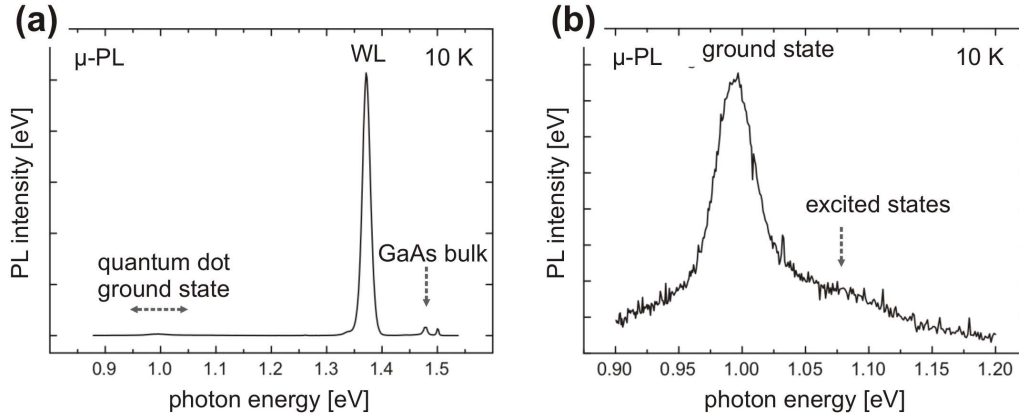


FIGURE 4.8: (a) Micro-photoluminescence spectrum of InGaAs/GaAs quantum dots; (b) extension showing the emission of the quantum dots in detail.

4.2.2 InAs/GaAs quantum dots

The second sample that was investigated in this work contains InAs quantum dots in a GaAs matrix, being grown by MOCVD analogous to the first sample, but with a non-rotating susceptor [144]. This led to the formation of a specific distribution profile of the quantum dots and to a local variation of their growth parameters. Therefore, the sample is characterized by a strongly varying quantum dot density, containing InAs/GaAs quantum dots of widely differing properties within a distance of a few millimeters.

Figure 4.9 shows a schematic of the sample structure. Due to the spatial inhomogeneity of the sample there is no reliable information obtainable on the structural properties of the investigated quantum dots. Investigations using XSTM and TEM were performed on different, more uniform ensembles of quantum dots, which are grown with comparable parameters [140, 190]. These generally support the model of a truncated-pyramid shape of the quantum dots, with a baselength between 10 nm and 20 nm, and a height between 2 nm and 6 nm. More specifically for InAs quantum dots grown on the GaAs-(001) surface, in principle a shell-like formation was found [135], which may cause a monolayer-splitting among the quantum dots, which is reflected in an incremental distribution of the ground state emission energy [137, 139]. However, the directional flow of material during the growth process may have led to even deviant quantum dot structures in the present sample. Regarding the thickness of the capping layer on top of the quantum dots, a value of nominally 120 nm GaAs is announced, including a diffusion barrier of 20 nm of AlGaAs [144]. However, in the SNOM investigations an optical resolution of the order of 150 nm is obtained, which allows to perform the measurements on the sample using uncoated fiber tips. Such a high spatial resolution suggests that actually the cap layer within the sample is thinner than it is announced according to the growth parameters.

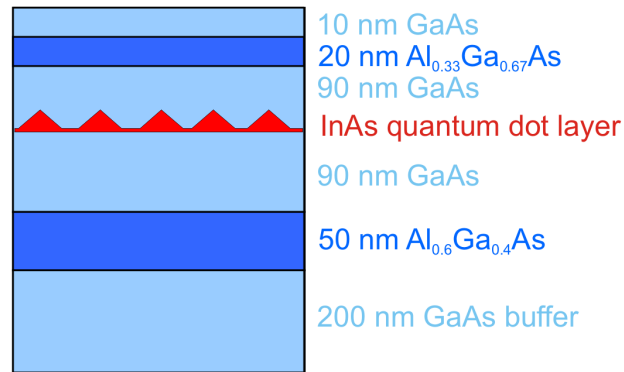


FIGURE 4.9: Structure of the InAs/GaAs quantum dot sample.

Due to the particular growth conditions, for the InAs/GaAs quantum dot sample no definite quantum dot density can be specified. Therefore, the local density of quantum dots has to be determined with the SNOM for any specific sample area, before a spectroscopic investigation of individual objects can be performed.

An example scanning image from the sample is shown in Fig. 4.10 [108]. The image was obtained using an uncoated fiber tip at integrated luminescence, with a medial detection energy of 0.995 eV, this way gathering the ground state emission signals of different quantum dots present in the area. A number of 11 luminescent spots of strongly different intensity are observed, which can be assigned to emissions from quantum dots, being indicated by the colored circles. With an image size of $3 \mu\text{m} \times 1 \mu\text{m}$, a quantum dot density of approximately $4 \mu\text{m}^{-2}$ is determined. The image demonstrates the inhomogeneity of the sample in terms of both, the density of the contained quantum dots, as well as their electronic properties. While in the center part of the image an accumulation of bright spots is recognized, other areas of comparable sizes show just a few spots with considerably weaker luminescence. An extended mapping of the sample yielded a varying density of $10^6 - 10^9 \text{ cm}^{-2}$ luminescent spots. Such mapping allowed a selection of areas with a density of $1 - 10 \mu\text{m}^{-2}$ for the spectroscopy measurements. This is high enough to locate a quantum dot within the respective area even at low temperatures by a small test scan of a few 100 nm in diameter, whilst still providing a sufficient separation of quantum dots to allow single-dot investigations. As visible in Fig. 4.10, some of the spots show an elongated shape, which can be an indication that actually two or more quantum dots are contributing to the observed emission feature [108]. In some cases, clarity about this issue can be obtained by drawing intensity profiles. However, this technique provides merely a minimum number of potentially covered quantum dots. By contrast, a repeated scanning of the sample area at varied detection energies allows the imaging of different peak emission signals of different quantum dots in the area, thus giving complementary information on the assemblage which is underlying a lumines-

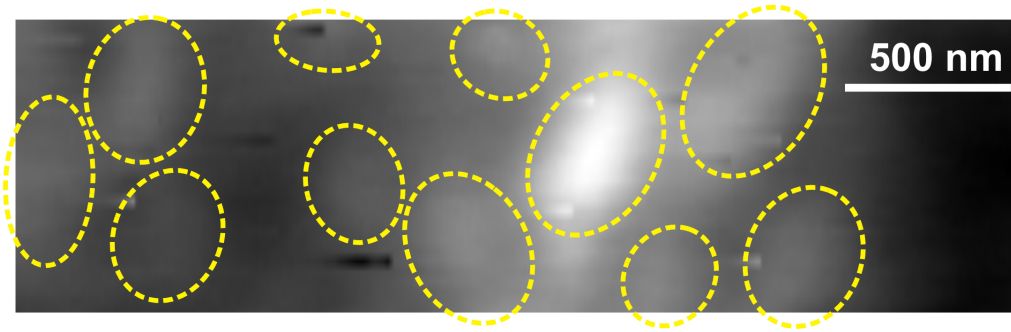


FIGURE 4.10: Example scanning image of the InAs/GaAs quantum dot sample, taken with integrated luminescence. The luminescence spots are assigned to ground state emission signals of different quantum dots.

cence spot. The choice of an appropriate spectral range of detection for the scans allows a co-detection of luminescence of lesser intensity from other quantum dots, as like in Fig. 4.10. This way, a characteristic pattern can continuously be recognized in the luminescence images, which provides information on the spatial distribution of quantum dots with differing luminescence. Such information is particularly valuable for investigations at very low temperatures, where the thermal broadening of the quantum dot luminescence is suppressed, and scanning has to be performed with a broad range of detection in order to observe the signals from different quantum dots in the searching scans.

This procedure of scanning a sample area at varying detection energies is demonstrated by the series of images shown in Fig. 4.11 (a) - (d) [108]. The images Fig. 4.11 (a), (b) and (c) show the luminescence from the ground state recombinations of a group of different quantum dots, imaged at different detection energies of 1.008 eV (a), 1.004 eV (b), and 1.001 eV (c), respectively. The image shown in Fig. 4.11 (d) was taken with a broadened spectral range, thus showing the integrated emission of the area. A characteristic pattern of luminescence features is apparent in Fig. 4.11 (a), (b) and (c), which is indicated by the colored circles, and a variation in the intensity of the different spots can be observed. In particular the feature (1) shows significant variation: this spot can be supposed to contain at least 3 different quantum dots, becoming successively visible with varying detection energies. The two other spots (2, 3) also show a significant modulation in intensity.

A reference of the luminescence characteristics of the InAs/GaAs quantum dots is obtained by spectroscopy investigations with SNOM and μ -PL. The images Fig. 4.12 (a) and (b) show representative spectra of single quantum dots, taken with the SNOM in two different areas of the sample with an equal quantum dot density of approximately 10^8 cm^{-2} . The spectra are chosen out of series of measurements which were performed at 300 K with an uncoated fiber tip [108].

The spectra show distinct differences. In the spectrum shown in Fig. 4.12 (a),

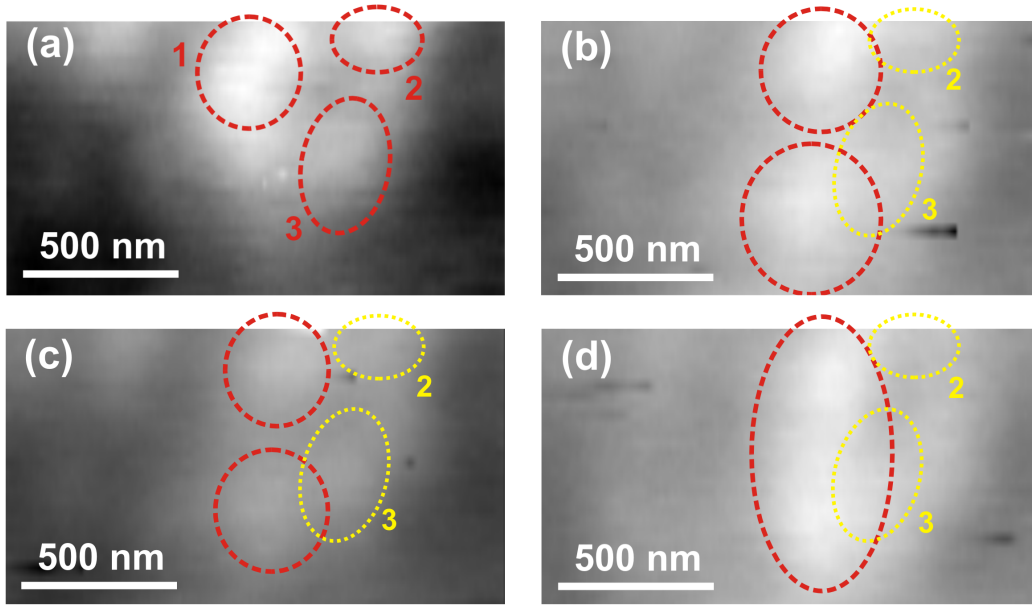


FIGURE 4.11: Luminescence scanning images of a group of InAs/GaAs quantum dots, taken at different detection energies of 1.008 eV (a), 1.004 eV (b), and 1.001 eV (c); (d) is taken at integrated luminescence.

an emission from the ground state and the first excited electron state of the quantum dot can be identified. At this temperature, the ground-state transition is found at a photon energy of 1.000 eV, showing a linewidth of 60 meV, and the first excited state in the region of 1.080 eV. In contrast, in the second area (Fig. 4.12 (b)), a clearly different luminescence profile is observed. Here, the peak of the ground state emission is found at a significantly higher energy of 1.050 eV, showing a linewidth of 75 meV, whilst an excited state cannot be identified clearly, even though the measurements were carried out at a comparable excitation intensity of nominally 20 mW. In general, this can be taken as an indication that the spectrum shown in Fig. 4.12 (b) originates from a small quantum dot, which does not allow the emergence of higher states. This interpretation corresponds to the increased energy of the ground state transition in comparison to the spectrum shown in Fig. 4.12 (a). Particularly remarkable is the large linewidth broadening of several tens of meV of the luminescence at room temperature (Fig. 4.12 (a), (b)). This feature is found to be typical for the quantum dots of this sample. Assuming that they originate from a thermally induced line broadening, these high values can be taken as an indication for an uncommonly large energy difference between the hole states in the quantum dots. For comparison, Fig. 4.12 (c) and Fig. 4.12 (d) show μ -PL spectra of the corresponding sample areas, taken at 10 K [144]. Two clearly differing luminescence profiles are observed, which correspond to the room temperature signals of single quantum dots (Fig. 4.12 (a), (b)). In the spectrum shown in Fig. 4.12 (c) the

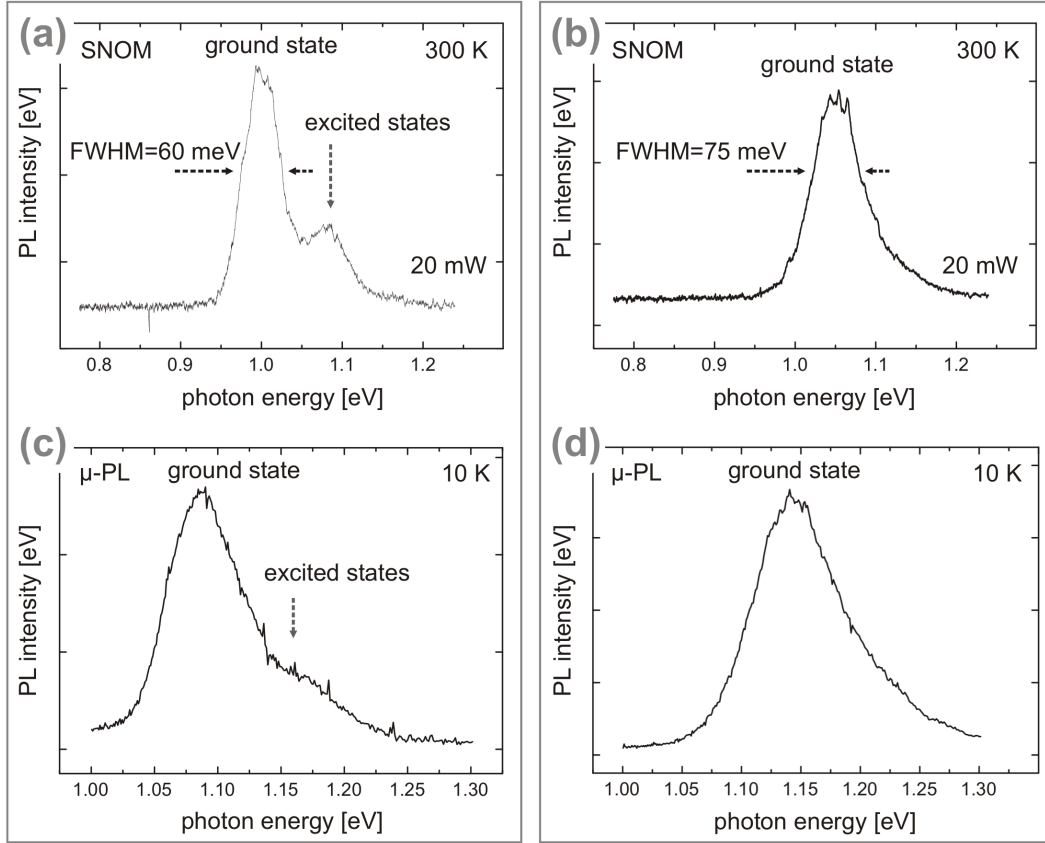


FIGURE 4.12: (a), (b) PL of single quantum dots from two different sample areas, taken at room temperature with the SNOM; (a) quantum dot shows emission from the ground state and the first excited state, (b) quantum dot shows emission only from the ground state, with different photon energy. (c), (d) ensemble μ -PL of the corresponding sample areas, taken at 10 K; different luminescence profiles are observed, being in accordance with (a) and (b).

peak emission is visible at a photon energy of 1.090 eV, which is accordingly assigned to the ground state transition at 10 K. Additionally, a tailing of the luminescence signal towards higher energies of the order of 1.150 eV indicates a population of the first excited states of the quantum dots in this sample area. In contrast, in the other sample area the peak emission from the ground state of the quantum dots is detected at a photon energy of 1.145 eV, while merely a weak tailing of the main signal towards higher photon energies is visible in Fig. 4.12 (d). This strengthens the assumption that in this area generally smaller quantum dots are present.

4.3 Low-temperature spectroscopy of individual quantum dots

4.3.1 InGaAs/GaAs quantum dots

Luminescence spectra of single InGaAs/GaAs quantum dots at 80 K

Figure 4.13 shows a series of spectra which are taken from a single InGaAs/GaAs quantum dot at 80 K [119]. In order to examine the luminescence of the ground

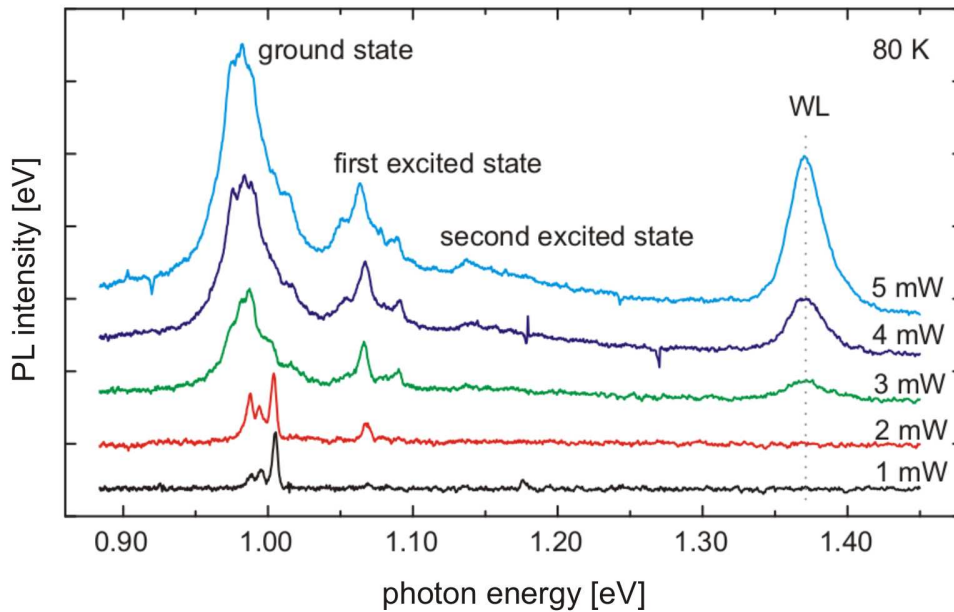


FIGURE 4.13: Photoluminescence spectra of a single InGaAs/GaAs quantum dot, obtained at 80 K under varying excitation intensities.

state of the quantum dot in detail, the excitation was performed at a low laser emission power of 1 – 5 mW. First it can be noticed that the spectra show a remarkably low level of noise for a low-temperature measurement of about 20 : 1 signal-to-noise ratio (SNR). The observed lines are well separated, which in principle allows a detailed analysis of the data in terms of their profile and intensity behavior. Accordingly, an assignment to specific transitions from different configurations of carriers is possible, assuming that the respective binding energies are larger than the observed thermal line broadening of 4 meV [107].

Since there is very few reliable information on the energies of the various configurations of carriers in comparable InGaAs/GaAs quantum dots with a ground state emission in the region of 1.000 eV, the identification of the observed peaks is based largely on a transfer of information upon quantum dots with a considerably higher ground-state energy [160]. For an analysis of the spectra in terms

of excitation-dependent line shifts a potential heating of the sample due to the increasing excitation power has to be regarded. As indicated in Fig. 4.13, the energy of the emission from the wetting layer (WL) is constant at 1.37 eV, which allows the ruling out of a thermally induced shift in the luminescence for this series of spectra.

Figure 4.14 (a), (b) shows the region between 0.950 eV and 1.030 eV at a large scale. The observed lines can be assigned to the ground state emission of the quantum dot. Figure 4.14 (a) shows an extension of the spectrum which is obtained at the lowest excitation intensity of 1 mW, Fig. 4.14 (b) shows the evolution of the signal with increasing excitation intensities. At lowest excitation intensity the appearance of initially 3 peaks can be noticed, which are labeled as L_1 , L_2 , and L_3 at 0.988 meV, 0.995 meV and 1.005 meV, respectively (Fig. 4.14 (a)). According to the theoretical considerations, these peaks can be assigned as follows: The peak L_3 , which shows highest luminescence intensity even at low excitation, should be assigned to a low-population state, i.e. either the neutral exciton (X) or a positive or negative trion (X^+/X^-), whereas the negative trion is improbable, because the signal of peak L_3 has a higher photon energy than both other peaks L_1 and L_2 . However, a definite decision concerning this issue cannot be made until the assignment of the other peaks is regarded. A comparison with measurements on other samples which have been grown under similar conditions, inclusive particularly a strong positive material doping, shows that the X^+ is typically antibinding [26]. Furthermore, in such samples very often the X^+ peak shows a higher intensity than the X peak even at low excitation, which is reasonable because the doping leads to a statistically enhanced population of the quantum dot with additional holes within the lifetime of the single exciton [100]. Moreover, the absolute value of the binding energy of the positive trion $E(X) - E(X^+)$ is reported to be generally larger than that of the biexciton $E(X) - E(XX)$ [26], which, regarding the energy differences in the spectra Fig. 4.14 (a), additionally supports the assignment to the positive trion.

Starting from this point, an assumption can be made for the peaks L_1 and L_2 , with respect to the variation of the spectra under increasing excitation density, as shown in Fig. 4.14 (b). As it can be seen in Fig. 4.13, an emission from the first excited electron state sets in at an excitation intensity of 2 mW. This roughly indicates the threshold where the ground state is fully populated on average, i.e. a luminescence behavior that is due to a varying ground-state population has to be observed at lower excitation.

With respect to the binding energies that can be expected, an assignment of peak L_2 to the single exciton X seems plausible, which would demand that peak L_1 is ascribed to a biexciton recombination. This is supported by the intensity behavior of the peaks: whilst peak L_2 is initially slightly stronger than peak L_1 , it is exceeded by the latter with increasing excitation, parallel to the appearance of the first excited state (Fig. 4.13). Quantitatively, the supposed biexciton peak L_1 should show a quadratic increase, while the single exciton rises linearly [186].

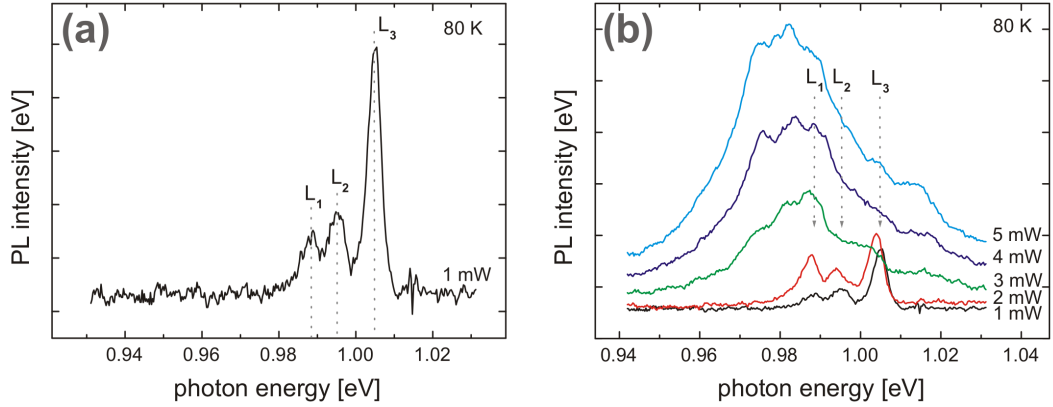


FIGURE 4.14: Photoluminescence of the ground state of a single InGaAs/GaAs quantum dot; (a) 3 lines are observed at an excitation intensity of 1 mW; (b) variation of the spectra with increasing excitation intensities.

For a quantum dot that is supposed to be charged because of background doping, the intensities of the sum of the neutral and the charged configuration have to be compared. In the given case, regarding the strength of the positive trion (X^+) emission, it seems likely that the investigated quantum dot has a particularly strong attraction to positive charges. Thus a high probability for a formation of positively charged biexcitons (XX^+) is expected, which should give rise to a corresponding emission signal. However, this is missing in the spectra, according to the given assignment. Furthermore, it can be noticed in Fig. 4.14 (b) that, up to an excitation intensity of 2 mW the supposed trion peak L_3 is stronger than both peaks L_1 and L_2 . This behavior is unlikely, provided that the given assignment of the peak L_3 is correct. Indeed, a thorough analysis of the peak behavior requires a statistical examination based on a more comprehensive database. In principle a fitting of the luminescence peaks with appropriately chosen Voigt profiles is also required for a precise determination of their intensity. However, this were reasonably practicable only for the spectrum taken at an excitation intensity of 1 mW (Fig. 4.14 (a)), which shows a sufficient separation of the peaks [100]. For these reasons the interpretation of the spectra remains largely speculative, and a number of alternative assignments must be considered possible. Regarding for instance the reported low values for the binding energy of the neutral biexciton XX [26], the focus may be put on the suggestion that the peak L_2 may actually cover two different emission signals, which could be assigned to the single exciton X and the neutral biexciton XX . Indeed, arguing that the peak L_2 shows a minute shift of its balance point between an excitation intensity of 1 mW and 2 mW (Fig. 4.14 (b)), an appearance of further emission signals at low excitation intensities can be suggested, which might be assigned to the missed positive biexciton (XX^+).

According to Fig. 4.14 (a), the energy of the single exciton X (L_2) can be an-

nounced as 0.995 eV, and the energy of the biexciton XX as 0.988 eV. This yields a positive binding energy of the biexciton of 7 meV, and a value of -10 meV for the binding energy of the positively charged exciton X^+ .

Unfortunately, the limited spectral resolution does not provide more detailed information, which is partly owing to the thermal line broadening at 80 K. So the suggested shift of the balance point of peak L_2 may well be caused by a background fluctuation, and vice versa, the peaks L_1 and L_3 may likewise cover emission signals from different transitions within the quantum dot, which cannot be discriminated clearly in this measurement. The limited number of spectra adds to this problem, because it impedes a detailed observation of the intensity behavior at variations of the excitation intensity in small steps.

A reference can be obtained from a comparison to spectra from other quantum dots within this sample, as is shown, e.g., in Fig. 4.15 [107]. The ground state region of this quantum dot is shown in more detail in Fig. 4.16. At low excitation

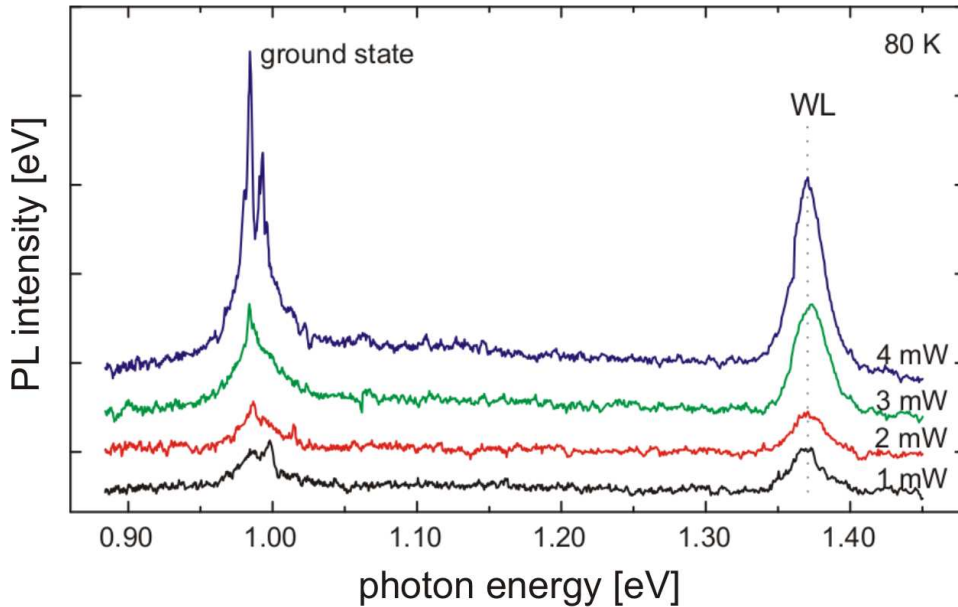


FIGURE 4.15: Photoluminescence spectra of a single InGaAs/GaAs quantum dot, obtained at 80 K under varying excitation intensities.

intensities between 1 mW and 3 mW, 3 different peaks are found, which are labeled as L_1 , at a photon energy of 0.984 eV, L_2 at 0.986 eV, and L_3 at 0.998 eV, respectively. They are separated by about 2 meV (L_2-L_1) and 12 meV (L_3-L_2), showing a similar intensity behavior as like the peaks L_1 , L_2 and L_3 observed in the firstly presented measurement (Fig. 4.13). The pattern is characterized by an initial appearance of the peak L_3 at the highest photon energy, followed by a successive rise of the peaks L_2 and L_1 , while L_3 is decreasing in amplitude.

With an analogous interpretation, the peaks L_1 , L_2 , and L_3 in the measurement

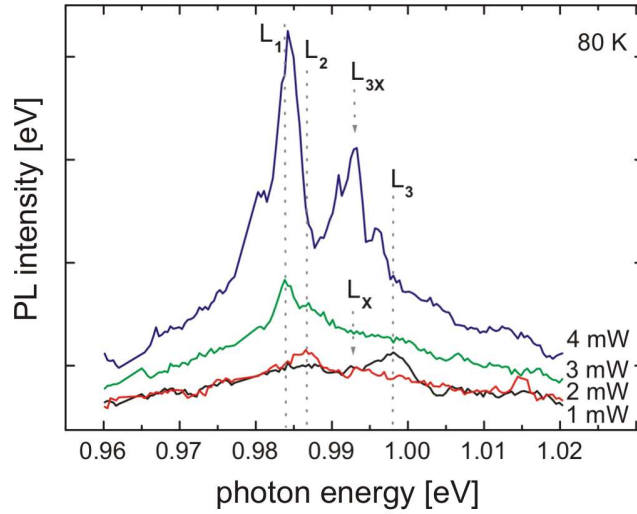


FIGURE 4.16: Photoluminescence spectra showing the emission from the ground state of a single InGaAs/GaAs quantum dot; new peaks appear at increasing excitation intensities.

shown in Fig. 4.15 may represent emission signals from a biexciton state (XX), a single exciton (X), and a positive trion (X^+). Correspondingly, the positive binding energy of the biexciton is given as 2 meV, and the absolute value of the negative binding energy of the positively charged exciton is 12 meV. Unfortunately, the measurement suffers from a strong background noise, which makes an assignment even more vague than for the previously shown series of spectra (Fig. 4.13). Again, it has to be taken into consideration that the thermally induced linewidth broadening of 4 meV may cover groups of different emission signals which cannot be resolved clearly. Therefore also in this measurement, an alternative assignment is possible, e.g., with peak L_2 stemming from the neutral biexciton (XX), while peak L_1 can be assigned to the positively-charged biexciton (XX^+). In this case, the emission from the neutral exciton (X) should be found in between the energies of the biexciton of 0.986 eV and the supposed positive trion (X^+) of 0.998 eV, according to theoretical considerations.

It might be represented, e.g., by the small shoulder L_X which can be perceived to appearing at a photon energy of 0.993 eV in the spectrum taken under an excitation intensity of 1 mW (Fig. 4.16). Another remarkable feature in this series of spectra is the appearance of a strong signal at a photon energy of 0.993 eV under a high excitation intensity of 4 mW, which is indicated by L_{3X} in Fig. 4.16. This peak L_{3X} appears at the threshold to the population of the first excited state, whose emergence is shown in more detail in Fig. 4.17. As is visible, at increasing excitation intensities of 4 – 5 mW, first the peak L_1 gains intensity, before the peak L_{3X} is rising, parallel to the appearance of the signal from the first excited (electron) state at a photon energy of about 1.078 eV. This behavior is, most

probably, an indication of the formation of a carrier complex, such as a biexciton. Therefore, again, an alternative interpretation of the spectra seems evident, with the peak L_1 representing the single exciton state, while the peak L_{3X} is to be assigned to the biexciton. This model were fitting also the assignment of peak L_3 to the positive trion (X^+) given above (Fig. 4.16), leading to a value of the negative binding energy of -14 meV. In this case, also the biexciton were antibinding, showing a binding energy of -9 meV. However, such an assignment conflicts

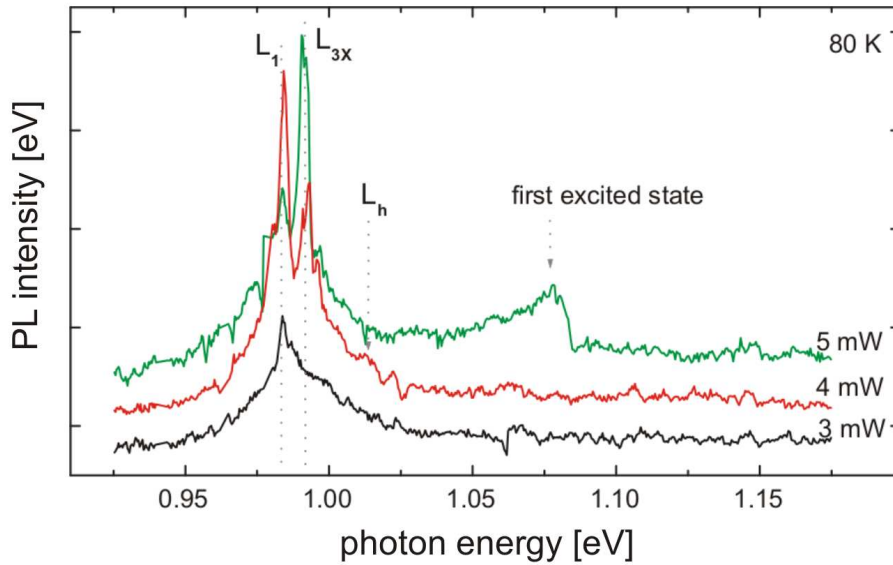


FIGURE 4.17: Photoluminescence spectra of single InGaAs/GaAs quantum dot; an emission from the first excited state appear at an excitation intensity of 5 mW.

with the observation that the biexciton state in InGaAs/GaAs is reported to be generally a binding state [26].

Some further information about the investigated quantum dots can be derived from an examination of the excited states. As visible in Fig. 4.13, for the investigated quantum dot an emission signal appears at a higher photon energy in between 1.050 eV and 1.100 eV, parallel to the rise of peak L_1 , which indicates a population of the first excited electron state. The signal from the ground state, the first and the second excited electron state of this quantum dot are shown in more detail in Fig. 4.18. A pattern of 3 peaks is observed to be appearing in the region of the first excited electron state, which are labeled as L_{I-1} , at a photon energy of about 1.050 eV, L_{I-2} at 1.068 eV and L_{I-3} at 1.089 eV. At a photon energy of about 1.136 eV a PL signal observed at high excitation intensities of 4 – 5 mW, which can be assigned to the second excited state (L_{II}). The first peak out of these to become apparent with increasing excitation intensities is L_{I-2} . This peak can be supposed to show the basically first excited state, which

is given by the recombination of an electron-hole pair out of the lowest energy configuration of 3 pairs of carriers within a quantum dot (XXX). Accordingly, with the given assignment for the emission of the single exciton to L_2 at 0.995 eV, the energy difference to the ground state can be determined as 73 meV for this quantum dot.

To determine the energy of the unmixed state, in principle the recombination of a single pair of carriers between the pure first excited electron state e_1 and the basic hole state h_0 has to be observed. However, this is extremely improbable according to the selection rules for a radiative transition, because both the first excited electron state and the hole ground state in a quantum dot are of p-state character, with a quantum mechanical angular momentum of $J = 1$ [122]. Since also the population statistics is opposing such a carrier configuration, a corresponding emission can hardly be observed with time-integrated spectroscopy. However, the observation of a transition between the s-like electron ground state (e_0) with an angular momentum of $J = 0$, and the p-like first excited hole state (h_1) is more probable, and provides some information which can be used for a better approximation [100]. According to theory, the distance of the hole states is of the order of a few meV, which corresponds to the observed thermal line broadening for the quantum dot luminescence of this sample [28, 29, 107]. Correspondingly, the emission from the $e_0 - h_1$ recombination can be expected to appear in a luminescence spectrum several meV higher than the single exciton signal. Regarding the energy difference to the supposed X peak, the peak L_h which is appearing at a photon energy of 1.017 eV in the spectrum taken at 3 mW excitation intensity (Fig. 4.18) is a candidate for such a transition. However, the signal is superimposed by a background, which may originate from interactions of carrier complexes within the quantum dot or from a scattering with free carriers floating in the bulk material, according to the measurement temperature of 80 K [100]. With respect to this, the proper energy difference of the first excited state to the ground state can be calculated as approximately $\Delta E_{e_0-e_1} = E_{XXX} - E_X - (E_{h_1} - E_X) = E_{L_{I-2}} - E_{L_h} = 51$ meV, with the distance between the hole ground state and the first excited hole state being determined as $\Delta E_{h_0-h_1} = E_{h_1} - E_X$. An analogous consideration can be made for the spectra taken from the second quantum dot (Fig. 4.17). Due to the unclear assignment of the peaks and the increased background noise, in this case only to a rough estimation is possible for the energy difference between the ground state and the first excited state, suggesting a value between 70 – 100 meV. However, it has to be kept in mind in any case that the calculation does not give the distance between the pure single-carrier states, since it is derived from an interaction of two confined carriers, even though for the first quantum dot (Fig. 4.18) the error is assumed to be rather small, in comparison to the measurement uncertainty that is given by the obtained linewidth.

As visible in Fig. 4.18 and Fig. 4.17, at higher excitation intensities the ground

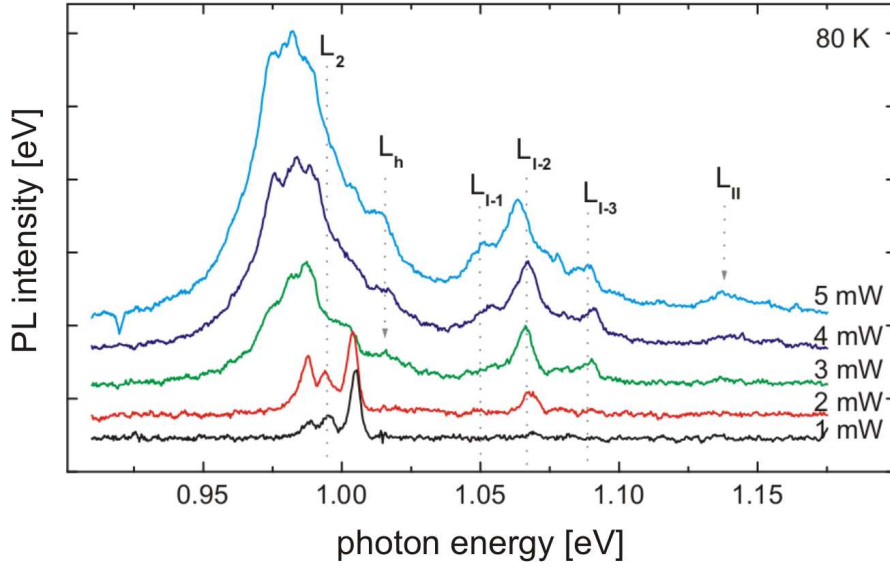


FIGURE 4.18: Photoluminescence spectra of a single InGaAs/GaAs quantum dot at varied excitation intensities; emission signals from the first and the second excited state appear at increasing excitation intensities.

state emission of both investigated InGaAs/GaAs quantum dots show a number of additional peaks, leading to a general broadening and a complex emission profile. In addition, the signal from the first excited state shows a complex profile at increased excitation intensity. According to theory, this is owing to the formation of few-particle complexes from the carriers accumulating within the quantum dot, leading to further energy shifts [168].

It is also interesting to note in this regard that, for the first quantum dot a strong peak L_{I-1} appears at a photon energy of 1.050 eV (Fig. 4.18). Furthermore, the peak L_{I-3} becomes observable at 1.089 eV, rising in parallel to the signal L_{II} of the second excited electron state. Provided that the energy difference $\Delta E_{h_1-h_2}$ of the hole states h_1 and h_2 can be assumed to be comparable to $\Delta E_{h_0-h_1}$, the peak L_{I-3} can be related to an $e_1 - h_2$ transition, which corresponds to the observed energy difference of L_h to L_2 ($e_0 - h_1$ transition). In such a view, the peak L_{I-1} is associated with an $e_1 - h_0$ recombination, since it shows a corresponding distance to the peak L_{I-2} , taking into account particularly that the latter shows a shift of about 4 meV towards a lower photon energy with increasing excitation (Fig. 4.18). This behavior can also be explained by few-carrier interactions. As already mentioned, however, such a transition is highly improbable. On the other hand, as is revealed by a first shot at this sample at a temperature of 4 K, the first-excited state emission is composed of a large number of closely adjoining lines. At a temperature of 80 K, this ensemble of lines shows up as a broadened luminescence pattern, which is superimposed further with a background from

free-carrier scattering processes. Thus, even though a number of peaks are pronounced in the presented spectra, a definite assignment cannot be given here, due to the limited resolution and the complexity of the configuration.

Interestingly, the signal from the excited electron state does not appear in the spectra taken from the second quantum dot up to an excitation intensity of 4 mW, as visible in Fig. 4.17, while the lineshift behavior of the ground-state emission is entirely evolving below this excitation intensity (Fig. 4.15). This indicates a different electronic structure in this quantum dot, which should be associated with correspondingly different structural properties. On the other hand, the strong signal from the ground state transitions, as well as the peak of the first excited electron state are detected at comparable energies as those found in the first series of spectra (Fig. 4.13), which is an indication for a comparable structure of the quantum dots. In addition, the small shoulder L_h which appears at a photon energy of about 1.014 eV under an excitation intensity of 4 mW (Fig. 4.17) may be due to an $e_0 - h_1$ recombination. In this measurement, the peak L_1 at a photon energy of 0.984 eV is assigned to the recombination out of the biexciton state, as discussed above (Fig. 4.15). However, there is no systematic dependence of the biexciton binding energy on a corresponding single exciton energy found for InGaAs/GaAs quantum dots, apart from the observation that the biexciton state is always a binding state [26]. Insofar as these findings can be transferred to the sample that is investigated in this work, the biexciton binding energy must apparently be accepted to vary unsystematically by several meV. Therefore, the position of the biexciton peak provides no further information for a discussion of the structural properties of the investigated quantum dots.

On the other hand, the different behavior of the ground state peaks of the quantum dots with increasing excitation intensities can be the result of a significantly different stoichiometry distribution, a different charging, or an inhomogeneous exposition to external fields. The first is unlikely, with reference to structural investigations on comparable samples which show a well-reproducible formation of InGaAs/GaAs quantum dots with a characteristic stoichiometric profile of a reversed truncated cone [154]. By contrast, there are two major indications for a different electronic charging, or for a different exposition to external fields of the investigated quantum dots. Firstly, the different emission behavior observed in the two measurements can generally be understood as reflecting a difference in the population statistics of the quantum dots. Accordingly the observation that the intensity of the supposed positive-trion (X^+) signal is significantly different indicates a different attractivity of the quantum dots to positive charges. Secondly, in the spectra shown in Fig. 4.15, a strong signal from the wetting layer is obtained despite a low population of the quantum dot with carriers, which can be interpreted as an indication for a different attractivity of the quantum dot to carriers.

In conclusion, the quantum dots investigated within the scope of this work show a rough consistency regarding the scale of the binding energies of the biexci-

ton and a supposed positive trion, which allows the assumption of a congruent atomic structure. By contrast, the quantum dots appear to be significantly different in terms of specific electronic properties, in particular of their attractivity to carriers, which can be explained by the influence of a different charging or electronic environment. So far, however, only a small quantity of data on individual quantum dots at low temperatures was obtained, which provide merely a first impression of the properties of the system. For an exhaustive analysis more photoluminescence data, also at lower temperatures, are required, as well as detailed information on the structural parameters of the investigated system.

4.3.2 InAs/GaAs quantum dots

Luminescence spectra of single InAs/GaAs quantum dots at 5 K

The operation of the new low-temperature SNOM was tested in investigating the photoluminescence of InAs/GaAs quantum dots at a temperature of 5 K. Figures 4.19 (a) and (b) show an example spectrum that was taken from a single quantum dot. Figure 4.19 (b) shows the region of the quantum dot ground state emission at larger scale, revealing a spectral resolution of 1.5 meV. The

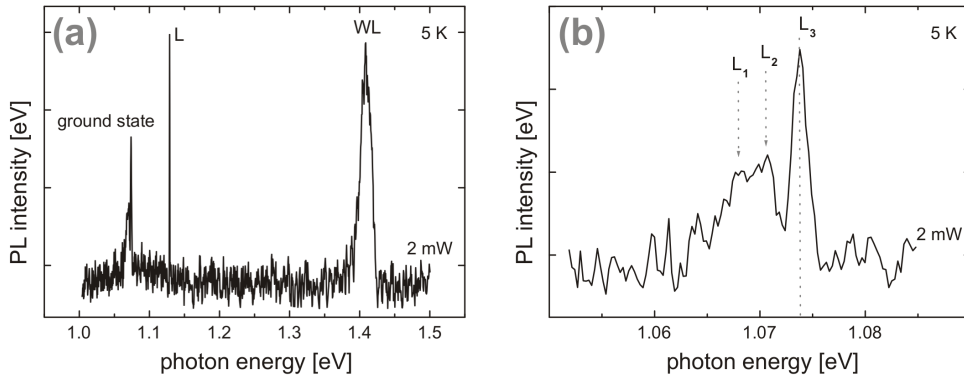


FIGURE 4.19: Photoluminescence of a single InAs/GaAs quantum dot, taken at 5 K; (a) an emission signal from the ground state is observed in between 1.050 eV and 1.080 eV; (b) in the extension, at least 3 peaks can be identified in the ground state.

emission from the wetting layer (*WL*) appears at 1.408 eV peak photon energy (Fig. 4.19 (a)). A luminescence signal is detected in between 1.050 eV and 1.080 eV which is assigned to the ground state of the quantum dot, as well as a single peak L_{μ} at 1.128 eV which can be ascribed to the impact from a cosmic particle in the detector. According to the applied low excitation intensity of nominally 2 mW laser emission power, there are no emission signals from higher states appearing.

An analysis of the emission profile shows that the observed pattern may contain at least 3 separate peaks, which are labeled as L_1 , at about 1.068 eV, L_2 at

1.071 eV, and L_3 at 1.074 eV Fig. 4.19 (b). A first assignment of the peaks to electronic transitions within the quantum dot can be given with respect to their positions and their relative intensity, which reveal a similar pattern than the characteristic spectra obtained from comparable InAs/GaAs quantum dots with higher ground state energies [26]. In this way, the peaks L_1 and L_2 in the spectrum (Fig. 4.19 (b)) can be assigned to recombinations from the single exciton state X (L_1) and the biexciton state XX (L_2), while the peak L_3 may originate from a positively-charged single exciton X^+ . This assignment corresponds to the interpretation given for the cathodoluminescence spectrum shown in Fig. 4.4, which had been obtained from a comparable InAs/GaAs quantum dot sample. However, the difference of the ground-state energies of the compared quantum dots of 300 meV corresponds to a considerably differing size, and potentially also a diverging atomic structure of the investigated quantum dot, thus probably leading to different electronic properties. This suggests a different assignment of the observed peaks in Fig. 4.19 (b), which in particular comprises an interchange between L_1 and L_2 , i.e. an assignment of the peak L_1 to the biexciton state (XX), and of the peak L_2 to the single exciton (X). In this case, the peak L_3 may still belong to the positively-charged exciton (X^+), assuming that the interchange would result in a correspondingly lessened strength of the repulsive effect of this complex. The positive binding energy of the biexciton then is determined to be 3 meV, and also is the negative binding energy of the trion found to be -3 meV. This interpretation is based on the assumption that the investigated quantum dot has a strong attractivity for positive carriers, which is reasonable regarding the strong background doping of the sample [100, 144]. However, if the quantum dot is not charged a priori, an alternative assignment can be considered, with the peak L_3 representing a single exciton recombination which is strong because of the low excitation intensity, and the weaker peaks L_1 and L_2 originating from binding few-carrier configurations, such as the biexciton or the trion state.

For a more detailed analysis, the characteristic behavior of the luminescence of the quantum dots within this sample is investigated under varied excitation intensities. Figure 4.20 shows a short series of spectra from another quantum dot, which are obtained at 5 K. The spectra are taken at relatively low excitation intensities, thus revealing the successive population of the ground state in detail. At the lowest excitation intensity of nominally 1 mW, a pattern of at least 3 peaks is visible in the region of the quantum dot ground state, which resembles that observed in the spectrum shown by Fig. 4.19 (b). The emission is dominated by a strong peak at a photon energy of 1.075 eV, accompanied by a broadened feature at a slightly lower photon energy, which may consist of at least 2 separate peaks of approximately equal intensity. With increasing excitation intensity the emission generally gains strength, and a number of additional peaks appear which are clearly visible at maximum excitation intensity. The pattern is pointed out by a multiple-line fit of the emission profile, shown in Fig. 4.21. A number of at least 5 peaks can be identified, which are labeled as L_1 appearing at a photon

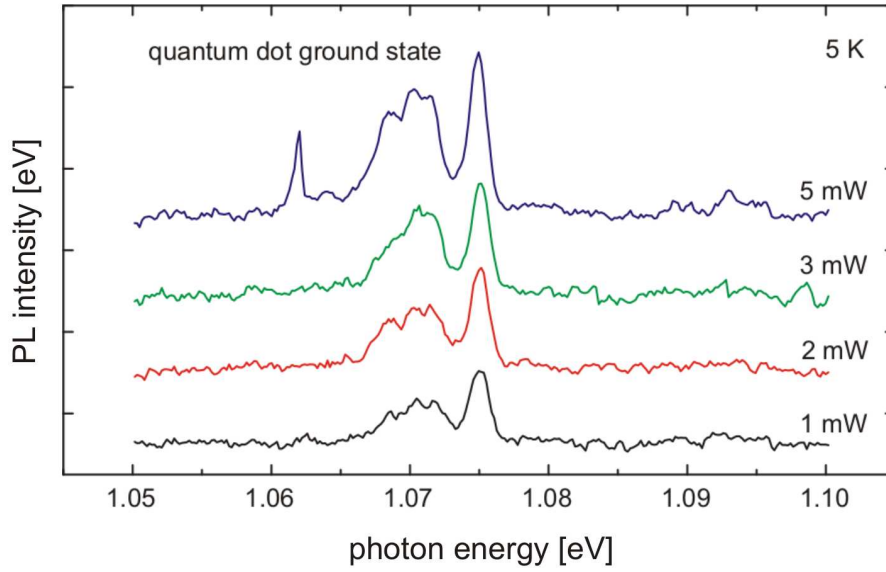


FIGURE 4.20: Photoluminescence spectra of a single InAs/GaAs quantum dot, showing the appearance of additional peaks in the region of the ground state with increasing excitation intensities.

energy of 1.056 eV, L_2 at 1.062 eV, L_3 at 1.064 eV, L_4 at 1.065 eV, and L_5 at 1.068 eV. Following a reasoning analogous to [26], the peak L_5 has to be assigned to a low-population state, as a single exciton (X) or a positive trion (X^+) which is strong even at low excitation. A comparison with the reference data shown in Fig. 4.1.5 basically suggests an assignment of the peak L_5 to a positive trion (X^+), which is the highest ground state transition in terms of photon energy. Another, particularly serious indication for this suggestion is the relative strength of L_5 , which is analogous to observations made at other quantum dots with a high positive background doping [100]. According to the propositions made in chapter (4.1.5) for the other peaks an ordering can be given as follows.

The next transition at a lower photon energy than the positive trion is the single exciton (X), which accordingly will be represented by the peak L_4 , followed by the positively-charged biexciton (XX^+) showing up either with the peak L_3 , or with L_2 . The neutral biexciton (XX) displays the largest, positive binding energy, thus it will be represented by the peak L_1 . With this hypothesis, for the positive trion (X^+), a negative binding energy of -3 meV can be determined. The neutral biexciton (XX) will have a positive binding energy of 11 meV, and its positively charged associate (XX^+) a binding energy between $1 - 3$ meV, depending on the assignment of the peaks.

An obvious problem with this model is that, according to the systematics shown in Fig. 4.1.5, the positively-charged exciton (X^+) should rather display a very small, or even a positive binding energy. Additionally, the broadened peak between 1.059 eV and 1.066 eV in Fig. 4.21 contains at least 3 peaks which have to

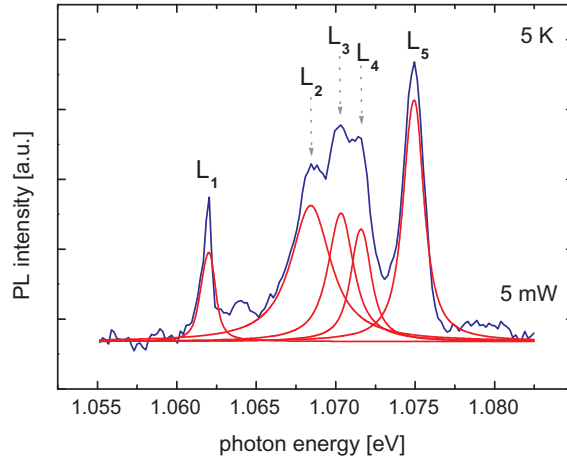


FIGURE 4.21: Pattern of the ground-state PL of InAs/GaAs quantum dot.

be assigned to different transitions. Furthermore, also the binding energy of the positively charged biexciton (XX^+) is expected to be rather low, and the energy difference between the neutral biexciton and the positively-charged biexciton is expected to be approximately 3 – 4 eV, quantitatively. Regarding these issues, here an alternative assignment is favored. This is given by the suggestion that the single exciton X is represented by the peak L_4 , the positively charged biexciton XX^+ by L_3 , and the neutral biexciton XX by L_2 , postponing at first the assignment of the peak L_1 . With respect to the general uncertainty associated with the extrapolation shown in Fig. 4.1.5, the preeminent strength of the peak L_5 is given more weight than the presumed transition energy of the positive trion (X^+). Therefore, the peak L_5 is again assigned to the positive trion (X^+), which hence will remain to be antibinding, with a binding energy of -3 meV, whilst the (positive) binding energy of the neutral biexciton (XX) is 4 meV, and that of the positively-charged biexciton (XX^+) has to be given as 1 meV.

A question remains about the transition represented by the peak L_1 at high excitation intensities. One explanation, namely that the low-energy peak L_1 is due to a recombination from higher electronic complexes, is unlikely for the present quantum dot, since there is no emission signal observed from an excited state emission in the spectra of this quantum dot, as is demonstrated by Fig. 4.22 (a). According to the ensemble measurements, for the majority of quantum dots within this sample, the energy difference between the ground state and the first excited electron state is of the order of 50 – 100 meV, with a mean value of 75 meV³. Thus, a signal from an excited electron state should be showing up at a photon energy of the order of 1.150 eV. Another candidate for the peak

³It has to be kept in mind that the distribution is not necessarily Gaussian.

L_1 is the negatively-charged exciton (X^-), which appears at the lowest energetic position in the systematics proposed in [26] (Fig. 4.1.5), even for quantum dots with a very low ground state transition energy. However, a formation of negative trions in the quantum dots should be highly improbable, regarding the strong background doping improbable the investigated sample. Moreover, the relative strength of the signal is in contrast to corresponding observations [26, 100]. Other possible explanations for the observed line L_1 might be, that it shows either a spectral diffusion effect induced by the influence of external fields, or the appearance of a signal from a neighboring quantum dot. The latter is not very likely, because the quantum dot density was low at the position of the measurement. Nevertheless, it cannot be ruled out completely, since the spectrum was taken at the end of a series of measurements, and may thus already have suffered from a slight lateral drift. Unfortunately, the position of the tip could not be controlled afterwards in this case, due to loss of the nearfield contact.

Another remarkable feature of this measurement is the peak L_6 at about 1.094 eV peak photon energy, which appears at relatively high excitation intensities of more than 3 mW, as is shown in Fig. 4.22 (a). This position is by and large still in the region of the ground-state, and an assignment to an excited electron state is highly inappropriate. A more plausible explanation for the peak L_6 is, that it originates from an $e_0 - h_1$ recombination. Taking a broader look, there are up to 5 peaks observable in the region, despite a relatively high level of background noise, as is highlighted in Fig. 4.22 (b). These spikes can be distinguished from a thermal effect, or a scattering on free carriers as there was suggested for the measurements on InGaAs/GaAs quantum dots at 80 K, since those effects are almost completely suppressed at a temperature of 5 K. Insofar as they are not mere background fluctuations, an interpretation of these peaks as originating from recombinations of ground state electrons with excited holes from different

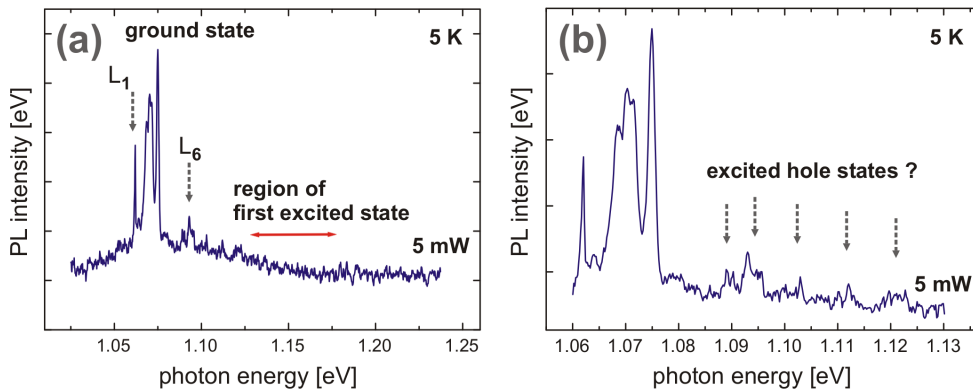


FIGURE 4.22: Photoluminescence of a single InAs/GaAs quantum dot; (a) under high excitation intensity, an additional peak appears at about 1.094 eV peak photon energy; (b) a detailed view reveals the appearance of up to 5 extra peaks in the region.

hole states h_1, h_2, \dots may be considered. Interestingly, the energy difference between the electron ground-state and the region of these supposed excited hole states corresponds to the large line broadening of about 50 meV in the ground state emission, which is observed in room-temperature measurements on single quantum dots. This corresponds to the hypothesis that an exceptionally wide spreading of the hole states might be a specific property of the InAs/GaAs quantum dots within the investigated sample.

As a reference, a short series of spectra was taken from another quantum dot. In order to take a closer look at the evolution of the low-population states, the excitation intensity was varied by a very low range of 0.5 mW to 1.5 mW in this measurement. The obtained spectra are shown in Fig. 4.23 (a), (b). An emission signal from the quantum dot ground state can be observed in between 1.085 eV and 1.105 eV, which is shown in more detail in Fig. 4.23 (b). However, the data are suffering from a considerable background noise because of the weak emission intensity, which makes the analysis difficult. In particular at the lowest excitation intensity of 0.5 mW, a luminescence signal cannot be distinguished clearly from the baseline. Nevertheless, even though the identification of the peaks is partly dimmish, some observations can be made in the spectra taken at slightly increased excitation intensities.

A pattern of 3 peaks appears at an excitation intensity of 1.0 mW, which are labeled L_1 , L_2 and L_3 in Fig. 4.23 (b): a pronounced peak L_3 is found at the highest energy position of 1.103 eV, being accompanied by two other peaks L_1 and L_2 at lower energies of 1.092 eV (L_1) and 1.097 eV (L_2). Interestingly, the pattern is changed significantly at an enhanced excitation intensity of 1.5 mW, differently from the previously presented measurement (Fig. 4.23 (b)). In the present case, the peak L_3 disappears with the increase in excitation intensity, while the peak L_2 increases in strength. In parallel, a new peak L_{ii} can be perceived to be appearing in between L_1 and L_2 , at a photon energy of 1.094 eV, leading to a broadening of L_2 . Furthermore, the appearance of a more separated, small peak L_i at a photon energy of 1.088 eV can be observed.

As a result, the pattern observed at an excitation intensity of 1 mW resembles the one which was obtained in the previously shown measurement at a considerably higher excitation intensity of 5 mW (Fig. 4.21). The major difference between both is that in the present case, the peak L_3 at the highest photon energy is disappearing at increased excitation intensity. In an analogous way, the peak L_3 might be assigned to a single exciton, or a trion recombination as well, because of its appearance at very low excitation intensities. Here the assignment to the single exciton (X) is preferable according to the intensity behavior of the signal. This leads to the suggestion that the investigated quantum dot has no particular attraction to single carriers. Accordingly it can be assumed that the probability for a formation of charged carrier complexes is rather low. The peak L_2 or L_{ii} can then be assigned to a recombination out of the biexciton state, and a positive

biexciton binding energy of 6 meV or 9 meV is found, respectively. However, in this case the origin of the other peaks remains unexplained. Therefore, another interpretation is favored here. Considering particularly the uncertainty that is associated with the measurement, the features L_1 , L_2 and L_3 which are observed at an excitation intensity of 1.0 mW are valued as being mere background fluctuations, just as like the small peak L_i , and the focus is put on the peaks L_{ii} and L_2 which are detected definitely. According to the propositions made in chapter 4.1.5, these peaks have to be assigned to the recombination of the single exciton (X) and the biexciton (XX). The peak L_2 is to be assigned to the single exciton, and L_{ii} to the biexciton state. Using this model, a positive binding

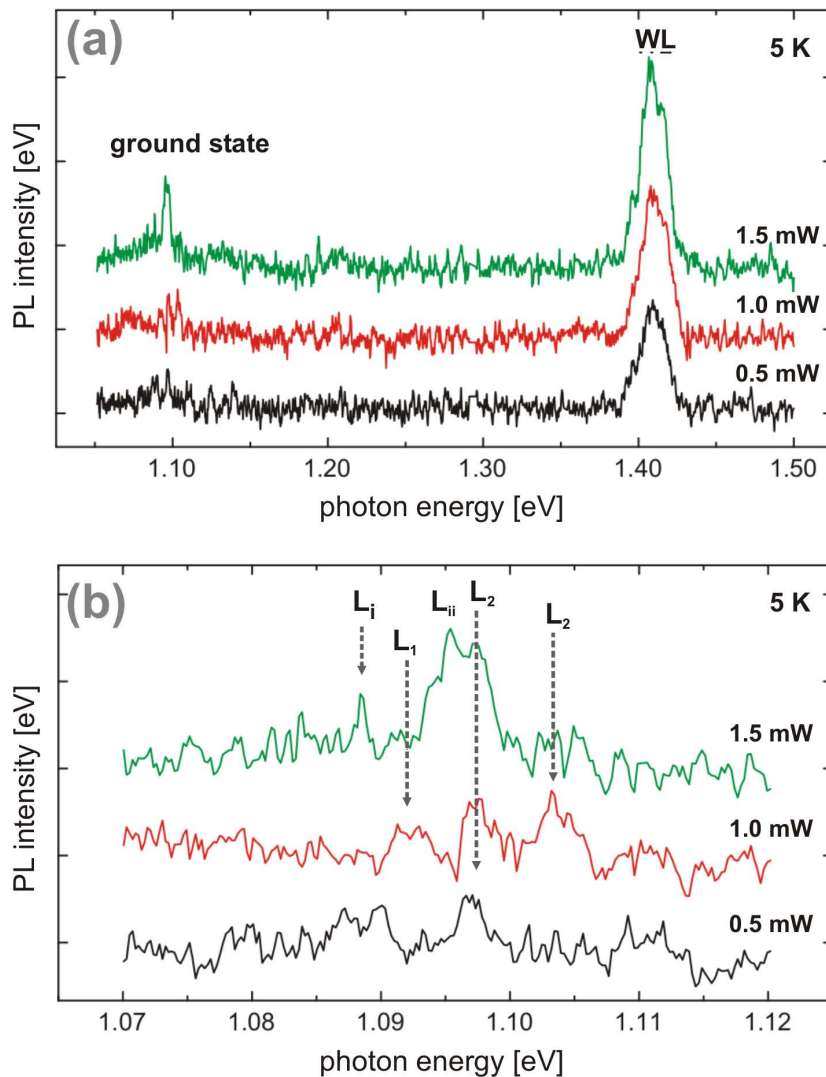


FIGURE 4.23: (a) Photoluminescence spectra of a single InAs/GaAs quantum dot at low, varied excitation intensities; (b) extension of the region of the ground state.

energy of 3 meV can be determined for the neutral biexciton in this quantum dot. Unfortunately, a more detailed assessing of the photoluminescence signal is not possible in this measurement, due to the low signal intensity and the limited number of spectra.

For reference, several singular and doubled spectra are consulted further, which were taken from different quantum dots at different excitation intensities. This practice is chosen as a makeshift way to bypass the difficulty of obtaining extended series of spectra at low temperatures. In these measurements, at comparable excitation conditions a majority of approx. 85% of the investigated InAs/GaAs quantum dots from different sample areas show the known characteristic pattern of the ground state emission, which consists of 3 or 4 neighboring peaks, with a pronounced emission at the highest photon energy, and 2 or 3 peaks close-by at lower energies, showing less signal intensity. According to the given propositions, these peaks are assigned in general to a positively charged trion (X^+), being represented by the pronounced peak at the highest photon energy, and to the single exciton (X) and the biexciton (XX), showing up with the accompanying features at lower photon energies. This way, at average a positive binding energy of 1 – 3 meV is determined for the biexciton, and a generally negative binding energy of about -3 meV is fixed for the positively-charged trion.

By way of example, Fig. 4.24 shows two singular spectra which are obtained from two different quantum dots at the same excitation intensity of nominally 2 mW, focussing on the ground-state region of the quantum dot luminescence. Both spectra show the characteristic pattern of peaks, despite the general difference of about 11 meV of the photon energies of their ground-state emissions.

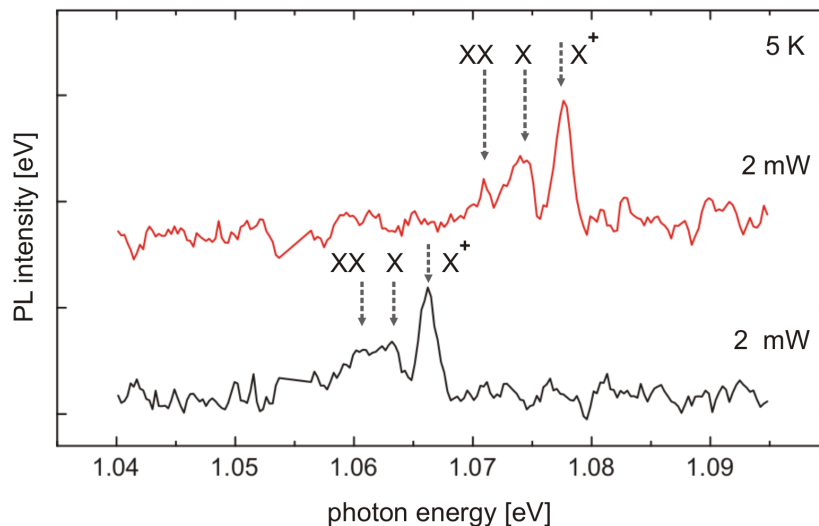


FIGURE 4.24: Singular photoluminescence spectra from two different InAs/GaAs quantum dots, showing the characteristic pattern of the ground state emission.

For the quantum dot which is represented by the lower spectrum (black curve), showing a recombination energy of the single exciton (X) of 1.063 eV, a value of equally ± 3 meV is determined for the binding energy of the (binding) biexciton and for the (antibinding) trion. For the other quantum dot (red curve) with a higher single exciton recombination energy of 1.074 eV, a binding energy of equally ± 4 meV is found for the biexciton (binding) and for the positively-charged exciton (antibinding).

The strategy of comparing numbers of singular or doubled spectra from different quantum dots is also used to obtain more information upon the typical luminescence signature of quantum dots at higher excitation intensities. Figures 4.25 (a) and (b) show 2 pairs of spectra, taken from 2 different quantum dots. The data were obtained at increased excitation intensities in a range of 4 – 12 mW. As visible in Fig. 4.25 (a), the characteristic pattern of the ground state emission can be observed for this quantum dot at a low excitation intensity of 4 mW, as well as at 12 mW, being indicated plainly by L_i , $L_{1,2}$ and L_3 . At increased excitation, additionally, a number of peaks become visible at various higher-energy positions, which can be supposed to originate from excited electron states. Such are, the feature L_I at a photon energy of 1.174 eV, and the feature L_{II} at about 1.243 eV.

Interestingly, neither of these features actually matches the expected spectral position for the respective excited state. If they are assigned to the first and the second excited electron state, respectively, their extraordinarily large energy differences to the ground state suggest an extremely small quantum dot. On the other hand, the position of the ground state signal at about 1.100 eV photon energy is well within the expected region, thus suggesting a common size and structure of the quantum dots. Similarly ambivalent observations are made for the measurement shown in Fig. 4.25 (b). These spectra are taken at an even higher excitation intensity of 12 – 15 mW. Accordingly, the profile of the ground state emission is lowered and broadened, and a number of peaks are observed at higher photon energies, which can be assigned roughly to higher electron and hole states. A strong signal is observed at a photon energy of 1.145 eV, labeled as L_I , and another one at 1.193 eV, being labeled as L_{II} . These peaks show a consistency in terms of their intensity behavior under varying excitation intensities, as can be observed in Fig. 4.25 (b). Thus, they might be assigned to the first and the second excited electron state, if an extraordinarily large energy difference between the states is accepted also for this quantum dot, as like for the data shown previously by Fig. 4.25 (a). More mysterious is the signal observed at an even higher photon energy of 1.217 eV, labeled as L_{ii} , which is already detected at a *lower* excitation intensity of 12 mW, before the appearance of the peaks L_I and L_{II} . A highly uncommon structure of the quantum-mechanical potential of the investigated quantum dots (Fig. 4.25 (a) and (b)) can be hypothesized, which may lead to an enhanced probability of uncommon recombination channels. However, there is no indication for the formation of such an exotic potential, regarding the

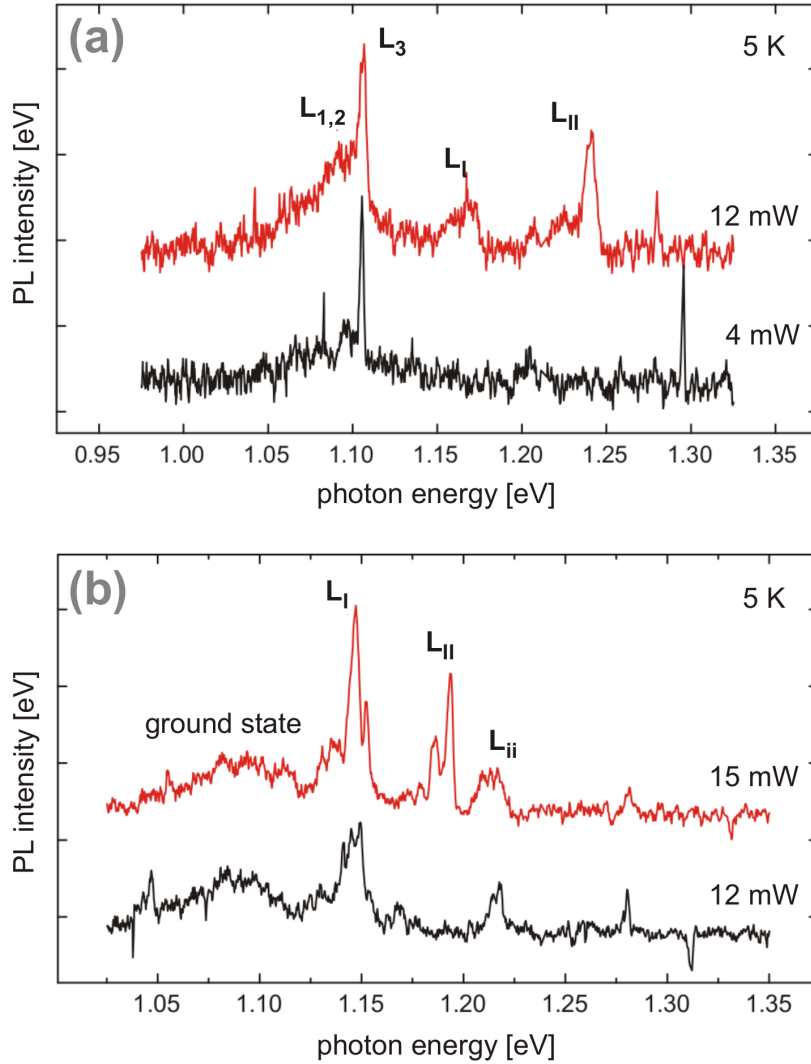


FIGURE 4.25: Photoluminescence of 2 single InAs/GaAs quantum dots, obtained at 5 K under varied excitation intensities.

majority of data from other quantum dots of this sample, and in particular the ordinary position of the ground state emission peaks of the quantum dots. Thus, the observed features remain mysterious for the time being.

Indeed, on basis of the data obtained within the frame of this work, merely a first insight to the system is possible. A more detailed investigation of the quantum dots, i.p. with the help of complementary techniques, should provide more information, which is required to work out a comprehensive understanding of InAs/GaAs quantum dots with low ground state energies. In general, the assignment given for the peaks which observed in the region of the ground state is fitting in the tendencies found for the references gathered from former investigations [26, 160, 164, 166, 167, 169]. However, the obtained values of the binding

energies, such as particularly the low binding energy of 3 – 4 meV of the neutral biexciton (XX), and the negative binding energy of the positively-charged trion (X^+), suggest that the behavior of these states is rather nonlinear in extrapolation towards low ground-state energies. In a firsthand-given scenario, a successive, general lowering of the values of all binding energies with a decreasing single-exciton recombination energy seems plausible, assuming a correspondingly successive lessening of the confinement effect owing to the increase of the quantum dot size. Evidently, further investigations are required on quantum dots with ground state energies that are varying on a broad range between 1.00 eV and 1.20 eV, in order to gain a more profound insight into the system.

Chapter 5

Conclusion

This work was intended to provide an accurate investigation of the photoluminescence of individual In(Ga)As/GaAs quantum dots with a ground-state energy of 1.0 – 1.1. eV. at low temperatures. This was inspired by a number of open questions concerning the interaction of confined carriers in semiconductor quantum dots which are of highest scientific interest in terms of a fundamental understanding of their formation and their opto-electronic properties, as well as for technological applications. The focus of the investigations was put on the determination of the binding energies of few-carrier complexes in the low-population regime, especially the biexciton state, in relation to the specific recombination energy of the single exciton within a quantum dot. For this purpose a novel scanning nearfield optical microscope (SNOM) had to be constructed, designed especially for operation at variable temperatures between 4 – 300 K. At low temperatures the thermal linewidth broadening of the photoluminescence of semiconductor quantum dots is reduced strongly, which in principle allows a spectral resolution of the order of a few μeV , depending on the spectrometer used. In this way, the optical line shift signature of few-carrier interactions within single quantum dots could be observed.

In this work a stable nearfield-scanning of the semiconductor quantum dot samples was demonstrated for the first time, using the new setup in a He-flow cryostate at a temperature of 5 K. The use of non-commercial fiber tip probes with a characteristic aperture of the order of 50 – 100 nm led to a spatial resolution of less than 200 nm, which allowed a specific selection of single quantum dots in different MOCVD-grown samples, containing on the one hand InGaAs/GaAs quantum dots with a spatial density of $10 \mu\text{m}^{-2}$ on average, and on the other hand InAs/GaAs quantum dots which are distributed in an inhomogeneous profile with varying spatial densities up to $100 \mu\text{m}^{-2}$. A first investigation of the photoluminescence of individual InGaAs/GaAs with a ground-state emission of 1.000 eV at 80 K, and of InAs/GaAs quantum dots with a ground-state emission of 1.100 eV at 5 K was performed under varying excitation intensities.

Based on the measurements, a systematic review of the related literature, and

corresponding theoretical calculations, the assignment of the emission signals to transitions from the single excitation, the biexciton, and further few-carrier states is discussed in detail. According to these considerations, for the biexciton in the investigated InGaAs/GaAs quantum dots a positive binding energy was found varying between 2 – 7 meV, and a negative binding energy of –11 meV for a positive trion, which is supposed to form because of the strong background doping of the sample. Further luminescence signals observed in the region of the ground-state are assigned to the appearance of a positively-charged biexciton with a positive binding energy of about 11 meV, and to the effect of higher carrier complexes forming with the successive population of the quantum dot at increasing excitation intensities. Out of these signals, one peak in particular can be assigned to the recombination of a ground-state electron with an excited hole state. With this assignment, the energy difference between the electron ground state and the first excited electron state is calculated to be approximately 50 meV. The obtained values for the InGaAs/GaAs system in general deviate in some aspects from earlier theoretical predictions which base on the assumed quantum dot structure. The interpretation partly leads to the suggestion that actually the confinement of the carriers within the quantum dots is stronger than expected. This can be explained by the specific stoichiometry distribution found in InGaAs/GaAs quantum dots, showing the profile of an inverted truncated cone. Indeed, a detailed analysis of the data in view of a thorough understanding of the system is difficult, owing to the lack of a definite signature in the obtained spectra and the currently low quantity of data which impedes a statistical approach to the relevant questions.

For the investigated InAs/GaAs quantum dots a positive binding energy of 3 – 4 meV was found for the biexciton state. The formation of a positive trion can also be assumed for some of the investigated InAs/GaAs quantum dots, depending on the attractivity of the particular quantum dot for single carriers, as well as the corresponding appearance of a positively-charged biexciton. According to the obtained data, a negative binding energy of the positive trion of about –3 meV is found, and a positive binding energy of the charged biexciton of 1 meV. The existence of a first excited electron state is supposed at least for a part of the quantum dots in the investigated sample, according to the related ensemble measurements performed using micro-photoluminescence. Further, recombinations of ground-state electrons with excited hole states were observed in some cases, which justifies the assumption of an excited electron state as well. The obtained results suggest an essentially nonlinear progression of the binding energies of the few-carrier states with decreasing ground state energies.

An interesting feature of the sample was the observation of a relatively large energy difference between the hole states of more than 10 meV, which corresponds to a particularly large homogeneous line broadening of 50 meV observed at room temperature. A number of further peaks were observed in the spectra on InAs/GaAs quantum dots at higher excitation intensities, which cannot be

assigned clearly to certain transitions yet. This is partly due to the generally limited quantity of data, but is also a consequence of the specific character of the sample, which had been grown without wafer rotation, thus leading to a broad variety of different forms of quantum dots. Nevertheless, in general the obtained results are consistent with the systematics that is proposed for this quantum dot system [26], even though a definite understanding of InAs/GaAs quantum dots with a ground-state emission of 1.100 eV remains outstanding at this stage.

Bibliography

- [1] A.I. Ekimov and A.A. Onushzhenko, *SJETP Lett.* **34**, 2225 (1981).
- [2] L. Goldstein, F. Glas, J.Y. Marzin, M.N. Charasse, and G. Le Roux, *Appl. Phys. Lett.* **47**, 1099 (1985).
- [3] M. Faraday, *Philos. Trans.* **147**, 145 (1857).
- [4] P.W. Anderson, *Phys. Rev.* **109**, 1492 (1958).
- [5] D.S. Wiersma, *Nature* **390**, 671 (1997).
- [6] J.W.S. Rayleigh, *Phil. Mag.* **26**, 256 (1888).
- [7] V.P. Bykov, *Sov. J. Quantum Electron.* **4**, 861 (1975).
- [8] S. Iijima, *Nature* **354**, 56 (1991).
- [9] R. Saito, M. Fujita, G. Dresselhaus, and M.S. Dresselhaus, *Phys. Rev. B* **46**, 1804 (1992).
- [10] J.H.K. Ky Hirschberg, L. Brunsveld, A. Ramzi, J.A.J.M. Vekemans, R.P. Sijbesma, and E.W. Meijer, *Nature* **407**, 167 (2000).
- [11] G. McDermott, S.M. Prince, A.A. Freer, A.M. Hawthornhwaite-Lawless, M.Z. Papiz, R.J. Cogdell, and N.W. Isaacs, *Nature* **374**, 517 (1995).
- [12] P. Vukusic and J.R. Sambles, *Nature* **424**, 852 (2003).
- [13] P. Michler, *Single Quantum Dots*, Springer Berlin, Berlin, 2003.
- [14] M. Grundmann, *The Physics of Semiconductors*, Springer Berlin, Berlin, 2006.
- [15] U. Woggon, *Optical Properties of Semiconductor Quantum Dots*, Springer, Berlin, 1997.
- [16] M. Grundmann, *Nano-Optoelectronics*, Springer Berlin, Berlin, 2002.

- [17] Ch. Weissmantel and C. Hamann, *Grundlagen der Festkörperphysik*, Springer Berlin, Berlin, 1979.
- [18] V.A. Shchukin, N.N. Ledentsov, and D. Bimberg, *Epitaxy of Nanostructures*, Springer Berlin, Berlin, 2003.
- [19] N.N. Ledentsov, *Growth Processes and Surface Phase Equilibria in Molecular Beam Epitaxy*, Springer Berlin, Berlin, 1999.
- [20] Frank Heinrichsdorff, *MOCVD Growth and Laser Applications of In(Ga)As/GaAs Quantum Dots*, PhD thesis, Technische Universität Berlin, 1998.
- [21] M. Grundmann, *Physica E* **5**, 167 (2000).
- [22] N.N. Ledentsov, V.M. Ustinov, V.A. Shchukin, P.S. Kop'ev, Zh.I. Alferov, and D. Bimberg, *Semiconductors* **32**, 343 (1998).
- [23] M. Geller et. al., *Appl. Phys. Lett.* **92**, 092108 (2008).
- [24] P. Michler, A. Kiraz, C. Becher, W.V. Schoenfeld, P.M. Petroff, L. Zhang, E. Hu, and A. Imamoğlu, *Science* **290**, 2282 (2000).
- [25] R.M. Stevenson, R.J. Young, P. Atkinson, K. Cooper, D.A. Ritchie, and A.J. Shields, *Nature* **439**, 179 (2006).
- [26] Sven Rodt, *Exzitonische Komplexe in einzelnen III-V Quantenpunkten*, PhD thesis, Humboldt-Universität Berlin, 2006.
- [27] D.W. Pohl, W. Denk, and M. Lanz, *Appl. Phys. Lett.* **44**, 651 (1984).
- [28] J.L. Spithoven, J. Lorbacher, I. Manke, F. Heinrichsdorff, and M. Dhne, *J. Vac. Sci. Technol. B* **17**, 1632 (1999).
- [29] I. Manke, J. Lorbacher, J.L. Spithoven, F. Heinrichsdorff, and M. Dhne, *Surf. Interface Anal.* **27**, 491 (1999).
- [30] E. Abbe, *Gesammelte Abhandlungen*, Fischer, Jena, 1904.
- [31] Andrea Crottini, *Low-temperature near-field spectroscopy of quantum wires*, PhD thesis, Ecole Polytechnique Federale de Lausanne, 2001.
- [32] F. de Fornel, *Evanescent Waves: From Newtonian Optics to Atomic Optics*, Springer, Berlin, 2001.
- [33] E.H. Synge, *The Philosophical Magazine* **7**, 356 (1928).
- [34] A. Lewis, M. Isaacson, A. Harootunian, and A. Muray, *Ultramicroscopy* **13**, 227 (1984).

- [35] G. Binnig, H. Rohrer, Ch. Gerber, and E. Weibel, *Phys. Rev. Lett.* **49**, 57 (1982).
- [36] G. Binnig, C.F. Quate, and Ch. Gerber, *Phys. Rev. Lett.* **56**, 930 (1986).
- [37] L. Novotny and B. Hecht, *Principles of Nano-Optics*, Cambridge University Press, Cambridge, 2006.
- [38] Dr. Christoph Lienau, *Optische Nahfeldspektroskopie von Halbleiter-Nanostrukturen, Habilitationsschrift zur Erlangung der Lehrbefähigung für das Fach Physik*, Humboldt-Universität zu Berlin, Berlin, 2002.
- [39] M.A. Paesler and P.J. Moyer, *Near-field Optics: Theory, Instrumentations and Applications*, J. Wiley and Sons, Inc., New York, 1996.
- [40] T. Saiki, S. Mononobe, M. Ohtsu, N. Saito, and J. Kusamo, *Appl. Phys. Lett.* **68**, 2612 (1996).
- [41] H. de Senarmont, E. Verdet, and L. Fresnel, *Oeuvre completes d'Augustin Fresnel*, Imprimerie imperiale, Paris, MDCCCLXVI.
- [42] T. Young, *On the theory of light and colours*, Philosophical Transactions, 1802.
- [43] M. Born, *Optik*, Springer, Berlin, 1972.
- [44] Francesca Intonti, *Near-field optical spectroscopy of disorder in semiconductor nanostructures*, PhD thesis, Humboldt-Universität Berlin, 2001.
- [45] Ingo Stamatis Manke, *Rasternahfeldmikroskopie an einzelnen $In_{0,4}Ga_{0,6}As/GaAs$ -Quantenpunkten*, PhD thesis, Technische Universität Berlin, 2002.
- [46] E. Betzig, J.K. Trautman, T.D. Harris, J.S. Weiner, and R.L.Kostelak, *Science* **251**, 1468 (1991).
- [47] P. Hoffmann, B. Dutoit, and R.-P. Salath, *Ultramicroscopy* **61**, 165 (1995).
- [48] D.M. Eisele, L.J. Rosanski, J. Knoester, S. Kirstein, J.P. Rabe, and D. Vanden Bout, *J. Chem. Phys.*, submitted .
- [49] Ch. Gerthsen, H.O. Kneser, and H. Vogel, *Physik*, Springer, Berlin, 1986.
- [50] R.C. Reddick, R.J. Warmack, and T.L. Ferrell, *Phys. Rev. B* **39**, 767 (1989).
- [51] E.R. Mendez, J.J. Greffet, and R. Carminati, *Opt. Com.* **142**, 7 (1997).

- [52] W.I. Smirnow, *Lehrgang der Höheren Mathematik, Teil IV*, VEB Deutscher Verlag der Wissenschaften, Berlin, 1968.
- [53] M. Geller, I. Manke, K. Hodeck, R. Heitz, and M. Dähne, *Phys. Rev. B* **64**, 233312 (2001).
- [54] C.C. Williams and H.K. Wickramasinghe, *Opt. Lett.* **14**, 542 (1989).
- [55] H.K. Wickramasinghe, *Apertureless near field optical microscope*, US Patent 4947034, 1990.
- [56] R. Bachelot, P. Gleyzes, and A.C. Boccara, *Opt. Lett.* **20**, 1924 (1995).
- [57] A. Bouhelier, M. Beversluis, A. Hartschuh, and L. Novotny, *Phys. Rev. Lett.* **90**, 013903 (2003).
- [58] J. Jersch, F. Demming, L.J. Hildenhagen, and K. Dickmann, *Appl. Phys. A* **66**, 29 (1998).
- [59] E.J. Sanchez, L. Novotny, and X. Sunney Xie, *Phys. Rev. Lett.* **82**, 4014 (1999).
- [60] T. Kalkbrenner, M. Ramstein, J. Mlynek, and V. Sandoghdar, *J. Micr.* **202**, 72 (2000).
- [61] W. Bente, *Plasmonen in einzelnen oxidgetragenen Edelmetallpartikeln*, PhD thesis, Technische Universität Berlin, 2006.
- [62] M. Tsukada, T. Schimizu, and K. Kobayashi, *Ultramicroscopy* **42**, 360 (1992).
- [63] H. Raether, *Surface plasmons on smooth and rough surfaces and on grating*, Springer Tracts in Modern Physics, Springer Berlin, 1988.
- [64] M. Moskovits, *Rev. Mod. Phys.* **57**, 783 (1985).
- [65] C.E. Bohren and D.R. Huffman, *Absorption and Scattering of Light by Small Particles*, John Wiley & Sons, Chichester, 1983.
- [66] U. Kreibig and M. Vollmer, *Absorption and scattering of light by small particles*, Springer Series Materials Science, vol 25, Springer Berlin, 1995.
- [67] Andrea Isabel Matschulat, *Mikroskopische Visualisierung von Gold-Nanopartikeln fr die Medizin*, Technische Universität Berlin, diploma thesis, 2007.
- [68] P. Johansson, R. Monreal, and P. Apell, *Phys. Rev. B* **42**, 9210 (1990).

- [69] P. Johansson and R. Monreal, *Z. Phys. B* **42**, 9210 (1990).
- [70] E. Betzig, P.L. Finn, and J.S. Weiner, *Appl. Phys. Lett.* **60**, 2484 (1992).
- [71] K. Karrai and R.D. Grober, *Proc. SPIE* **69**, 2535 (1995).
- [72] K. Karrai, *Lecture notes on shear and friction force detection with quartz tuning forks*, Ludwig-Maximilians Universität München, Center for NanoScience, München, 2000.
- [73] K. Karrai and R.D. Grober, *Appl. Phys. Lett.* **66**, 1842 (1995).
- [74] P. Guenther, U.Ch. Fischer, and K. Dransfeld, *Appl. Phys. B* **48**, 89 (1989).
- [75] F.F. Froehlich and T.D. Milster, *Appl. Phys. Lett.* **70**, 1500 (1997).
- [76] A.G.T. Ruiter, J.A. Veerman, K.O. van der Werf, and N.F. van Hulst, *Appl. Phys. Lett.* **71**, 28 (1997).
- [77] W.A. Aita and C.C. Davis, *Appl. Phys. Lett.* **70**, 405 (1997).
- [78] C.L. Jahnke, S.H. Huerth, Beverly Clark III, and H.D. Hallen, *Appl. Phys. Lett.* **81**, 21 (2002).
- [79] M.J. Gregor, P.G. Blome, J. Schöfer, and R.G. Ulbrich, *Appl. Phys. Lett.* **68**, 307 (1995).
- [80] T. Okajima and S. Hirotsu, *Appl. Phys. Lett.* **71**, 545 (1996).
- [81] S. Davy, M. Spajer, and D. Courjon, *Appl. Phys. Lett.* **73**, 2594 (1998).
- [82] R. Brunner, O. Marti, and O. Hollrichter, *J. Appl. Phys.* **86**.
- [83] D.A. Lapshin, V.S. Letokhov, G.T. Shubeita, S.K. Sekatskii, and G. Dietler, *Proceedings of the IEEE* **88**, 1460 (2000).
- [84] D.A. Lapshin and V.S. Letokhov, *Appl. Phys. Lett.* **81**, 1503 (2002).
- [85] D.A. Lapshin, V.S. Letokhov, G.T. Shubeita, S.K. Sekatskii, and G. Dietler, *Ultramicroscopy* **99**, 227 (2004).
- [86] S. Hoppe, G. Ctistis, J.J. Paggel, and P. Fumagalli, *Ultramicroscopy* **102**, 221 (2005).
- [87] M. Ternes, C.P. Lutz, C.F. Hirjibehedin, F.J. Giessibl, and A.J. Heinrich, *Science* **319**, 1066 (2008).
- [88] T.R. Albrecht, P. Grütter, D. Horne, and D. Rugar, *J. Appl. Phys.* **69**, 668 (1991).

- [89] K. Karrai and R.D. Grober, *Ultramicroscopy* **61**, 197 (1995).
- [90] Ch. Lienau, private communication.
- [91] K. Karrai, private communication.
- [92] H. Eisele, private communication.
- [93] A. Walid and C.C. Davis, *Appl. Phys. Lett.* **70**, 405 (1997).
- [94] R. Garcia, R. Magerle, and R. Perez, *Nature Materials* **6**, 405 (2007).
- [95] A. Knorr, private communication.
- [96] A. Zorn, private communication.
- [97] T. Mezger, *Das Rheologie-Handbuch für Anwender von Rotations- und Oszillations-Rheometern*, Vincentz Network, 2000.
- [98] C.J. Chen, *Introduction to Scanning Tunneling Microscopy*, Oxford University Press, New York, 1993.
- [99] M. Dähne, private communication.
- [100] S. Rodt, private communication.
- [101] Tobias Günther, *Femtosekunden Nahfeldspektroskopie an einzelnen Halbleiterquantenpunkten*, PhD thesis, Humboldt-Universität Berlin, 2002.
- [102] G. Guttroff, J.M. Keto, C.K. Shih, A. Anselm, and B.G. Streetman, *Appl. Phys. Lett.* **68**, 3620 (1996).
- [103] T. Saiki, K. Nishi, and M. Ohtsu, *Jap. J. Appl. Phys.* **37**, 1638 (1998).
- [104] D.W. Pohl, *Rev. Sci. Instr.* **58**, 54 (1987).
- [105] G. Mariotto, M. D'Angelo, and I.V. Shvets, *Rev. Sci. Instr.* **70**, 3651 (1999).
- [106] S.H. Pan, *Piezo-electric Motor*, International Patent WO 93/19494, 1990.
- [107] Kai Friedrich Hodeck, *Rasternahfeldspektroskopie an einzelnen $In_{0,4}Ga_{0,6}As/GaAs$ -Quantenpunkten bei tiefen Temperaturen*, Technische Universität Berlin, diploma thesis, Berlin, 2001.
- [108] Christian Griesche, *Rasternahfeld-Lumineszenzspektroskopie an Quantenpunkten mit lokaler Dichtefluktuation*, Technische Universität Berlin, diploma thesis, Berlin, 2005.
- [109] attocube systems AG, Königinstrasse 11a RGB, 80539 München, Germany, www.attocube.com.

- [110] Omar Al-Khatib, *Lumineszenzuntersuchungen an einzelnen Quantenpunkten bei unterschiedlichen Temperaturen*, Technische Universität Berlin, diploma thesis, Berlin, 2006.
- [111] L.N. Lupinovich and L.P. Zosin, *Mechanics of Composite Materials* **22**, 530 (1987).
- [112] D.R. Turner, *Etch procedure for optical fibers*, US Patent 4469554, 1983.
- [113] B. Ren, G. Picardi, and B. Pettinger, *Rev. Sci. Instr.* **75**, 837 (2004).
- [114] Maximilian Assig, *Aufbau und Inbetriebnahme eines aperturlosen optischen Rasternahfeldmikroskops*, Technische Universität Berlin, diploma thesis, Berlin, 2006.
- [115] J.P. Ibe, Jr. P.P. Bey, S.L. Brandow, R.A. Brizzolara, N.A. Burnham, D.P. DiLella, K.P. Lee, C.R.K. Marrian, and R.J. Colton, *J. Vac. Sci. Technol. A* **8**, 3570 (1990).
- [116] A. Naber, *J. Micr.* **194**, 307 (1998).
- [117] B. Lamprecht, G. Schider, R.T. Lechner, H. Ditlbacher, J.R. Krenn, A. Leitner, and F.R. Aussenegg, *Phys. Rev. Lett.* **84**, 4721 (2000).
- [118] Helmholtz-Zentrum Berlin für Materialien und Energie, Glienicker Strasse 100, 14109 Berlin, Germany, <http://www.hmi.de>.
- [119] K. Hodeck, I. Manke, M. Geller, R. Heitz, F. Heinrichsdorff, A. Krost, D. Bimberg, H. Eisele, and M. Dähne, *phys. stat. sol. (c)* **0**, 1209 (2003).
- [120] S. Schmitt-Rink, D.A.B. Miller, and D.S. Chemla, *Phys. Rev. B* **35**, 8113 (1987).
- [121] D. Bimberg, M. Grundmann, and N.N. Ledentsov, *Quantum Dot Heterostructures*, John Wiley and Sons, Chichester, 1999.
- [122] O. Stier, M. Grundmann, and D. Bimberg, *Phys. Rev. B* **59**, 5688 (1999).
- [123] L.-W. Wang, J. Kim, and A. Zunger, *Phys. Rev. B* **59**, 5678 (1999).
- [124] D. Leonard, M. Krishnamurty, C.M. Reaves, S.P. Denbaars, and P.M. Petroff, *Appl. Phys. Lett.* **63**, 3203 (1993).
- [125] Holger Eisele, *Cross-Sectional Scanning Tunneling Microscopy of InAs/GaAs Quantum Dots*, PhD thesis, Technische Universität Berlin, 2002.
- [126] F.C. Frank and J.H. van der Merwe, *Proc. Roy. Soc.* **A189**, 205 (1949).

- [127] M. Volmer and A. Weber, *Z. Phys. Chem.* **119**, 277 (1926).
- [128] I.N. Stranski and L. Krastanov, *SB Wiener Akad. Wiss., Klasse IIb* **146**, 797 (1938).
- [129] H. Lüth, *Surfaces and Interfaces of Solid Materials*, Springer, Berlin, 1997.
- [130] Roman Sellin, *Metalorganic Chemical Vapor Deposition of High-Performance GaAs-Based Quantum-Dot Lasers*, PhD thesis, Technische Universität Berlin, 2003.
- [131] J.M. Moison, F. Houzay, F. Barthe, L. Leprince, E. Andr, and O. Vatel, *Appl. Phys. Lett.* **64**, 196 (1994).
- [132] D. Leonard, K. Pond, and P.M. Petroff, *Phys. Rev. B* **50**, 11687 (1994).
- [133] Q. Xie, P. Chen, and A. Madhukar, *Appl. Phys. Lett.* **65**, 2051 (1994).
- [134] N. Moll, M. Scheffler, and E. Pehlke, *Phys. Rev. B* **58**, 4566 (1998).
- [135] A. Lenz, private communication.
- [136] F. Guffarth, R. Heitz, A. Schliwa, K. Pötschke, and D. Bimberg, *Physica E* **21**, 326 (2004).
- [137] R. Heitz, F. Guffarth, K. Pötschke, A. Schliwa, D. Bimberg, N.D. Zakharov, and P. Werner, *Phys. Rev. B* **71**, 045325 (2005).
- [138] R. Seguin, A. Schliwa, S. Rodt, K. Pötschke, U.W. Pohl, and D. Bimberg, *Phys. Rev. Lett.* **95**, 257402 (2005).
- [139] U.W. Pohl, K. Pötschke, A. Schliwa, F. Guffarth, D. Bimberg, N.D. Zakharov, P. Werner, M.B. Lifshits, and V.A. Shchukin, *Phys. Rev. B* **72**, 245332 (2005).
- [140] Andrea Lenz, *Atomic structure of capped In(Ga)As and GaAs quantum dots for optoelectronic devices*, PhD thesis, Technische Universität Berlin, 2008.
- [141] G. Constantini, A. Rastelli, C. Manzano, P. Acosta-Diaz, R. Songmuang, G. Katsaros, O.G. Schmidt, and K. Kern, *Phys. Rev. Lett.* **96**, 226106 (2006).
- [142] P. Kratzer, Q.K.K. Liu, P. Acosta-Diaz, C. Manzano, G. Constantini, R. Songmuang, A. Rastelli, O.G. Schmidt, and K. Kern, *Phys. Rev. B* **73**, 205347 (2006).

- [143] J.M. Garcia, T. Mankad, P.O. Holtz, P.J. Wellman, and P.M. Petroff, Appl. Phys. Lett. **72**, 3172 (1998).
- [144] K. Pötschke, private communication.
- [145] A. Schliwa, M. Winkelkemper, and D. Bimberg, Phys. Rev. B **76**, 205324 (2007).
- [146] H. Eisele and K. Jacobi, Appl. Phys. Lett. **90**, 129902 (2007).
- [147] J. Marquez, L. Geelhaar, and K. Jacobi, Appl. Phys. Lett. **78**, 2309 (2001).
- [148] A. Lenz, H. Eisele, R. Timm, L. Ivanova, H.-Y. Liu, M. Hopkinson, U.W. Pohl, and M. Dähne, Physica E **40**, 1988 (2008).
- [149] H. Eisele, R. Timm, A. Lenz, Ch. Hennig, M. Ternes, S.K. Becker, and M. Dähne, phys. stat. sol. (c) **4**, 1129 (2003).
- [150] H. Eisele, A. Lenz, Ch. Hennig, R. Timm, M. Ternes, and M. Dähne, J. Crystal Growth **248**, 322 (2003).
- [151] Andrei Schliwa, private communication.
- [152] P.W. Fry, I.E. Itskevitch, D.J. Mowbray, M.S. Skolnick, J.J. Finley, J.A. Barker, E.P. O'Reilly, L.R. Wilson, I.A. Larkin, P.A. Maksym, M. Hopkinson, M. Al-Khafaji, J.P.R. David, A.G. Cullis, G. Hill, and J.C. Clark, Phys. Rev. Lett. **84**, 733 (2000).
- [153] N. Liu, J. Tersoff, O. Baklenov, A.L. Holmes, and C.-K. Shih, Phys. Rev. Lett. **84**, 334 (2000).
- [154] A. Lenz, R. Timm, H. Eisele, Ch. Hennig, S.K. Becker, R.L. Sellin, U.W. Pohl, D. Bimberg, and M. Dähne, Appl. Phys. Lett. **81**, 5150 (2002).
- [155] R. Heitz, O. Stier, I. Mukhametzhanov, A. Madhukar, and D. Bimberg, Phys. Rev. B **62**, 11017 (2000).
- [156] Oliver Stier, *Electronic and Optical Properties of Quantum Dots and Wires*, PhD thesis, Technische Universität Berlin, 2000.
- [157] K. Shiraishi and E. Yamaguchi, Phys. Rev. B **42**, 3064 (1990).
- [158] G.H. Li, A.R. Goñi, C. Abraham, K. Syassen, P.V. Santos, A. Cantarero, O. Brandt, and K. Ploog, Phys. Rev. B **50**, 1575 (1994).
- [159] L.-W. Wang and A. Zunger., *Pseudopotential Theory of Nanometer Silicon Quantum Dots* in : *Nanocrystalline Semiconductor Materials*, Elsevier Science, 1996.

- [160] S. Rodt, A. Schliwa, K. Pötschke, F. Guffarth, and D. Bimberg, Phys. Rev. B **71**, 155325 (2005).
- [161] R. Heitz, private communication.
- [162] O. Stier, A. Schliwa, R. Heitz, M. Bichler, and G. Abstreiter, Phys. Rev. B **64**, 195326 (2001).
- [163] M. Grundmann, N.N. Ledentsov, O. Stier, D. Bimberg, V.M. Ustinov, P.S. Kop'ev, and Zh.I. Alferov, Appl. Phys. Lett. **68**, 979 (1996).
- [164] E. Moreau, I. Robert, L. Manin, V. Thierry-Mieg, J.M. Gérard, and I. Abram, Phys. Rev. Lett. **87**, 183601 (2001).
- [165] S. Rodt, R. Heitz, A. Schliwa, R.L. Sellin, F. Guffarth, and D. Bimberg, Phys. Rev. B **68**, 035331 (2003).
- [166] M. Bayer, F. Findeis, A. Zrenner, M. Bichler, and G. Abstreiter, Phys. Rev. B **64**, 195326 (2001).
- [167] J.J. Finley, P.W. Fry, A.D. Ashmore, A. Lemaitre, A.I. Tartakovskii, R. Oulton, D.J. Mowbray, M.S. Skolnick, M. Hopkinson, P.D. Buckle, and P.A. Maksym, Phys. Rev. B **63**, 161305 (2001).
- [168] M. Bayer, O. Stern, P. Hawrylak, S. Fafard, and A. Forchel, Nature **405**, 923 (2000).
- [169] L. Landin, M.-E. Pistol, C. Pryor, M. Persson, L. Samuelson, and M. Miller, Phys. Rev. B **60**, 16640 (1999).
- [170] D.V. Regelman, E. Dekel, D. Gershoni, E. Ehrenfreund, A.J. Williamson, J. Shumway, A. Zunger, W.V. Schoenfeld, and P.M. Petroff, Phys. Rev. B **64**, 165301 (2001).
- [171] A.I. Tartakovskii, M.N. Makhonin, J. Cahill, D.M. Whittaker, J-P.R. Wells, A.M. Fox, D.J. Mowbray, M.S. Skolnick, M.J. Steer, K.M. Groom, and M. Hopkinson, Appl. Phys. Lett. **85**, 2226 (2004).
- [172] M. Böhm and A. Scharmann, *Höhere Experimentalphysik*, VCH, Weinheim, 1992.
- [173] B. Di Bartolo, *Optical Interactions in Solids*, Ed. 1, John Wiley and Sons, 1968.
- [174] P. Borri, W. Langbein, J.M. Hvam, and F. Martelli, Phys. Rev. B **60**, 4505 (1999).

- [175] D.F. Schroeter, D.J. Griffiths, and P.C. Sercel, Phys. Rev. B **54**, 1486 (1996).
- [176] R. Heitz, I. Mukhametzhanov, A. Madhukar, A. Hoffmann, and D. Bimberg, J. Elec. Mat. **28**, 520 (1999).
- [177] D. Bimberg, M. Sondergeld, and E. Grobe, Phys. Rev. B **4**, 3451 (1971).
- [178] R. Pssler, phys. stat. sol. (b) **200**, 155 (1997).
- [179] R. Pssler, J. Appl. Phys. **83**, 3356 (1998).
- [180] D.A.B. Miller, D.S. Chemla, T.C. Damen, A.C. Gossard, W. Wiegmann, T.H. Wood, and C.A. Burrus, Phys. Rev. Lett. **53**, 2173 (1984).
- [181] S.A. Empedocles, D.J. Norris, and M.G. Bawendi, Phys. Rev. Lett. **77**, 3873 (1996).
- [182] R.J. Warburton, C. Schulhauser, D. Haft, C. Schflein, K. Karrai, J.M. Garcia, W. Schoenfeld, and P.M. Petroff, Phys. Rev. B **65**, 113303 (2002).
- [183] J.J. Finley, M. Sabathil, P. Vogl, G. Abstreiter, R. Oulton, A.I. Tartakovskii, D.J. Mowbray, M.S. Skolnick, S.L. Liew, A.G. Cullis, and M. Hopkinson, Phys. Rev. B **70**, 201308 (2004).
- [184] M. Grundmann, O. Stier, and D. Bimberg, Phys. Rev. B **52**, 11969 (1995).
- [185] K. Matsuda, K. Ikeda, T. Saiki, H. Tsuchiya, H. Saito, and K. Nishi, Phys. Rev. B **63**, 121304 (2000).
- [186] M. Grundmann and D. Bimberg, Phys. Rev. B **55**, 9740 (1997).
- [187] F. Heinrichsdorff, private communication.
- [188] A. Rosenauer, W. Oberst, D. Livinov, D. Gerthsen, A. Frster, and R. Schmidt, Phys. Rev. B **61**, 8276 (2000).
- [189] Johannes Leonardus Spithoven, *Scanning near-field optical microscopy and spectroscopy of quantum dots*, Technische Universität Berlin, diploma thesis, Berlin, 1998.
- [190] J.M. Garcia, G. Medeiros-Ribeiro, K. Schmidt, T. Ngo, J.L. Feng, A. Lorke, J.Kotthaus, and P.M. Petroff, Appl. Phys. Lett. **71**, 2014 (1997).